

Analytical Design Procedures for the Odd Mode of Ridge Gap Waveguide Devices and Antennas

Abduladeem Altayib Amer Beltayib

A Thesis

In the Department

of

Electrical and Computer Engineering

Presented in Partial Fulfillment of the Requirements

For the Degree of

Doctor of Philosophy (Electrical and Computer Engineering) at

Concordia University

Montréal, Québec, Canada

March, 2020

© Abduladeem Altayib Amer Beltayib, 2020

CONCORDIA UNIVERSITY

School of Graduate Studies

This is to certify that the thesis prepared

By: Abduladeem Altayib Amer Beltayib

Entitled: Analytical Design Procedures for the Odd Mode of Ridge Gap Waveguide
Devices and Antennas

and submitted in partial fulfillment of the requirements for the degree of

Doctor of Philosophy (Electrical and Computer Engineering)
complies with the regulations of the University and meets the accepted standards with
respect to originality and quality.

Signed by the final examining committee:

Dr. Ming Yuan Chen Chair

Dr. Serioja Ovidiu Tatu External Examiner

Dr. Abdessamad Ben Hamza External to Program

Dr. Ahmed A. Kishk Examiner

Dr. Robert Paknys Examiner

Dr. Abdel R. Sebak Thesis Supervisor

Approved by:

Dr. Rastko Selmic, Graduate Program Director

February 10, 2020

Dr. Amir Asif, Dean
Gina Cody School of Engineering & Computer Science

Abstract

Analytical Design Procedures for the Odd Mode of Ridge Gap Waveguide Devices and Antennas

Abduladeem Altayib Amer Beltayib, Ph.D.

Concordia University, 2020

The millimeter-wave (mm-wave) band has attracted attention due to its wideband characteristics that make it able to support multi-gigabit per second data rate. Nevertheless, the performance of mm-wave wireless communication systems is restricted due to attenuation loss. Design of mm-wave components and antennas is rapidly growing with the current evolution in the wireless communication systems. However, the traditional waveguide structures such as microstrip, coplanar, substrate integrated waveguide, and rectangular waveguide either suffer from high losses or difficulty in manufacturing at mm-wave band. The ridge gap waveguide (RGW) technology is considered as a promising waveguide technology for the mm-wave band. RGW technology overcomes the conventional guiding structure problems as the wave propagates in an air gap region which eliminates the dielectric loss. Moreover, RGW does not need any electrical contacts, unlike traditional rectangular waveguides. Also, the RGW can be implemented in the printed form (PRGW) for easy integration with other planer system components.

In this thesis, the use of the odd mode (TE_{10}^{RGW}) RGW to design mm-wave components and antennas is presented. First, a systematic design methodology for the RGW using hybrid PEC/PMC waveguide approximation is presented. This reduces the design time using full wave simulators. The concept has been verified by simulation and experimental measurements. Second, two different methods to excite the odd mode in RGW are studied and investigated. In the first method, a planar L-shape RGW is used where less than -10 dB reflection coefficient is achieved, from 28 to 36 GHz, and more than 93% of the input power has been converted into the odd mode at the output port. The second

method uses a magic tee with a shorted sum port and provides a wideband pure odd mode at the output port with reflection coefficient less than -10 dB from 28 GHz to 39 GHz. Other mm-wave components based on odd mode TE_{10}^{RGW} RGW are designed and presented including a Y-junction power divider and 3 dB forward coupler are designed for the first time in RGW technology. The Y-junction has a wideband matching from 28 to 34 GHz with a reflection coefficient less than -15 dB and the transmission output levels are about -3.3 dB.

The usefulness of the odd mode RGW lies in the ability to increase the channel bandwidth that has been achieved by designing a dual-mode RGW. A magic tee is used to simultaneously excite the fundamental mode Q-TEM and the odd mode TE_{10}^{RGW} on the ridgeline. The proposed dual-mode RGW performance is verified through simulation and measurement of a back-to-back configuration. The proposed design achieves a matching level less than -10 dB for the two modes over the frequency range from 29 GHz to 34.5 GHz with isolation better than 23 dB. The dual-mode RGW is then used to feed a reconfigurable Vivaldi horn antenna where two different radiation patterns can be obtained depending on the excited mode. The Q-TEM generates a single beam pattern, while the odd mode TE_{10}^{RGW} generates a dual-beam pattern. The maximum gain for the single beam radiation is 12.1 dBi, while it is 10.43 dBi for the dual-beam pattern. The bandwidth of the dual-mode antenna is 25% at 32 GHz with impedance matching less than -10 dB and isolation better than 20 dB.

Finally, several antennas are presented in this thesis based on the odd mode RGW. A novel differential feeding cavity antenna using the odd mode of RGW is presented. The measured results show good performance in terms of gain, bandwidth, sidelobe level, and cross-polarization. The maximum gain is 16.5 dBi, and the sidelobe level is -17 dB and -13.8 dB, for the E-plane and H-plane, respectively. Moreover, the proposed antenna has low cross-polarization levels of -35 dB in the E-plane and -27 dB in the H-plane. In addition, two 2x1 linear frequency scanning array antennas are designed and implemented using the proposed Y-junction to generate single beam and dual-beam patterns. The beam scan is from -11° to 40° at 28 GHz and 32 GHz, respectively.

Acknowledgments

First of all, I sincerely wish to thank my supervisor Prof. Abdel Razik Sebak, who gave me the opportunity to join his group, and support me. It was a real pleasure for me to have such an exceptional scholar and it was my honor to be his PhD student. Furthermore, I would like to thank my committee members, Prof.Paknys, Prof.Kishk,Dr. S Tatu,and Prof.Ben Hamza for their review of my dissertation and their constructive commentsand feedback.

My thanks extend to my colleagues in my office, who provided me with some useful discussions. Also, I would like to thank Moufthah Asadi, Magid Alzidani, Zouhair Briquish, Walid Dyab, and Ahmad Sakar.

In particular, I would like to acknowledge my colleague Islam Afifi who collaborated with me and helped me during measurements.

I finally would like to thank my beloved parents, brother, sisters, and wife for their love and warm support.

Contents

List of Figures **x**

List of Abbreviations **xvii**

1 Introduction and Historical Overview **1**

 1.1 Introduction 1

 1.2 Millimeter Wave Overview 3

 1.3 Motivations and Problem Statement 4

 1.4 Objectives 6

 1.5 Contributions 7

 1.6 Thesis Organization 8

2 Background and Literature Review **9**

 2.1 Historical Overview of Guiding Structures 9

 2.1.1 Microstrip and Striplines, Coplanar and Grounded Coplanar Waveguides, Metal and Substrate-integrated Waveguides 10

 2.1.2 Gap Waveguide Technology 15

 2.2 Ridge Gap Waveguide (RGW) Concept 16

 2.2.1 Ridge Gap Waveguide Structure 18

 2.2.2 Bed of Nails Operation 19

 2.2.3 Bed of Nails Region Downed by a PEC Ground Plane 20

 2.2.4 Bed of Nails Covered From Both Sides by PEC-Plates 21

 2.3 Analytical Design Procedure for Forward Wave Couplers in RGW Technology 24

2.4	RGW High Order Mode Excitation	25
2.5	RGW Power Divider Based on First High Order Mode	26
2.6	RGW Forward Hybrid Coupler Based on First High Order Mode	27
2.7	Dual Mode Waveguide	27
2.8	Sum and Difference Beam Switching Antenna	28
2.9	Frequency Scanning and leaky Wave Antenna Based on First Higher Order Mode Ridge Gap Waveguide	29
2.10	Design Methodology	30
3	Analytical Design Procedure for RGW Forward Coupler Based on PEC/PMC Waveguide Model	31
3.1	Introduction	31
3.1.1	Hybrid PEC/PMC Waveguide Operation	33
3.2	Hybrids PEC/PMC Coupler	37
3.3	Analytical Design of RGW Coupler	41
3.3.1	Design of Unit Cell and Dispersion Diagram	42
3.3.2	Dispersion Diagram of the Complete RGW	44
3.3.3	Excitation Based on PEC/PMC Circular Bend	47
3.3.4	The Full RGW Coupler	52
3.3.5	Frequency-Tunable RGW Coupler	52
3.4	A Possible Setup for Prototyping the Proposed RGW Coupler	55
3.4.1	Microstrip to RGW Transition	55
3.4.2	Whole Setup Model of 0dB Coupler Include the Microstrip Transition	57
3.4.3	Fabrication and Experimental Results	59
4	Odd Mode RGW-based Devices: Design Procedure	61
4.1	Introduction	61
4.2	First High Order Mode Ridge Gap Waveguide	62
4.2.1	Ridge Gap Waveguide Analysis and Unit Cell	63
4.2.2	Ridge Gap Waveguide Section	63

4.3	Excitation of First High Order Mode by Magic Tee	68
4.3.1	Magic Tee Implementation	68
4.3.2	RGW Excitation by Magic Tee	70
4.4	Excitation of First High Order Mode by L-Shape transition	71
4.4.1	Odd Mode RGW Transition Design	71
4.5	RGW Y-Junction Based on First High Order Mode	74
4.5.1	First High Order Mode RGW Y-Junction Design Procedure	75
4.6	Hybrid Forward Coupler Based on First Higher Order Mode RGW	79
4.6.1	3dB Hybrid Coupler	79
4.7	Design of Dual Mode Ridge Gap Waveguide	84
4.8	High order modes concept of RGW	86
4.8.1	Bandgap of unit Cell	86
4.8.2	RGW Section	86
4.9	Higher order Mode Excitation	88
4.10	Design of Dual Mode RGW	91
4.11	Fabrication and Measurement	94
5	Antennas Design Based on Odd Mode of Ridge Gap Waveguide	98
5.1	4x4-element Cavity Slot Antenna Differentially-fed by Odd Mode Ridge Gap Waveguide	98
5.1.1	Antenna Design	99
5.1.2	4 x 4 Cavity Slot Antenna with Differential RGW Feeding	100
5.1.3	Parametric Study	102
5.1.4	3D Printing Implementation and Measurements	104
5.2	Frequency Beam-Scanning Antenna Array Using Frist Higher Order Mode Ridge Gap Waveguide	109
5.2.1	Single-Element Frequency Beam Scanning Antenna	109
5.2.2	Two-Element Frequency Beam Scanning Antenna.	112
5.2.3	Dual-Beam RGW Frequency Beam-Scanning Antenna.	115

5.2.4	Leaky Wave Antenna based on a First Higher-order Mode Ridge Gap Waveguide	117
	Antenna Design and Theory	117
5.3	Sum and Difference Beam Switching Antenna	123
5.3.1	Antenna Design	124
5.3.2	Results and Discussion	124
6	Conclusion and future work	127
6.1	Conclusion	127
6.2	The future work	129
	Bibliography	131
	List of Publications	144

List of Figures

1.1	Atmospheric absorption at millimeter-wave frequencies [1] © 2009 IEEE.	4
2.1	Some conventional transmission lines; (a) Microstrip Line,(b) Stripline.	11
2.2	(a) Coplanar Waveguide,(b) Grounded Coplanar Waveguide.	12
2.3	(a) Suspended Microstrip Line (b) Inverted Microstrip Line	12
2.4	Typical Metal Waveguide.	14
2.5	Substrate Integrated Waveguide (SIW).	14
2.6	Configurations of: (a) a Ridge gap waveguide, (b) a Groove gap waveguide, (c) an Inverted microstrip gap waveguide, and(d) a Microstrip ridge gap waveguide.	16
2.7	Basic concept of hard and soft surface	17
2.8	Basic concepts of operation of Ideal RGW	19
2.9	Different Views of Ridge gap Waveguide Configuration	19
2.10	Thin wire media	20
2.11	Geometry of the “Fakir’s bed of nails”	21
2.12	Bed of Nails Covered by PEC-Plates	22
2.13	TM and TE dispersion equation of the bed of nails covered by PEC-Plates and light line	23
2.14	The unit cell’s geometry, simulated and theoretical dispersion curves of the TE and TM modes	24
2.15	Flow chart of the design methodology for designing several components and antennas based on the first high order mode RGW.	30
3.1	Equivalent hybrid PEC/PMC waveguide.	33

3.2	Hybrid PEC/PMC waveguide: (a) dispersion curves, (b) cross-sectional electric field distribution for the TEM, TE ₁₀ and TE ₂₀ modes, respectively at $w_r = 13mm$	35
3.3	Field Distribution of the ideal PMC waveguide (a) at width of $w = 5mm$ for $m=0$ and $m=1$ and (b) at $w = 13mm$ for $m=0$ and $m=1$	36
3.4	Hybrid PEC/PMC Coupler, (a) geometry, (b) electric field distribution at 13GHz	37
3.5	dispersion diagram of the common section of the hybrid PEC/PMC Coupler.	38
3.6	S-parameters of 0dB hybrid PEC/PMC waveguide coupler.	40
3.7	Complete Ridge Gap Waveguide configuration.	41
3.8	Periodic bed of nails, (a) geometry and (b) simulated and theoretical dispersion curves of the TE and TM modes.	43
3.9	Comparison between dispersion curves of RGW obtained from HFSS and theoretically, at $w = 13mm$	46
3.10	Dispersion curves for the common waveguide of RGW coupler obtained from, hybrid PEC/PMC theoretical model (solid lines), theoretical analysis of RGW coupler (circles and diamonds) and simulation results of RGW coupler (dashed lines) where $w = 13mm$	46
3.11	Dispersion curves of the RGW coupler and the hybrid PEC/PMC waveguide with width equal to the effective width.	48
3.12	Coupling length versus frequency for both of a 0dB and a 3dB couplers. . .	48
3.13	Circulating hybrid PEC/PMC and Realistic waveguide bends with the corresponding field distributions"	49
3.14	Comparison among the theoretical, Realistic and hybrid PEC/PMC phase and magnitude response of circular bend waveguide: (a) Magnitude response, (b) phase response.	51
3.15	The physical structure of the RGW 0dB coupler.	53

3.16	Full wave simulation for the 0dB RGW coupler at 13 GHz, (a) electric field distribution and (b) magnitude of S-parameters.	53
3.17	The behavior of odd mode versus the air gap height.	54
3.18	The coupling length versus the air gap height.	55
3.19	Full wave simulation for the 0dB RGW coupler at 13 GHz: magnitude S-parameters (S31 and S21) versus the air gap height.	55
3.20	The fundamental mode in Microstrip and metallic ridge gap waveguide.	56
3.21	Microstrip to metallic Ridge gap waveguide transition.	57
3.22	Simulated results microstrip to metallic ridge gap waveguide transition.	57
3.23	The whole setup model of 0dB coupler include the microstrip transition.	58
3.24	Simulated scattering parameters and Electric field distribution of the whole setup model of 0dB coupler include the microstrip transition. (a) Scattering parameters, (b) Electric field distribution.	58
3.25	Pictures of the fabricated individual parts and assembled structure. (a) Individual parts of designed 0dB coupler, (b) Assembled 0dB coupler.	59
3.26	Measured and simulated scattering parameters of the whole setup model of 0dB coupler include the microstrip transition.	60
4.1	The configuration of unit cell and its dispersion diagram. (a) The configuration of the unit cell. (b) Dispersion diagram.	63
4.2	The configuration of wide RGW and dispersion curves of RGW obtained from HFSS. (a) The configuration of wide RGW. (b) Dispersion diagram.	64
4.3	Electric field distribution of the first three modes proposed wide RGW.	65
4.4	Cross sectional fields distribution of the first three modes.	65
4.5	The configuration of RGW with PEC boundary at the middle and its dispersion curves. (a) The configuration of RGW. (b) Dispersion diagram. (c) Electric field distribution of the RGW.	67
4.6	Electric and magnetic field distribution of the RGW first odd mode TE_{10}^{RGW} (proposed wide RGW).	67

4.7	The configuration of the magic tee transition. (a) 3D view with the electric field distribution. (b) Top view right, middle cut left.	69
4.8	The magic tee S-parameters. (a) Magnitude. (b) Phase.	69
4.9	RGW with the magic tee transition. (a) Electric field distribution of the TE_{10}^{RGW} mode in the proposed RGW.	70
4.10	S-parameters of back to back transition.	71
4.11	(a) Odd mode RGW configuration (b) Top view	72
4.12	The magnitude of the proposed RGW odd mode S-parameters	73
4.13	The field distribution for the proposed odd mode RGW transition at 32 GHz.	73
4.14	Y-Junction RGW based on first higher mode with ideal PMC boundary conditions. (a) Structure top view. (b) Simulated electric field distribution . . .	76
4.15	The Y-junction S-parameters. (a) Magnitude. (b) Phase	77
4.16	The Y-junction RGW based on first higher mode with bed of nails. (a) Structure side view. (b) Electric field distribution.	78
4.17	The Y-junction RGW based on first higher mode with bed of nails. (a) Structure top view. (b) Electric field distribution.	78
4.18	3dB Hybrid PEC/PMC Coupler, (a) geometry, (b) electric field distribution at 32GHz.	80
4.19	S-parameters of the proposed 3dB hybrid PEC/PMC waveguide coupler . .	81
4.20	Phase response of the proposed 3dB hybrid PEC/PMC waveguide coupler	81
4.21	3dB Hybrid Coupler, (a) geometry, (b) electric field distribution at 32 GHz. .	82
4.22	Scattering parameters of the 3dB coupler.	83
4.23	Phase difference between Port2 and port3($\angle S_{21} - \angle S_{31}$).	83
4.24	The configuration of unit cell and its dispersion diagram.	86
4.25	The RGW section and its dispersion diagram.	87
4.26	Electric field distribution of (a) Q-TEM mode (b) TE_{10}^{RGW} mode. (c) TE_{20}^{RGW} mode.	88

4.27	The configuration of the magic tee transition. (a) 3D view without the top plate. (b) 3D side view of the magic tee transition.	89
4.28	2D view with the electric field distribution in port2 and port3 (a) the electric field distribution in port2 and port3 when the input from port1, (b) the electric field distribution in port2 and port3 when the input from port4. . .	90
4.29	The magnitude of magic tee S-parameters.	90
4.30	The phase of magic tee S-parameters.	90
4.31	The geometry of the proposed dual-mode RGW structure. (a) Top and side views. (b) 3D view of the RGW.	92
4.32	The field distribution for the proposed RGW dual mode structure. (a) Q-TEM mode. (b) TE_{10}^{RGW} mode.	93
4.33	S-parameters of the proposed RGW dual mode.	94
4.34	The fabricated dual-mode RGW structure (a) individually parts. (b) Assembled parts.	95
4.35	Dual-mode RGW measurements setup.	95
4.36	Dual-Mode RGW results using back-to-back setup. (a) Measurements and simulations obtained from port1 and port2. (b) Measurements and simulations obtained from port3 and port4.	96
4.37	Measurements and simulations the Isolation of proposed dual-Mode RGW.	96
5.1	Magnetic and electric fields distribution of TE ₄₄₀ mode in square waveguide cavity. (a) The electric field in square waveguide cavity. (b) The magnetic field in the cavity and Electric field across the slots.	100
5.2	The geometry of the proposed cavity antenna structure. (a) 3D view of the SIW cavity. (b) Cavity excitation structure. (c) Whole cavity slot antenna structure.	101
5.3	Comparison of the HFSS and CST simulated reflection coefficients and gains of the proposed cavity antenna.	103

5.4	Simulated reflection coefficients and gain of the proposed antenna considering the impact of varying different geometric parameters of cavity feeding: (a) l_{match} ; (b) l_{slot} .	104
5.5	Simulated reflection coefficients and gain of the proposed antenna considering the impact of varying different geometric parameters of the cavity: (a) h_c ; (b) S_c ; (c) L_s .	105
5.6	The fabricated 4 x 4 cavity antenna (a) individually parts. (b) Assembled parts.	106
5.7	Photos of the measurement set up.	106
5.8	Comparison of simulated and measured reflection coefficients and gains of the proposed cavity antenna.	108
5.9	Measured and Simulated radiation patterns of the proposed cavity antenna. (a) 32.75 GHz. (b) 33.5 GHz. (c) 34.5 GHz.	108
5.10	The configuration of an element of the FSA.	110
5.11	Simulated reflection and transmission coefficients of the single-element FSA.	111
5.12	Simulated realized gain of the E-plane radiation pattern for 28,29,30,31 and 32 GHz.	111
5.13	(a) Separated view of the top, bottom and a magic tee transition; and (b) Complete configuration of the FSA array.	112
5.14	Simulated reflection and realized gain of the FSA array.	113
5.15	Simulated realized gain of the E-plane radiation pattern for 28,29,30,31 and 32 GHz.	113
5.16	Simulated E-field distribution in slots for 28, 30, 31,32,33 and 34 GHz.	114
5.17	Simulated realized gain of 3D radiation pattern for 29, 30, 31 and 32 GHz.	114
5.18	Configuration of the dual-beam FSA array line with identical slots on both Y-junction arms.	116
5.19	Simulated realized gain of 3D radiation pattern of dual-beam FSA array for 29, 30, 31 and 32 GHz.	116
5.20	Sketch of center dismantlement leaky wave antenna.	118

5.21	(a) Sketch of a leaky wave antenna; (b) Dispersion diagram; and (c) Comparison of the simulated and calculated angles of maximum radiation of the RGW leaky-wave antenna for the TE_{10}^{RGW}	119
5.22	(a) Complete configuration of the RGW-LWA; and (b) Separated view of the stacked layers with a zoom view close to the slots and a magic tee	121
5.23	Simulated S parameters and gain of the proposed LWA	122
5.24	Simulated realized gain of the radiation pattern for 28,30,32,34 and 35 GHz for feeding from port1 and port2.	122
5.25	Switchable sum and difference radiation pattern.	123
5.26	RGW Dual mode horn antenna views.	124
5.27	Simulated reflection coefficients and gain for both the sum- and difference-beam radiation modes.	125
5.28	Simulated radiation patterns for the sum- and difference-beam radiation modes at center and at the two edge frequencies. (a) 28 GHz, (b) 32 GHz, and (c) 36 GHz.	126

List of Abbreviations

2D	Two-Dimensional
CST	Computer Simulation Technology
HFSS	High Frequency Structure Simulator
PBG	Photonic Bandgap
EBG	Electromagnetic Bandgap
RGW	Ridge gap waveguide
PRGW	printed Ridge gap waveguide
mm-wave	Millimeter wave
PEC	Perfect Electric Conductor
PMC	Perfect Magnetic Conductor
AMC	Artificial Magnetic Conductor
SIW	Substrate Integrated Waveguide
PCB	Printed Circuit Board
MMICs	Monolithic Microwave Integrated Circuit
5G	Fifth generation communication
TEM	Transverse electromagnetic wave
QTEM	Quasi Transverse electromagnetic wave
TE	Transverse Electro wave
TM	Transverse Magnetic wave
NRD	Nonradiative Dielectric
MS	Microstrip
CPW	Coplanar Waveguides
G-CPW	Grounded Coplanar Waveguides

DSW	Dielectric Slab Waveguide
EHF	Extremely High-frequency
FSA	Frequency Scanning Antenna
LWA	Leaky Wave Antenna
DC	Direct Current

Chapter 1

Introduction and Historical Overview

1.1 Introduction

The ongoing demand for high data for wireless communication systems has been growing exponentially in the past few years. One of the highly anticipated solutions to satisfy such demand is to operate at the millimeter-wave (mm-wave) band (30 GHz-300 GHz) [1]. Migrating the operating frequencies to mm-wave frequencies will require new front-end designs for the antenna stage, feeding structures, up/down converting stages and the baseband circuits. The current focus of microwave engineers is to implement efficient microwave components and feeding structures with high-performance metrics.

At the mm-wave band, the traditional technologies (microstrip, coplanar microstrip, stripline, substrate integrated waveguide, and metal waveguide) have many shortcomings related to performance or manufacturing challenges. The printed technologies, such as the microstrip, coplanar, and substrate integrated waveguides (SIW), are appropriate for integrating with other printed circuits and are easy to fabricate. However, they suffer from dielectric losses as the signal propagates in the dielectric substrate, especially at high frequencies. Also, these technologies are hindered by the existence of the cavity resonances when using a closed structure, which has negatively influenced waveguide performance. In addition of the dielectric loss, microstrip and coplanar structures may suffer from radiation loss if they are not perfectly packaged. Surface waves are another critical issue that causes high losses when designing a microstrip network for an array antenna. These unwanted waves have an impact on the radiation pattern of the

antenna [2, 3]. The metal waveguides (rectangular and circular waveguide) are preferred for applications that require low-loss and high power handling [4]. However, they are difficult to integrate with planar circuits, especially at high frequencies.

Ridge-gap waveguide (RGW) technology is a suitable candidate with which to overcome the limitations of the other technologies. RGWs do not suffer from dielectric losses, as the wave propagates in an air-gap between the ridge and the upper plate, and they can be designed in a printed form which allows them to be easily integrated with other circuits [5–8].

However, the utilization of traditional waveguides' higher-order modes may also be considered as a means to improve the performance, simplify the structure, increase channel capacity (multimode transmission), and reduce fabrication cost. Many studies have invested significant efforts into designing the excitation structure for higher-order modes based on different technologies; developing and evaluating several types of transitions and antennas for higher-order modes. Several higher-order modes of rectangular dielectric resonator antennas that use multi-mode operations to improve the impedance bandwidth and gain are presented in [9–11]. In [12], the first higher-order mode (TE₂₀ mode) is excited by using an SIW hybrid coupler and an SIW 90° phase shifter, which then use this transition for feeding an SIW slot array to reduce the number of metal vias. A multimode signal transmission based on generating a TE₂₀ mode in SIW by using a multilayer balun is presented in [13], and two wideband balun transitions are presented to excite TE₂₀ mode in SIW in [14]. Both transitions have a simple structure and broad bandwidth. A millimeter-wave patch antenna fed differentially by a TE₂₀ mode SIW is introduced in [15]; the same study shows that the higher-order-mode in SIW technology provides high radiation gain, a wide impedance bandwidth and a compact size.

Combining the above-mentioned advantages of the mm-wave band and gap waveguide technology, it is clear that using the higher-order mode opens the door for the development of wireless communication, which requires a multi-gigabit per second (Gbit/s) data rate transmission. In this chapter, we first present a brief overview of the properties

of millimeter waves, followed by a brief discussion about the potential problems and difficulties that may appear when using conventional technologies at high frequencies. We finish with a short overview of the characteristics and advantages of RGW technology.

1.2 Millimeter Wave Overview

The millimeter wave spectrum opens the door for the development of wireless communication systems, especially for 5G cellular networks. The huge range of the microwave band, which starts at 3 GHz and ends at 300 GHz (only 5.8 GHz is used presently) remains underutilized. This band is divided into two sub bands: a super high-frequency (SHF) band from 3 GHz to 30 GHz, and a second band from 30 GHz to 300 GHz, called the extremely high-frequency (EHF) band [16, 17].

The several attractive factors that distinguish the millimeter-wave frequency band are its:

1. Wide bandwidth;
2. Multi Gbit wireless communications;
3. License-free bands;
4. Resistance to interference;
5. High security;
6. Frequency re-use; and
7. High gain/narrow beam antennas with small physical dimensions.

These advantages indicate that mm-wave systems could be utilized in several applications such as satellite communications and applications that need high-quality video transmission (gigabit data rates). However, the propagating signal at the mm-wave band is susceptible to high attenuation due to atmospheric absorption. Fig 1.1 shows atmospheric the absorption losses from direct current (Dc) to 400 GHz, revealing where these

losses are especially high at certain frequencies. Atmospheric absorption loss has discouraged the development of high data rate wireless systems capable of covering a wide area, but they have proven to be very suitable for short-distance applications that need high-speed data.

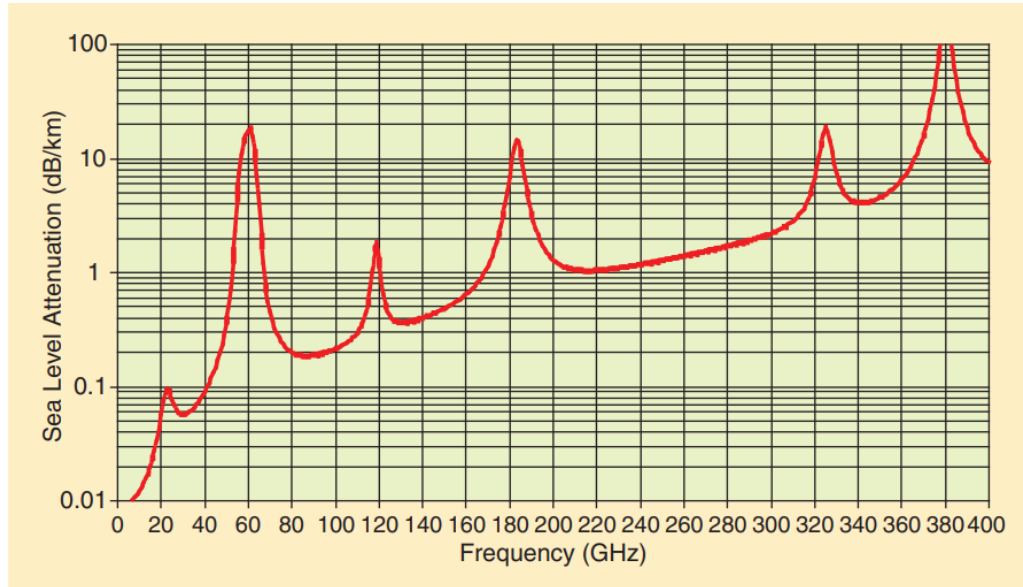


FIGURE 1.1: Atmospheric absorption at millimeter-wave frequencies [1] © 2009 IEEE.

1.3 Motivations and Problem Statement

The demand for high data rates for wireless communication systems is growing more and more, motivating researchers to investigate mm-wave bands (30 GHz-300 GHz) where more spectrum range is available that can provide a multi-gigabit per second (Gbit/s) data rate transmission. However, there are serious challenges related to the propagation loss, dielectric losses, interference effect, multipath, and link blockage by obstructions. Also, designing components to work at mm-wave frequencies with practical, small-sized, easily integrated, low loss, and low cost is a must. Indeed, there is a disparity

between printed guiding structures (microstrip, coplanar, stripline, and substrate integrated waveguides) and non-printed guiding structures (metal rectangular and circular waveguides) in terms of the amount of loss, their size, ease (or not) of manufacture, and cost.

The main mm-wave research challenge is to design a guide structure that is as inexpensive as the microstrip, and that is as low-loss as the conventional metal waveguide. Recent research points to the ridge gap waveguide (RGW) as a very good candidate that combines the advantages of microstrip and metal waveguides at high-frequency bands. The RGW does not suffer from dielectric and radiation losses, as it is a closed structure and the wave propagates in an air-gap region. Also, it can be designed in a printed form using printed circuit board technology (PCB), which is low cost and allows it to be integrated with other circuits. Designing RGW structures using the full-wave simulators takes a long simulation time. Kildal et al. have offered an analytical solution to such a waveguide, but it is complex and has some limitations regarding the dimensions to have a homogenous medium. In our work, we proposed a PEC/PMC hybrid waveguide to model the RGW and give initial dimensions to design components with a simplified analytical equation, a 0-dB coupler is designed based on the proposed equations and accurate dimensions are obtained.

The dominant mode of RGW structure is Q-TEM mode and it has been studied in many reported works. However, higher-order modes of RGW have not taken the same attention as the Q-TEM mode. It is well known that each mode has characteristics different from other modes, and so each kind of mode might suit different applications. Based on this insight, we decided to study the effect of having the first -higher-order mode (the odd mode TE_{10}^{RGW}) propagating through an RGW structure rather than the more usually studied even mode Q-TEM. The first odd mode can be used as a differential feed structure instead of a conventional magic-tee and rat-race coupler. It has the advantage of low profile compared to the magic-tee and the advantage of a wideband 180° constant phase difference compared to rat-race coupler. Another usage of the odd mode is to design a high data rate transmission line by exciting the Q-TEM mode and odd mode on the

same structure simultaneously.

Generally, designing antennas using RGW technology is desired to have high radiation efficiency. Also, the antenna must have a high gain to compensate the path losses. On the other hand, in order to avoid the effect of interference, multipath, and signal blockage, beamforming, beam switching, multi-beam antenna, and reconfigurable beam antenna are required. Though, most of the beamforming networks use complex feeding networks that include phase shifters and/or crossovers that lead to a relatively narrow bandwidth. In this thesis, the odd mode has been used to design a frequency scanning antenna. Also, a sum and difference beam switching antenna based on Q-TEM and odd mode is presented.

1.4 Objectives

The main purpose of the thesis is to develop the concept of a fictitious type of ridge gap waveguide, called the hybrid PEC/PMC waveguide and then design components and antennas based on first higher-order TE_{10}^{RGW} mode RGW which has the functionality to be used to feed a cavity antenna differentially, design a dual-mode RGW, and design a frequency scanning antenna. The objectives are classified into four specific parts:

- Develop a simple theoretical design procedure for the RGW-based components, in which this procedure mainly based on a hybrid PEC/PMC waveguide. This will facilitate and simplify the theoretical analysis of RGWs, which would be rather complicated if an RGW is analyzed directly in its complete form [18]. Furthermore, due to its simplicity and accuracy, this analysis is also used to analyze the transitional bends and hybrid junctions that are the main building blocks of many mm-wave components, such as the six-port junction and the Butler matrix.
- Introduce different methods to excite a first high-order mode RGW, and to then design several components based on the first high-order mode RGW, such as a Y-junction power divider and a forward 3dB coupler, where the fundamental mode in

those components is TE_{10}^{RGW} rather than Q-TEM.

- Design a dual-mode ridge gap waveguide at mm-wave band. Due to the orthogonality of the fundamental mode Q-TEM and the first higher-order mode TE_{10}^{RGW} , these modes can be used for carrying several signals with low interference through the same waveguide. Using the fundamental mode Q-TEM and the first high order mode TE_{10}^{RGW} on the same waveguide offers many advantages. First, the channel capacity is increased, which helps to improve system performance. Second, a dual pattern antenna can be designed, with each pattern corresponding to one mode. Third, the number of pins utilized to build the dual-mode RGW can be reduced compared to the number required for two parallel lines, reducing the fabrication cost.
- The last objective of this work is to use the first higher-order mode in RGW TE_{10}^{RGW} in the design of a frequency scanning antenna array and a cavity slot antenna, both differentially fed by an odd-mode RGW.

1.5 Contributions

This thesis offers the main contributions summarized below:

- A systematic design methodology of a 0dB forward couplers based on the ridge gap waveguide (RGW) technology is presented, which reduces the computational time of full-wave simulators. Based on the designed model, a simple analyzing of transitional bends and phase shifters with accurate calculations is presented. Moreover, the possibility of tuning the coupler center frequency is introduced without the need to use any nonlinear elements [J1];
- Two different methods to excite the first higher-order mode TE_{10}^{RGW} with wide bandwidth is introduced [C1]. These excitation methods enable various components to be designed based on the first higher-order mode RGW;

- Novel Y-junction power divider and 3-dB hybrid coupler based on the first higher-order mode are introduced. Then, a frequency scanning antenna array (FSA) and a leaky-wave antenna (LWA) based on the first higher-order mode TE_{10}^{RGW} are presented;
- New differential excitation mechanism for a 4x4-element cavity slot array antenna is introduced and implemented using the TE_{10}^{RGW} mode of a wide RGW [J2]; and
- Novel dual-mode ridge gap waveguide is introduced and implemented to double the channel capacity of the mm-wave guiding structure. Then, based on the proposed dual-mode RGW, a dual-functional sum and difference beam switching antenna is presented [J3].

1.6 Thesis Organization

The thesis is divided into six chapters and an abstract. The first chapter covers the introduction, the motivation, the objectives and contributions, and a brief overview of mm-wave and conventional waveguides. A historical overview of guiding structures is presented in chapter two, along with the background and basic concepts of the ridge gap waveguide (RGW). The third chapter describes a new systematic design methodology for the RGW using a vertical PMC wall, which models a periodic bed of nails. The same chapter shows an analysis of the phase response of a circular RGW based on the proposed model and the possibility of tuning the coupler center frequency. The fourth chapter presents two different methods to excite the first higher-order mode (TE_{10}^{RGW}), the Y-junction power divider, the 3dB coupler based on the first high order mode of RGW, and a dual mode RGW. Chapter five displays a differential feeding structure using the first higher-order mode (TE_{10}^{RGW}) of an RGW. A frequency scanning antenna array, a leaky wave antenna, and a multi-beam radiation antenna as an application of the dual-mode RGW are also presented in chapter five. Finally, the last chapter summarizes and discusses results obtained in this dissertation and outlines further work.

Chapter 2

Background and Literature Review

This chapter presents a brief literature review of Ridge gap waveguides (RGWs) and some background of the study of RGWs, including their propagation properties, propagation constant, and characteristic impedance. Some works on the high-order excitation mode are also included, along with an overview of several components and antennas based on high order modes and using different technologies. A brief literature review of the dual-mode waveguide and its advantages is presented at the end of this chapter.

2.1 Historical Overview of Guiding Structures

One of the more challenging topics in Radio-Frequency' mm-wave research is the development of guiding structures for millimeter signals, where the basic concepts of the propagation of electromagnetic waves inside the guiding structures are analyzed by solving Maxwell's equations. The major principles of the electromagnetic (EM) waves inside guided structures were established in [19,20]. Based on Maxwell's equations, Helmholtz derived wave equations at the end of the 18th century. The electric and magnetic fields inside guided structures are obtained as solutions of wave equations, which are second-order partial differential equations. Solving these equations in accordance with the structure boundary conditions shows the propagating modes inside the waveguide, in which each mode is a solution for a wave equation, and is in the form of an Eigen function. Propagation modes inside the guided structure depend on the operating frequency, the

fields' polarization, and the guide's shape and dimension. Accordingly, these modes can be classified into the following types:

1. TE modes (Transverse Electric);
2. TM modes (Transverse Magnetic); and
3. TEM modes (Transverse Electromagnetic).

Each of these mode types has a cutoff frequency below which they cannot exist in the guide. In low-frequency bands, the performance of conventional waveguides, such as rectangular, circular, microstrip, parallel plate, coplanar and substrate integrated waveguides is acceptable, but it degrades as the frequency increases. In addition, it is difficult to manufacture rectangular and circular waveguides for use at high-frequency bands. These are just a few of the some limitations in using conventional guide structures in especially in the SHF or EHF (mm-wave) bands.

2.1.1 Microstrip and Striplines, Coplanar and Grounded Coplanar Waveguides, Metal and Substrate-integrated Waveguides

As shown in Fig 2.1 (a), the microstrip is a strip conductor and a ground plane separated by a dielectric material. The quasi-TEM mode propagates between the strip conductor and the ground plane through the dielectric substrate [21]. Since the wave propagates in the dielectric material and the strip conductor is uncovered, the microstrip line suffers from three types of losses, dielectric, ohmic, and radiation loss. These losses become more significant at high frequency bands. Unlike the microstrip waveguide, the stripline confines wave propagation within a substrate between two grounds, as shown in Fig 2.1 (b). The TEM mode propagates between the strip and the top ground, similar to the coaxial transmission line, which is non-dispersive at all frequencies. Moreover, since the strapline confines wave propagation between two ground planes, there is no wave leakage, which provides high isolation between adjacent circuits (unlike the microstrip waveguide).

The coplanar waveguide (CPW) is another form of transmission line realized by including the conductor strip between two ground conductors with a certain width, as shown in Fig 2.2 (a). In this technology, the fields propagate inside the dielectric substrate as a quasi-TEM mode at low frequencies and as a TE mode at high frequencies. As the fields are not totally confined within metallic boundaries, there is some leakage in the fields. The loss due to this energy leakage is partially controlled by tuning the ratio between the width of the central strip and the substrate's thickness, in which 1:2 is the optimum ratio. The CPW has low dispersion losses in large part because it supports quasi-TEM mode. Moreover, it is easy to fabricate. However, the CPW suffers from dielectric losses and surface waves.

The grounded coplanar waveguide (GCPW) is similar to the CPW, but with a ground plane at the bottom of the substrate and side strips grounded through a metallic substrate via holes. As shown in Fig 2.2(b), the ground is used at the bottom of the substrate to protect the structure from any active components in lower layers when integrated within a system. The GCPW has even lower losses than the CPW, although it still suffers from dielectric losses. When the GCPW is integrated and packaged inside an enclosed system, some cavity modes may propagate and affect the performance [22].

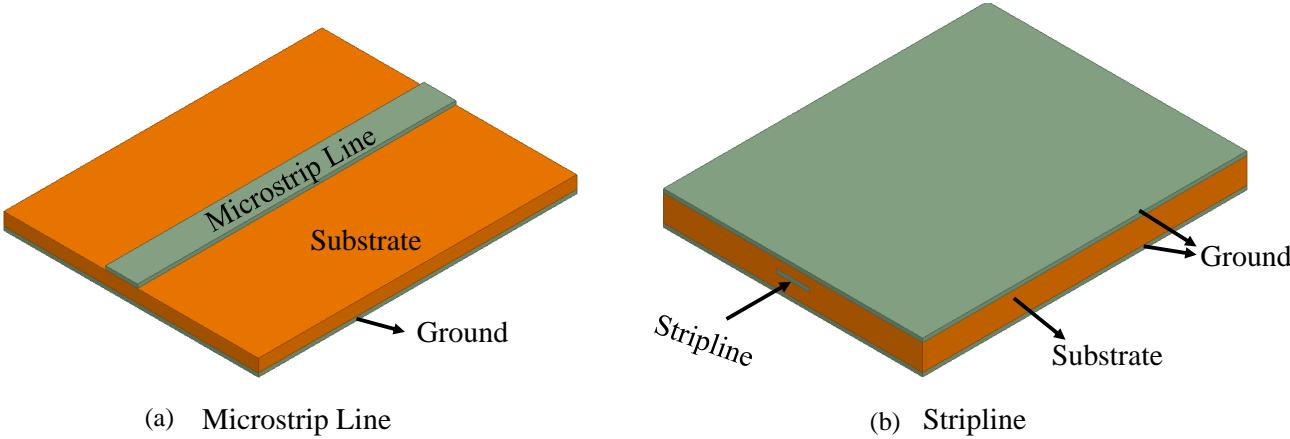


FIGURE 2.1: Some conventional transmission lines; (a) Microstrip Line,(b) Stripline.

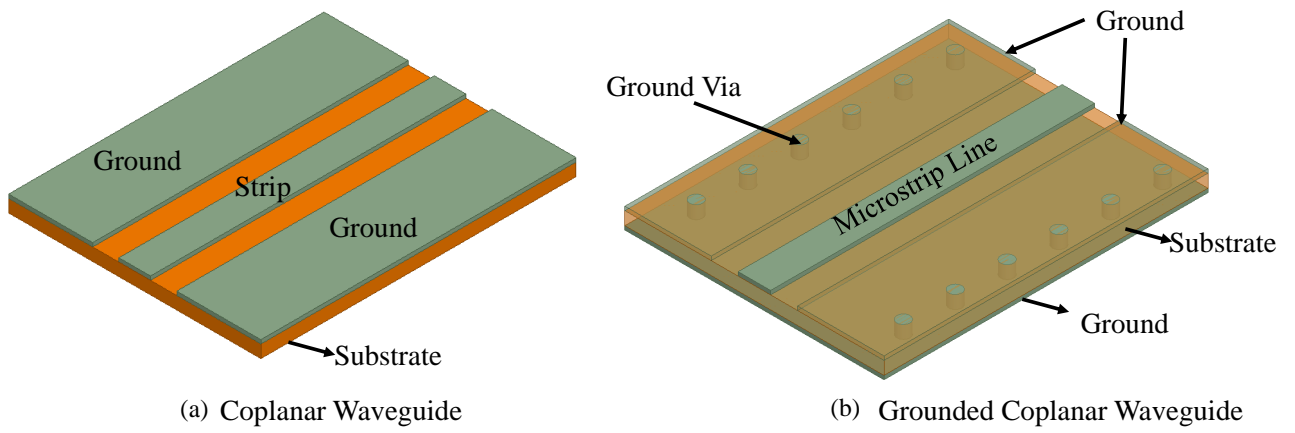


FIGURE 2.2: (a) Coplanar Waveguide,(b) Grounded Coplanar Waveguide.

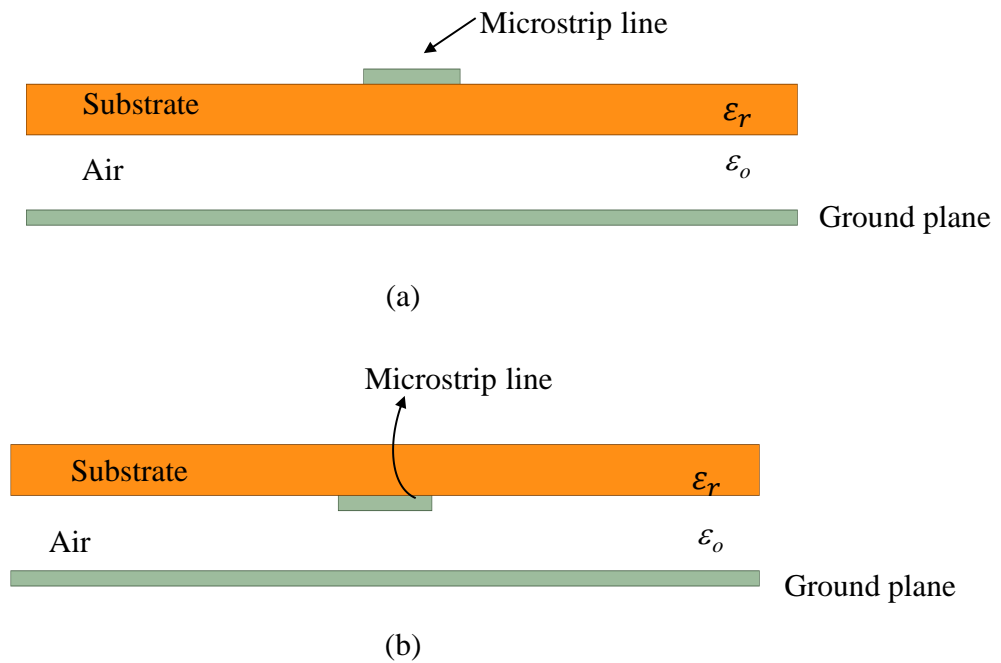


FIGURE 2.3: (a) Suspended Microstrip Line (b) Inverted Microstrip Line

Various technologies have been developed to reduce dielectric loss, such as a suspended microstrip line, which includes an air gap between the ground plane and the dielectric substrate, as shown in Fig 2.3 (a). The suspended microstrip line is especially effective at mm-wave frequencies, as it offers low losses compared to conventional microstrip lines [23,24]. Fig 2.3 (b) shows the configuration of an inverted microstrip, which incurs low losses compared to conventional microstrip lines because the field confines the air between the ground plane and the bottom of the substrate. However, the radiation losses will increase due to the larger air gap between the ground plane and the bottom plane of the substrate. Thus, a new guiding technology is still needed, one that can solve all the above-mentioned problems simultaneously. The dielectric loss is not the only problem for these technologies; the conductive losses become more significant whenever the narrower metal stripline is used to match 50Ω line impedance.

Figs 2.4 (a) and (b) show the traditional rectangular and circular metal waveguides, respectively, which guide waves of both TE and TM modes. Even though TE and TM modes are subjected to dispersion loss, they have much lower losses than transmission lines that support the TEM mode. In general, these waveguides are passive components, and they have a very low loss level. Despite these features, traditional metallic waveguides are costly, especially at the mm-wave spectrum, due to their complexity [25,26]. Another drawback of these waveguides is their bulky structure, which makes it difficult to integrate them with the other components to form a single model. Moreover, when joined with other hardware components, like PCB components and planar monolithic microwave integrated circuit devices (MMICs), the performance degrades at the millimeter-wave band due to leakage loss at the joints. Hence, these hollow waveguides are not the right solution for millimeter-wave applications.

The substrate integrated waveguide technology (SIW), shown in Fig 2.5, is presented in [27,28]. Basically, the configuration of an SIW is similar to that of a rectangular waveguide filled with a dielectric in which the SIW is a dielectric substrate with a metal plate on top and bottom, and metalized holes act as a metallic sidewall. This technology is now considered to be the most promising technology for the realization of millimeter-wave

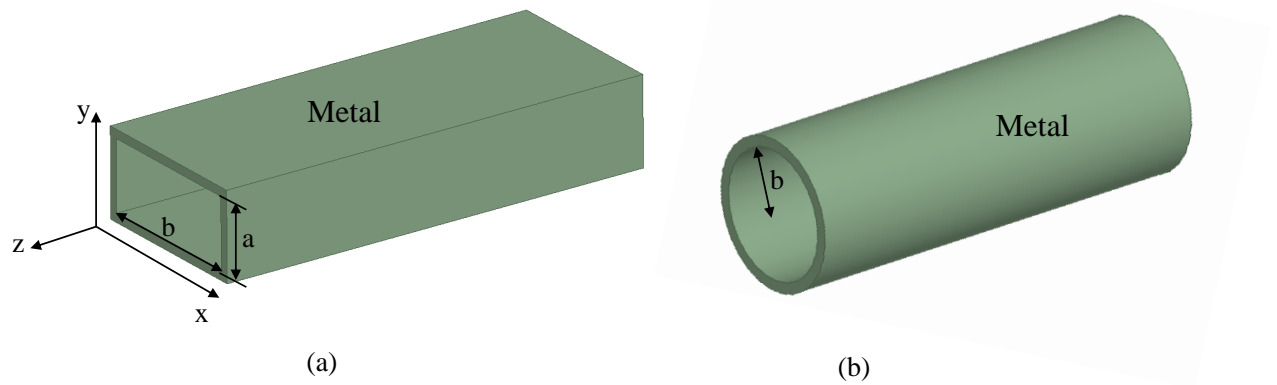


FIGURE 2.4: Typical Metal Waveguide.

system's components as it offers a compact waveguide that is flexible enough to integrate with PCB technology. The fields inside the SIW structure can be guided in the form of TE modes, which is the dominant mode. However, this technology is subject to dielectric losses, as in microstrip transmission lines, especially at the mm-wave range, which is a significant drawback [28,29].

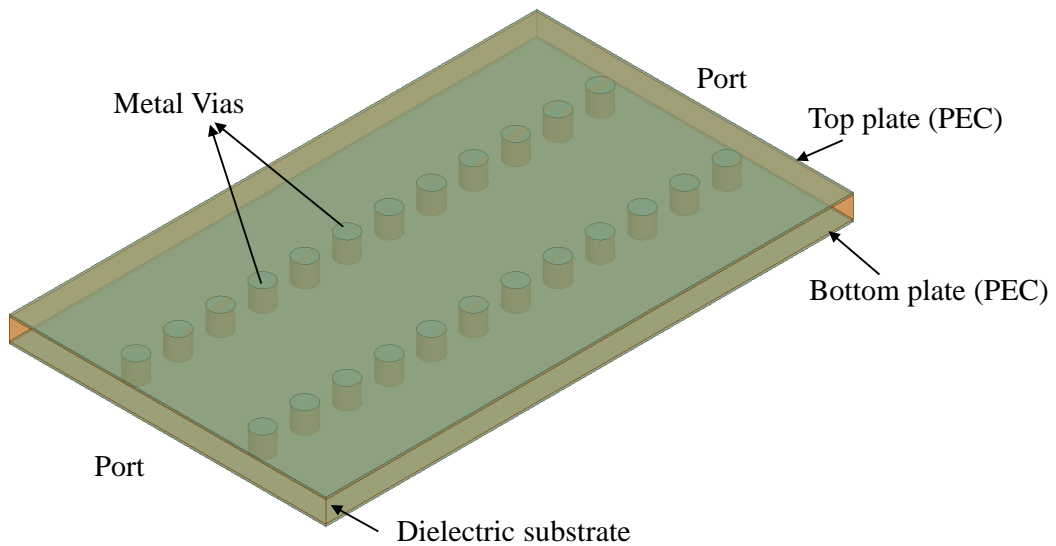


FIGURE 2.5: Substrate Integrated Waveguide (SIW).

2.1.2 Gap Waveguide Technology

Ridge gap waveguide (RGW) technology was introduced over the past decade [30,31] as a new version of guiding structure that offers a high potential to overcome the problems of traditional technologies. Moreover, it can be used to design millimeter components and antennas. The RGW guides the wave in the form of a quasi-TEM mode, in which the artificial perfect magnetic conductors' (PMC) boundary around the ridgeline stops the leakage and confines the wave, so that the wave propagates inside an air gap between the ridgeline the top plate. Because the wave is confined and propagated in air, gap waveguides are not subjected to dielectric losses as in the microstrip and SIW technologies. Also, unlike metal waveguides, a gap waveguide does not need any electrical contacts. Moreover, the RGW can be implemented in a printed form (PRGW) for easy integration with other planer system components. The gap waveguide can be classified into the following types:

1. Ridge gap waveguide;
2. Groove gap ;
3. Inverted microstrip gap ; and
4. Microstrip ridge gap waveguide.

In ridge gap waveguides, the field propagates in the form of a Q-TEM mode along the metal ridge, as shown in Fig 2.6(a), while in groove gap waveguides, the field propagates as a TE mode along the groove as shown in Fig 2.6(b). The third and fourth forms of gap waveguide are called microstrip and inverted microstrip gap waveguide, respectively, where the field propagates in the air gap between the upper plate and the stripline in the form of a Q-TEM mode as shown in Fig 2.6(c,d).

As can be concluded from the characteristics of traditional waveguides, there is still a need for suitable guiding technology for mm-wave frequency bands. Although the metal waveguides have the most excellent performance concerning the loss and power handling, the insufficiency to achieve the electrical contact between the separate portions,

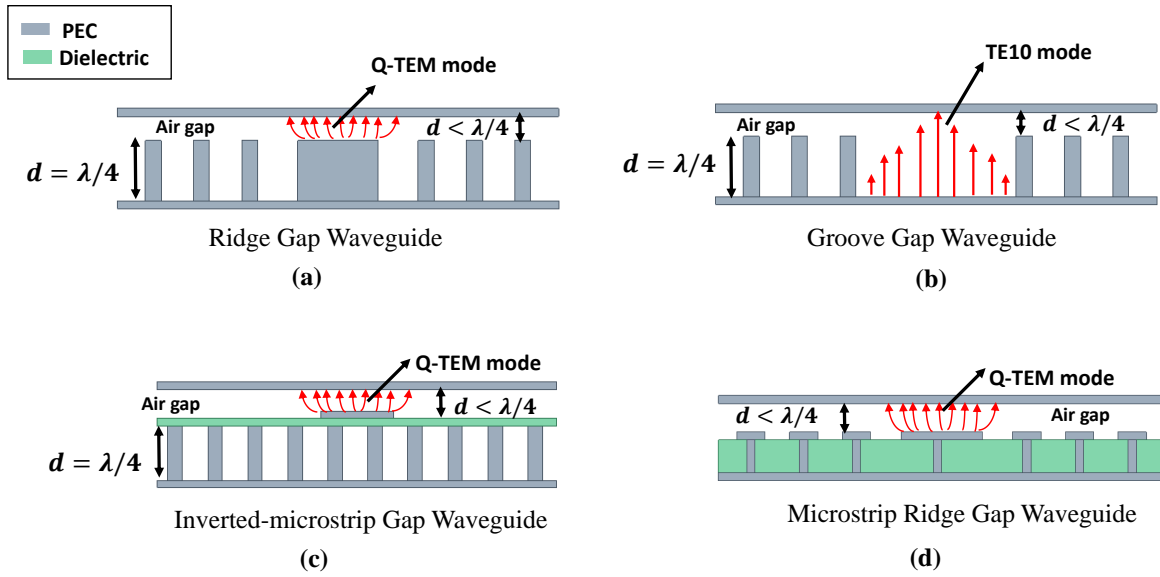


FIGURE 2.6: Configurations of: (a) a Ridge gap waveguide, (b) a Groove gap waveguide, (c) an Inverted microstrip gap waveguide, and (d) a Microstrip ridge gap waveguide.

the electric contact can be realized by deep-brazing, screwing, or diffusion bonding, techniques. However, as working at mm-wave frequencies, the physical dimensions decrease, in which high precision technology is needed for industrialization, which increases the cost. On the other hand, most all the planar waveguide technologies that based on propagating the wave inside the dielectric, which have high losses that led to the low-efficiency device, especially at the mm-wave band. Also, microstrip technology suffers from radiation loss. Consequently, there is an extreme need for appropriate guiding technology that can combine the characteristics of metal waveguides and the characteristics of planar waveguide technologies.

2.2 Ridge Gap Waveguide (RGW) Concept

Many applications based on hard and soft surfaces have proven useful for improving the performance of antenna feeding structures. Periodic hard and soft surfaces can be used to control the field distribution of microwave components and antenna apertures by means

of their varying surface impedances. Photonic bandgap (PBG) structures and electromagnetic bandgap (EBG) structures are two of the basic hard and soft surface structures in this field. The concept of hard and soft surfaces is demonstrated in Fig 2.7, in which the corrugations consist of successive metallic strips and grooves. The depth of the grooves are all quarter-guided wavelengths at the operating frequency, and these grooves must be filled with material that has a permittivity larger than the permittivity of the medium above the surface. The strips and grooves act as a PEC-PMC surface. It can be observed that when the strips and grooves are in the same orientation as the wave propagation, the structure represents a hard surface, while it represents a soft surface when they are orthogonally-oriented above each other [32].

In the proposed analysis, the soft and hard surfaces are considered to be one-dimensional when the periodicity of the strips and grooves are in one direction. Other periodic structures have been introduced, in which the periodicity is in two or three dimensions, such as the above-mentioned EBG structures. The main motivation for using such periodic structures is to obtain a high surface impedance in order to eliminate surface waves from a dielectric substrate [33]. Many of these structures have been used to improve the performance of devices such as antennas, waveguide structures, and filters, etc. [34-36].

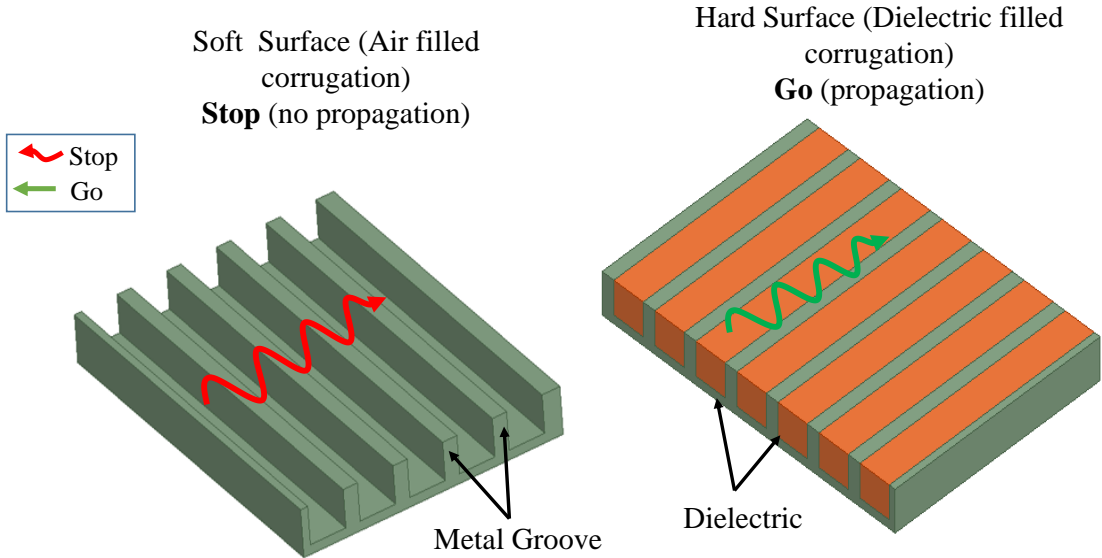


FIGURE 2.7: Basic concept of hard and soft surface

In [18], the quasi-TEM modes can propagate on the ridge of the corrugations as long as the corrugations are covered by a metallic plate, where the distances between them are less than a quarter wavelength. This concept is similar to that of the PEC and PMC strips with metal covers at less than quarter-wavelength distances. The wave in this kind of structure propagates along the longitudinal direction and is prevented from propagating along the other directions by means of the periodic grooves. The development of the RGW was inspired based on this concept [30].

2.2.1 Ridge Gap Waveguide Structure

Ridge Gap waveguide (RGW) technology is an extension of the above-mentioned soft and hard surfaces. Kildal [30]] was the first to show how these surfaces can guarantee the guidance needed for the operation of a waveguide. Fig 2.8 illustrates the basic conceptual geometry of the RGW. In the ideal case, a RGW consists of two horizontal PEC plates surrounded by PMC plates on the left and right sides, as shown in Fig 2.8. In this design, the distance between the top and bottom plates should be less than a quarter of the guided wavelengths at the operation frequency in order to stop the propagation of any mode supported by the RGW. In this case, all the modes between the PEC and the PMC plates are prevented from leaking inside of the periodic bed of nails. Meanwhile, the TEM mode propagates on the ridge, guided by the two horizontal PEC plates [31]. However, the PMC boundary does not exist naturally, and so a horizontal Artificial Magnetic Conductor (AMC) may be used as an equivalent model for the periodic bed of nails. Therefore, the design of an AMC is necessary to stop the modes of operation from propagating through the bed of nails. Fig 2.9 shows different views of a three-dimensional RGW image. The main concept is based on using a quarter wavelength bed of nails on both sides of the ridge to form a PMC surface and to cover them with a metal plate. In this case, the propagation path is between the ridge and the top plate. All the modes between the bed of nails and the top plate are blocked while the Quasi-TEM mode propagates along the ridge in the gap between the two PEC plates. The bed of nails is the

main element in the gap waveguide structure, which achieves the functionality of a PMC surface. The bandwidth of the RGW is directly related to the stop band of the unit cell.

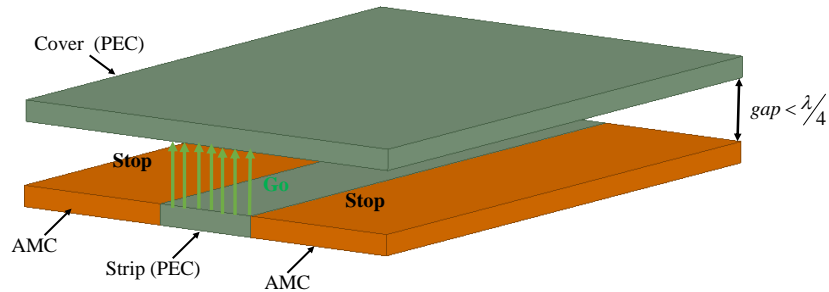


FIGURE 2.8: Basic concepts of operation of Ideal RGW

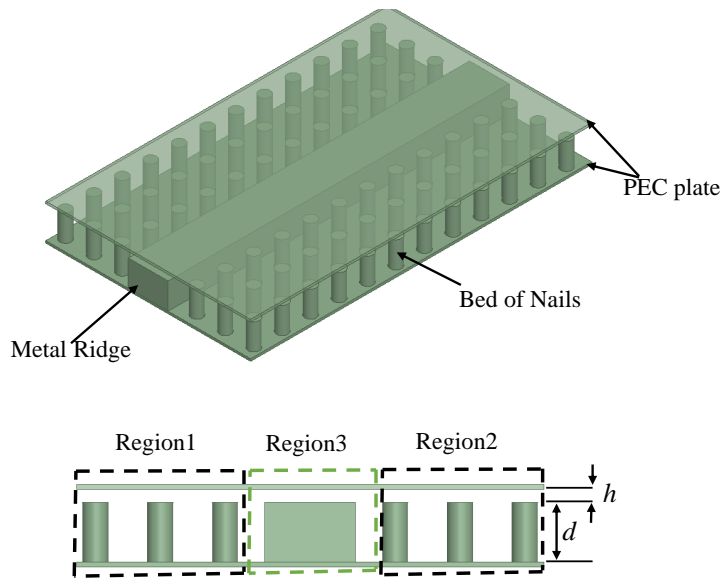


FIGURE 2.9: Different Views of Ridge gap Waveguide Configuration

2.2.2 Bed of Nails Operation

Understanding the RGW concept and its analysis makes it possible to find the solution of the fields in the three regions shown in Fig 2.9 . The response of the electromagnetic propagation through thin wire media as shown in Fig 2.10 is studied in [37]. This analysis shows that the medium is described by a permittivity tensor, which is frequency-dependent. The dispersion diagram of the unit cells is studied theoretically and then verified by using a commercial software (HFSS). The bed of nails configuration is shown

in Fig 2.10, where the cells are formed by metallic cylinders with radius b , height d , and with period a . The permittivity of such medium is a frequency dependent quantity as given in [37].

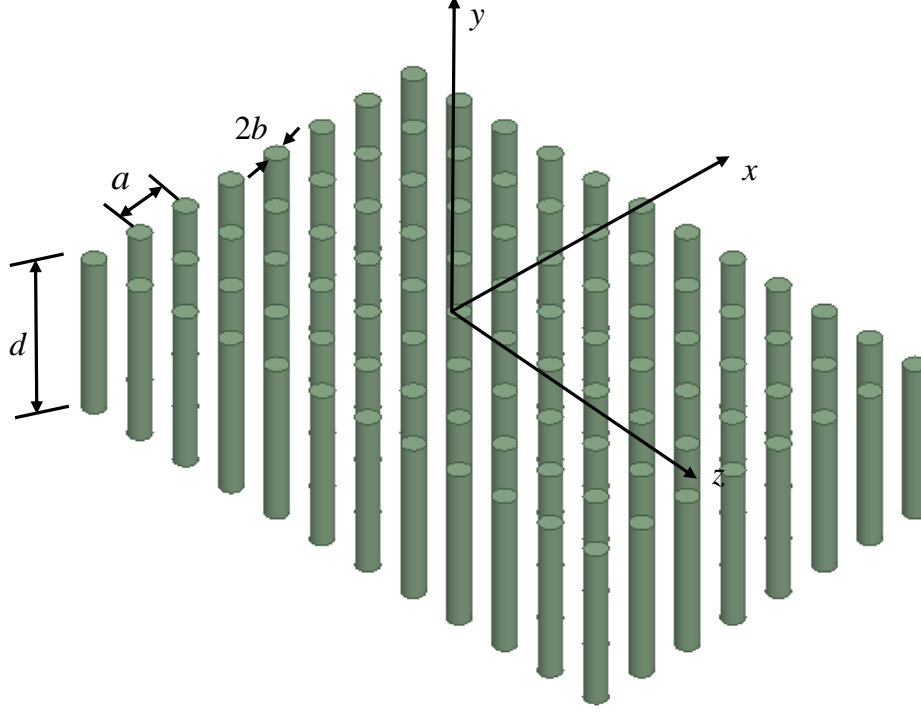


FIGURE 2.10: Thin wire media

$$\epsilon_{yy}(\omega, k_y) = \frac{1 - k_p^2}{k_h^2 + k_y^2} \quad (2.1)$$

where $k_h = \sqrt{\epsilon_h}k$, ϵ_h is the permittivity of the host medium, selected to equal unity for simplicity, k is the wavenumber and k_p is the plasma wavenumber [37] where

$$k_p = \frac{1}{a} \sqrt{\frac{2\pi}{\ln(\frac{a}{2\pi b}) + 0.5275}} \quad (2.2)$$

This model is valid only when $a/d, a/\lambda \ll 1$ as presented in [18].

2.2.3 Bed of Nails Region Downed by a PEC Ground Plane

In Fig 2.11, metallic pins are connected to a PEC ground plane. This structure is called Fakir's bed of nails. Fakir's bed of nails was studied in [38] in order to examine the

reflection properties of TE and TM modes. That work reported that this kind of medium can support three modes: a transverse electromagnetic TEM mode, a transverse magnetic TM-y mode, and a transverse electric TE-y mode [38]. Considering the matching points at the air-medium interface, the reflection coefficients of the TE and TM modes can be calculated by exciting the surface of a Fakir bed of nails with a plane wave, as shown in Fig 2.11.

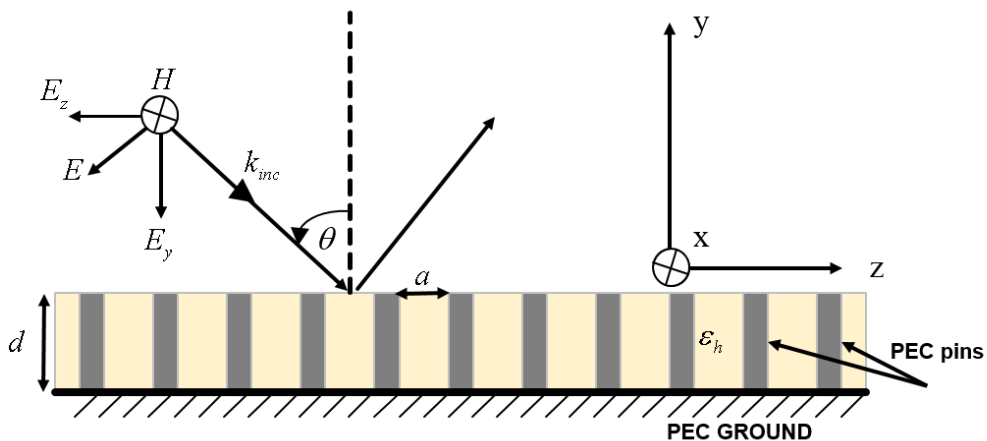


FIGURE 2.11: Geometry of the “Fakir’s bed of nails”

2.2.4 Bed of Nails Covered From Both Sides by PEC-Plates

By covering the upper and lower sides of the bed of nails with bottom and top metallic plates, as shown in Fig 2.12, a parallel plate waveguide (PPWG) is formed. The top plate is a PEC plate and the bed of nails, together with the bottom plate, act as a homogenized surface as explained in the previous section. The wave in such structures bounces in the gap between the two surfaces as illustrated in Fig 2.12. By applying the boundary conditions, the propagation constant can be derived in the y-direction for both cases of the TE and TM modes. The TE and TM dispersion equations of this periodic structure can be formulated as follows [18]:

For the TE mode,

$$k_y = \frac{\pi}{h + d} \quad (2.3)$$

where k_y is the propagation constant in y-direction and, For the TM mode,

$$\frac{k_y}{k} \tan(k_h h) + \left[1 - \frac{k^2 - k_y^2}{k_y^2 + k^2 - k_y^2} \right] \tan(kd) + \frac{k^2 - k_y^2}{k_p^2 + k^2 - k_y^2} \frac{\sqrt{k_p^2 - k_y^2}}{k} \tan\left(\sqrt{k_p^2 - k_y^2} d\right) = 0 \quad (2.4)$$

The value of k_y is the solution of a transcendental equation which is obtained from bouncing the wave in the gap between the two surfaces, as shown in Fig 2.12. The periodic bed of nails' dimensions are chosen to be the same as the dimensions presented in [18], where the height of the unit cell is $d = 7.5mm$, radius $b = 0.5mm$, air gap is $h = 1mm$ and the unit cells' period $a = 2mm$.

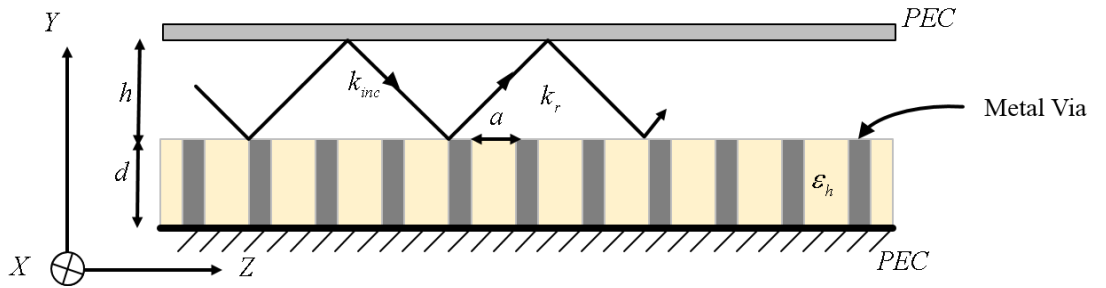


FIGURE 2.12: Bed of Nails Covered by PEC-Plates

A Matlab code is then used to solve this equation. The dispersion curves (k_y^{TE}, k_y^{TM}) and the dimensions of the periodic bed of nails are presented in Fig 2.13. As illustrated in the Fig 2.13, the TE solution does not change with the frequency. The TM solution is shown in the same figure, where the graph is divided into three regions. The first and third regions start from zero to $f(d = \lambda/4)$ and $f > (d = \lambda/4)$, respectively, where k_y is purely imaginary. This means that there is a TM wave that propagates on the surface of the pins. The second region consists of two sub-regions, both of which are purely real.

In the region between $f(d = \lambda/4)$ and $f(d + h = \lambda/2)$, k_y is greater than the value of light line, which means that the attenuation will be in all the directions along the surface. Therefore, this region represents the stopband of this structure. The dispersion diagram in Fig 2.13 clearly shows the stop band of the periodic medium, where the dispersion relation is the relationship between the frequency and the propagation constant in the z-direction, which can be written as

$$k_z = \sqrt{k^2 - k_y^2} \quad (2.5)$$

The dispersion curves of the periodic bed of nails are presented in Fig 2.14 based on (2.3)-(2.5). The accuracy of the resulting dispersion equations is confirmed when they are compared with simulation results obtained from the HFSS eigen mode solver.

Fig 2.14 shows that in the frequency range between 10 and 17GHz, there is no solution for (2.3) and (2.5) that gives real solution for (2.5). This means there are no waves propagating on the bed of nails within this band of frequencies.

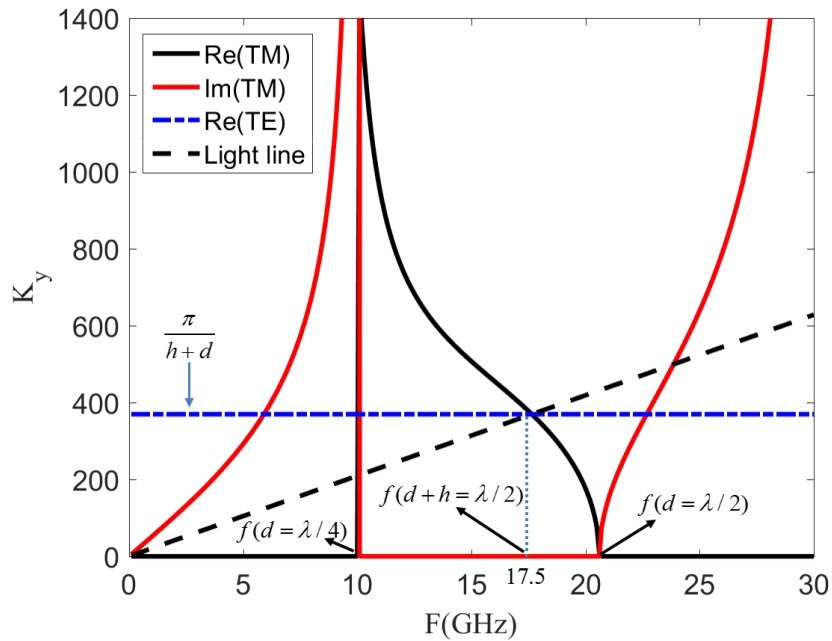


FIGURE 2.13: TM and TE dispersion equation of the bed of nails covered by PEC-Plates and light line

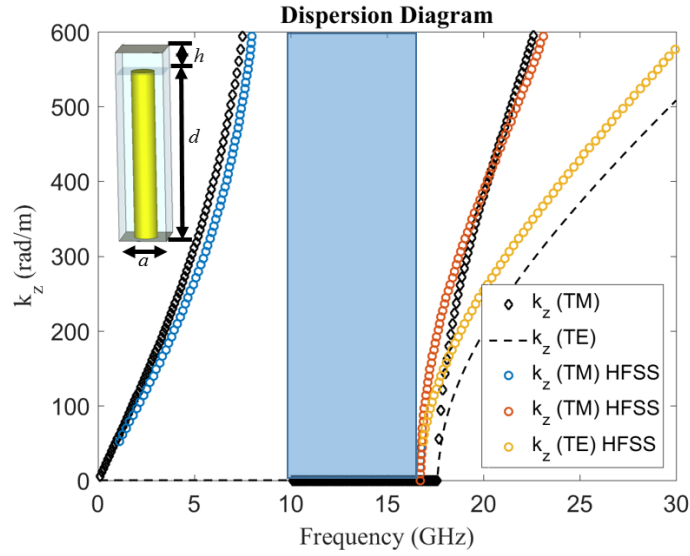


FIGURE 2.14: The unit cell's geometry, simulated and theoretical dispersion curves of the TE and TM modes

2.3 Analytical Design Procedure for Forward Wave Couplers in RGW Technology

Due to the advantages as mentioned earlier of the ridge gap waveguide, it is being considered as a promising candidate for high-frequency applications, especially for the fifth-generation (5G) applications of wireless technology [39, 40]. RGW technology is also a remarkable candidate for the implementation of slot array antennas [41–43]. Therefore, it is extremely important to have a clear theoretical design procedure for RGW-based structures.

Most of the published works about microwave components based on RGW technology mainly rely on approximate or empirical equations. For example, a design procedure for the hybrid couplers was presented in [44], in which the coupling length of the coupling section is calculated by empirical expression. However, the long processing time for optimization is needed, which led to complicate the design procedure for such microwave components. In order to reduce the processing time, an ideal PEC-over-PMC ridge gap

waveguide is presented in [45] for the design of a model of a stripline. This model represents a good approximation, thereby reducing the time need for time-consuming full-wave simulators.

A theoretical analysis of the fundamental and the first higher-order mode in gap waveguide has been investigated in [18, 30, 46]. In [18, 46], the dispersion diagrams of both modes are obtained in an analytical form. This facilitates analyzing hybrid couplers with precise calculations, which will bring the dispersion characteristics under control to design components in the required frequency band. However, those models introduced in [18, 46] are complicated and valid whenever the period of the pins much smaller than the height of the pin and the period of the pins much smaller than the wavelength.

In this work, we develop the concept of a fictitious type of ridge gap waveguide, called the hybrid PEC/PMC waveguide. This will simplify and facilitate the theoretical analysis of RGW, which would be rather complicated if an RGW is analyzed directly in its complete form. Furthermore, due to its simplicity and accuracy, this analysis is also used to analyze the transitional bends, hybrid junctions, and leaky-wave antenna.

2.4 RGW High Order Mode Excitation

The employment of higher-order modes for wireless communication system design is promising at mm-wave bands. Many higher-order mode antennas and components based on substrate integrated waveguide (SIW) have been implemented recently, and several transitions have been utilized to excite higher-order mode in SIWs [47–49]. A simple structure of an SIW slot array antenna based on high order mode (TE₂₀) was presented in [12]. Another technique was used in [13], where a multilayer balun was used to excite the high order mode (TE₂₀) of the SIW in order to design the multimode signal transmission.

All the above-mentioned transitions are designed for the high order mode of the SIW. Relatively little research has been done on the high order mode of the RGW. With the increasing number of applications for using the RGW in wireless communication systems,

RGW higher-order mode components and antennas have become more attractive to the researchers. One such effort is [50], in which a magic tee was designed to feed a leaky wave slot array antenna based on RGW. In this thesis, two different methods to excite the first higher-order mode TE_{10}^{RGW} with wide bandwidth is introduced, which opens the door to design components and antennas based on high order mode RGW technology.

2.5 RGW Power Divider Based on First High Order Mode

A low loss feed network is desirable for building an array antenna, and the RGW can be used to build low loss feed network. A number of T-junction power dividers have been designed and investigated using the ridge gap waveguide technology [51, 52]. In [53], a Y-shaped power divider based on a printed RGW is designed to feed two leaky-wave antennae (LWA) subarrays, which provide backward scanning and a high gain antenna. The studies in [54, 55] present a 1:4 power divider designed to feed a one-by-four linear slot array antenna. And, single T-junction was designed in order to build a two-by-two slot antenna array based on RGW technology in [56].

All the above-mentioned power dividers are designed based on the dominant mode of the RGW, namely, the Q-TEM mode. However, there is not enough information about designing power dividers or slot array antennas based on higher-order mode RGWs. Due to the increasing number of publications that use the RGW, especially in high-frequency bands, higher-order mode RGW components and antennas are attracting more research attention. To date, except for the leaky-wave antenna covered in [50], there have not been any publications on RGW components and antennas. Therefore, one of the primary purposes of the thesis is to introduce the first high order mode power divider based on RGW technology. We introduce a high order mode single Y-junction power divider for the first time in this thesis. This power divider is applied to the design of RGW frequency scanning RGW antenna.

2.6 RGW Forward Hybrid Coupler Based on First High Order Mode

Our literature review shows that, there has been no work reported on designing forward couplers based on a high order mode RGW. All the available couplers based on RGW technology have been designed and analyzed for the dominant mode, namely, the quasi-TEM mode. A forward 3dB coupler based on RGW technology is designed and analyzed here for the first high order mode, namely, the TE_{10}^{RGW} mode.

2.7 Dual Mode Waveguide

With the enormous development in using the ridge gap waveguide to design microwave and millimeter wave components and with the limitation of channel bandwidth, it becomes imperative to concentrate on the increase of channel capacity of RGW. The most effective way to achieve that is by generating two orthogonal modes on the same guiding structure.

The multimode transmission concept is applied in [13] by using the TE₁₀ and TE₂₀ modes to provide a high data rate to an SIW interconnect. Meanwhile, the bandwidth of the TE₁₀ channel is limited by the cutoff frequency of the TE₂₀ channel. That method uses two separate bands for each mode, contrary to the orthomode transducer (OMT), which uses the same band with different polarizations. Moreover, the SIW technology is subjected to the dielectric loss as the wave propagates in the dielectric substrate.

OMT has been employed in antenna feeding networks to transmit and receive orthogonal modes through the same waveguide [57, 58]. But, the OMT is large and bulky. One approach to design a planar orthomode transducer (OMT) on microstrip technology is reported in [59], which employed a rat-race coupler to create one polarization and a single feed to generate another polarization, with good isolation between them. However, this design has a narrow band.

In this work, we introduced a dual-mode based on RGW technology to double the channel capacity of the millimeter waveguiding structure. The proposed design depends on the orthogonality of the fundamental and the first higher-order mode. The advantage of the proposed work is the use of the same frequency band for both modes simultaneously. Also, the proposed design has a wide band with high isolation. As the wave in RGW propagates in the air gap, the signal is not subjected to the dielectric loss as in SIW technology.

2.8 Sum and Difference Beam Switching Antenna

The millimeter-wave frequency band has attracted more research attention recently, since this band offers high data rates. However, working at the mm-wave band is challenging, as the performance of the communication system is decayed due to losses, the interference effect, multipath systems, and link blockage by obstructions. Generally, the losses are compensated by using high gain antenna systems, and to avoid the effect of interference, multipath and signal blockage beamforming techniques, switched beam antenna, multi-beam antennas and reconfigurable beam antennas are required. Beamforming is commonly achieved by varying the phase of each element of an array antenna, in which signals are transmitted from the antenna elements in-phase in a specific direction. The beamforming techniques are classified into fixed and adaptive beamforming techniques. The fixed or switched beamforming techniques include the Butler matrix, Blass matrix, Rotman lens, and Nolen matrix. However, the Butler matrix, Blass matrix, and Nolen matrix are mainly narrow band due to the phase shifter, while the Rotman lens occupies a large area and very lossy due to the dummy load.

A diverse system requires different radiation characteristics (single beam, dual-beam pattern, single, or dual polarization) or the ability to function at different frequency bands. For example, in urban areas, where many users are using a system with a limited bandwidth, the chance of interference increases. A switchable beam antenna can overcome

this issue by covering multiple non-adjacent areas, and hence making a space multiplexing. Using switched beam antennas has many other advantages such as saving energy, avoiding noise, and improving the system security [60,61]. Moreover, the switched beam antenna is able to switch the main beam to a particular direction. Therefore, it is able to cover a large area by pointing the main beam.

Switched beam antennas are essential for designing smart antennas and adaptive systems, and have attracted much attention in the past decade. Several switched beam antennas were designed and presented rather recently [62–64]; most of these designed antenna achieved beam steering or switching by using diodes or switches. A switched beam antenna is mainly dependent on using active elements and switches, but the diodes and switches introduce additional loss and complexity to the system.

This thesis presents a sum and difference beam switching antenna based on dual-mode RGW. The proposed antenna has a wide bandwidth and can generate two radiated beams with reasonable high gain for the single and dual beam patterns. All these features help to improve wireless communications links [65,66].

2.9 Frequency Scanning and leaky Wave Antenna Based on First Higher Order Mode Ridge Gap Waveguide

In general, the frequency scanning antenna (FSA) and leaky-wave antenna (LWA) are ones of the traveling wave antenna family, in which they can be designed to achieve high gain and directional beam. They have been received a significant consideration of the antenna designers due to their abilities to produce a steering beam [67,68]. In addition to the abilities to produce a steering beam, the impedance bandwidth of FSA and LWA are wider than the phased array and slot antenna array. Moreover, those kind of antennas do not need any complex or lossy feed network. To design of frequency-scanning antennas, the frequency bandwidth, the beam scanning angle, and the loss in the traveling-wave antenna must be considered. Frequency-scanning antenna is based on the phase-shifting

induced, between successive slots, by the traveling wave in the waveguide [69]. The conventional metal waveguide offers a low loss as the wave propagates in the air. However, it is bulky, which makes it hard to be integrated with the other planar components. On the other hand, FSA and LWA based on microstrip or SIW technology are presented in [70–73]. Yet, the gain is relatively low due to the radiation and dielectric losses in the microstrip line and dielectric loss in the SIW structure.

In this thesis, frequency scanning and leaky-wave antenna based on RGW technology are designed using the first high order mode. The proposed antennas have good performance in terms of band width, gain, wide scanning angle, and losses.

2.10 Design Methodology

In this section, the design methodology for the proposed factitious type of waveguides referred to as the hybrid PEC/PMC waveguide and several antennas, components based on first higher-order mode RGW are shown in Fig 2.15.

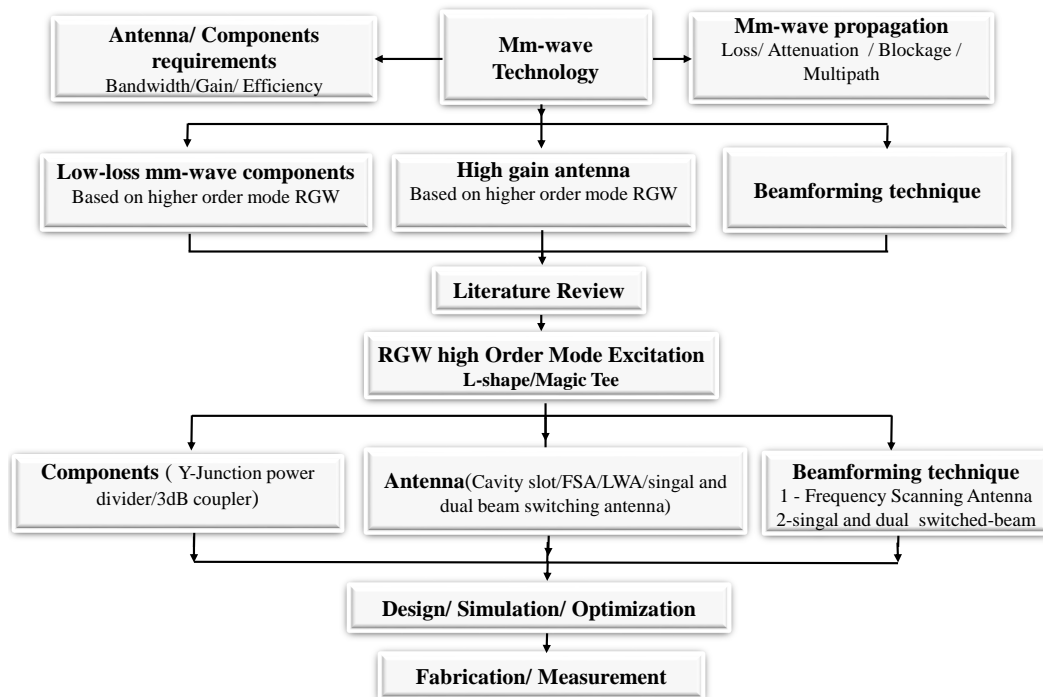


FIGURE 2.15: Flow chart of the design methodology for designing several components and antennas based on the first high order mode RGW.

Chapter 3

Analytical Design Procedure for RGW Forward Coupler Based on PEC/PMC Waveguide Model

3.1 Introduction

Several technologies have been utilized to implement the forward wave couplers, as earlier mentioned in the Chapter 1. Unfortunately, all the mentioned technologies have some issues that could adversely affect the hybrid junction operation. For instance, the conventional rectangular waveguide (WG) is bulky and hard to be integrated with the printed waveguides. This issue becomes more and more critical at high frequencies in particular at millimeter-wave (mm-wave) band. Furthermore, either the SIW or the microstrip technologies is subjected to high dielectric losses at high frequencies. The previously-mentioned problems make the study of the RGW technology for designing microwave components with better performance is preferred.

In this chapter, a design methodology of a 0dB forward coupler based on the ridge gap waveguide (RGW) technology is presented. The proposed design methodology is based on exact theoretical formulations rather than any approximate or empirical equations. The procedure of this methodology is to build a virtual equivalent waveguide model. The proposed waveguide has two vertical left and right walls are made of perfect magnetic conductors (PMC), while the horizontal upper and lower perfect electric conductor (PEC) walls. A detailed analysis of the proposed hybrid PEC/PMC waveguide is introduced as the starting stage to design the RGW couplers. The equivalent RGW coupler that assures

the same operation of the hybrid PEC/PMC waveguide at a specific frequency range is deduced based on detailed theoretical aspects. Furthermore, a simple analyzing of transitional bends with precise calculations is presented in this chapter, which is an essential building block of several mm-wave components such as the six-port junction and the butler matrix. The possibility of tuning the coupler center frequency is presented without the need for utilizing any nonlinear elements. The resulting RGW couplers are implemented by the well-known full-wave simulator (Ansoft HFSS), with verification through prototype measurements to confirm the validity of the proposed design methodology. A good agreement is achieved between measurement and simulation results.

The design procedure of the proposed RGW-based hybrid junction begins by deriving the field solutions and dispersion equations of the hybrid PEC/PMC waveguide. The obtained dispersion is applied for determining the required coupling length at the operating frequency range. The coupling mechanism, in this design, is based on Riblet (short slot) coupler [74]. The following step is to implement the RGW coupler based on the dimensions obtained from the hybrid PEC/PMC waveguide. A comparison between the results of the hybrid PEC /PMC waveguide coupler and the RGW-based coupler leads to an important observation. This comparison proves that the width of the RGW is not constant with the frequency, which may be considered as an effective width that varies with frequency. In other words, the equivalence between the hybrid PEC/PMC waveguide width and the RGW effective width is a frequency-dependent property. This is described in detail through the chapter.

Recent researches about microwave components based on RGW technology typically depend on approximate, empirical equations, and numerical solutions. For instance, and to the best of our knowledge, there is no reported work in the literature that applies even and odd mode to obtain the coupling length of the forward coupler. Consequently, the long processing time for optimization is required, which led to complicates the design procedure for such microwave components. Hence, it is important to have a clear and simple theoretical design procedure for the RGW-based components. A simple model represents a good approximation of the RGW based on theoretical analysis is presented

in this chapter, which decreases the computational time of full-wave simulators.

3.1.1 Hybrid PEC/PMC Waveguide Operation

The main goal of this part is to develop the concept of an artificial type of waveguides referred to as the hybrid PEC/PMC waveguide. This is to facilitate and simplify the theoretical analysis which would be rather complicated if the RGW is analyzed directly in its complete form. In Fig. 3.1, an equivalent hybrid PEC/PMC waveguide is presented. The operation of the hybrid PEC/PMC waveguide is introduced firstly in this section. Then later, the relation between this hybrid PEC/PMC waveguide and the realistic ridge gap waveguide is explained.

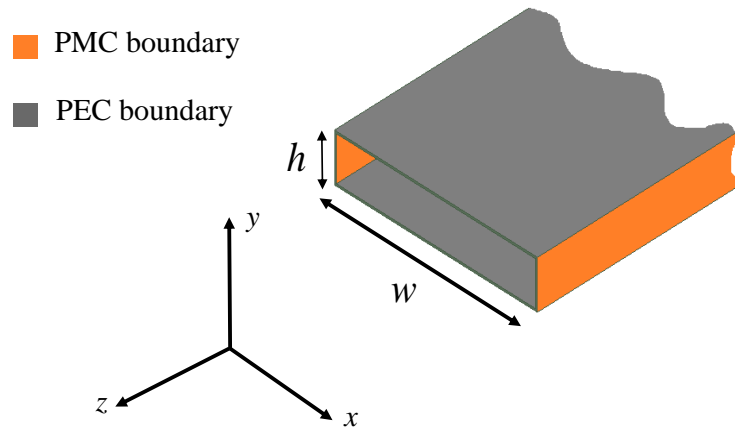


FIGURE 3.1: Equivalent hybrid PEC/PMC waveguide.

The proposed waveguide in Fig.3.1 consists of two vertical PMC walls and two horizontal PEC walls. For simplicity and without loss of principle, the waveguide is assumed to be filled with free space. The width of the waveguide is w , and its height is h . It is assumed that h is always smaller than w in order to avoid the variation of fields in y -direction. Consequently, only the modes that are uniform in the vertical y -direction are the modes of interest in this work.

In order to find full expressions for the field of those modes, one can follow a traditional solution methodology to solve the Heaviside wave equation in rectangular coordinates [4]. Particular boundaries conditions have to be satisfied to solve the wave equation. That is tangential magnetic field has to vanish on the left and right PMC walls, while the tangential electric field has to vanish on the top and bottom PEC walls. The first condition is different from the traditional boundary condition known in conventional rectangular PEC waveguides.

To satisfy this boundary condition at PMC walls, one can write the expression for the tangential electric field component as follows,

$$E_y = \sum_{m=0,2,4}^{\infty} E_m \cos(\beta_{xm}x) e^{-j\beta_{zm}z} + \sum_{m=1,3,5}^{\infty} E_m \sin(\beta_{xm}x) e^{-j\beta_{zm}z} \quad (3.1)$$

where $x = 0$ is taken at the center of the waveguide, β_{zm} is the propagation constant in z -direction and β_{xm} is the propagation constant in x -direction which can be written as,

$$\beta_{xm} = \frac{m\pi}{w}, m = 0, 1, 2, 3, \dots \quad (3.2)$$

The relation between β_{zm} and β_{xm} is given by

$$\beta_{zm}^2 + \beta_{xm}^2 = k_0^2 = \omega^2 \mu_0 \epsilon_0 \quad (3.3)$$

where k_0 is the wavenumber, $\omega = 2\pi f$ is the radial frequency, μ_0 , ϵ_0 are the permeability and permittivity of free space, respectively.

The mode that corresponds to $m = 0$ is the well-known TEM parallel plate mode with propagation only in the z -direction and uniform distribution in the y - and x -directions. This mode has real propagation constant in the z -direction β_{zm} for all frequencies down to direct current DC, regardless of the width w , as illustrated by the solid black curve in Fig.3.2 (a). Moreover, this propagation constant is equal to the wavenumber in free space, k_0 . The electric field E_y of this mode as a function of x is shown by the solid black curve in Fig.3.2 (b).

By assuming that the vertical PMC walls are not artificial and can be truly realized by certain artificial material, we consider the behavior of the first higher-order mode corresponding to $m = 1$ as a plane wave propagating forth and back between the two PMC walls. The reflection coefficient of PMC walls must be in the way that cancels out the tangential magnetic field components and not the electric field components as in the conventional PEC waveguide, i.e., the reflection coefficient magnitude has to be equal to unity.

As a result, the wave will be propagated in the region between those two artificial PMC walls with the tangential electric field taking a maximum value at PMC walls. The propagation constant of this mode in z -direction is purely imaginary below a particular frequency, which is calculated by the distance between the two PMC walls, w . That is,

$$\beta_{z1} = \sqrt{k_0^2 - \left(\frac{\pi}{w}\right)^2} \quad (3.4)$$

From (3.4), one can conclude that β_{z1} is pure imaginary for all frequencies less than $f_{c_PMC/PEC} = c/2w$. The behavior of the real part of β_{z1} is displayed versus frequency by the dashed red curve of Fig.3.2 (a), and the electric field of this mode as a function of x is demonstrated by the dashed red curve in Fig.3.2 (b).

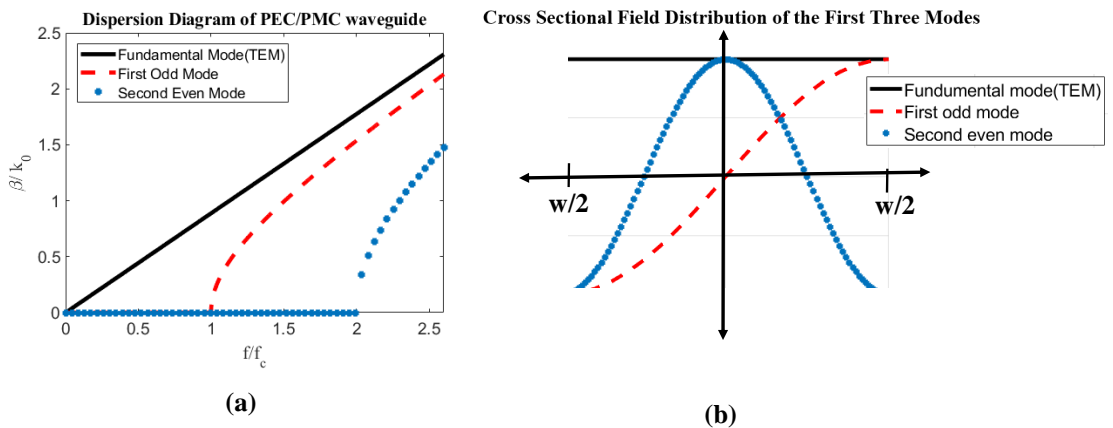


FIGURE 3.2: Hybrid PEC/PMC waveguide: (a) dispersion curves, (b) cross-sectional electric field distribution for the TEM, TE₁₀ and TE₂₀ modes, respectively at $w_r = 13mm$

Although this mode is the first higher order mode and not the fundamental mode, it resembles in behavior the fundamental mode of a traditional PEC waveguide except that the electric field is maximum at the PMC walls and zero at the center, i.e., this mode has an odd symmetry about the longitudinal axis of the guide. The following higher-order mode will be of even symmetry and has a cutoff frequency which is double that of the first higher-order mode, as indicated in Fig.3.2 (b). As a further clarification, suppose $w = 5mm$ and $h = 1mm$. The fundamental propagating mode is the TEM mode with $m = 0$ for all frequencies. The cutoff of the first higher-order mode is $f_{c_PMC/PEC} = c/2w = 30$ GHz. Therefore, at 13 GHz, for instance, the field distribution will be as shown in Fig. 3.3 (a), where the only propagating mode is the uniform parallel-plate mode, while the first higher-order mode still cannot propagate. For the first higher-order mode to propagate, either the frequency of operation should be increased to be higher than 30 GHz or the width w should be increased such that $f_{c_PMC/PEC} = c/2w = 30$ is below 13 GHz. For instance, if $w = 13mm$, the field distribution for the possible two modes at 13 GHz is indicated in Fig. 3.3 (b). These deduced information can be used as the starting phase for designing a factitious forward wave coupler as illustrated in the next section.

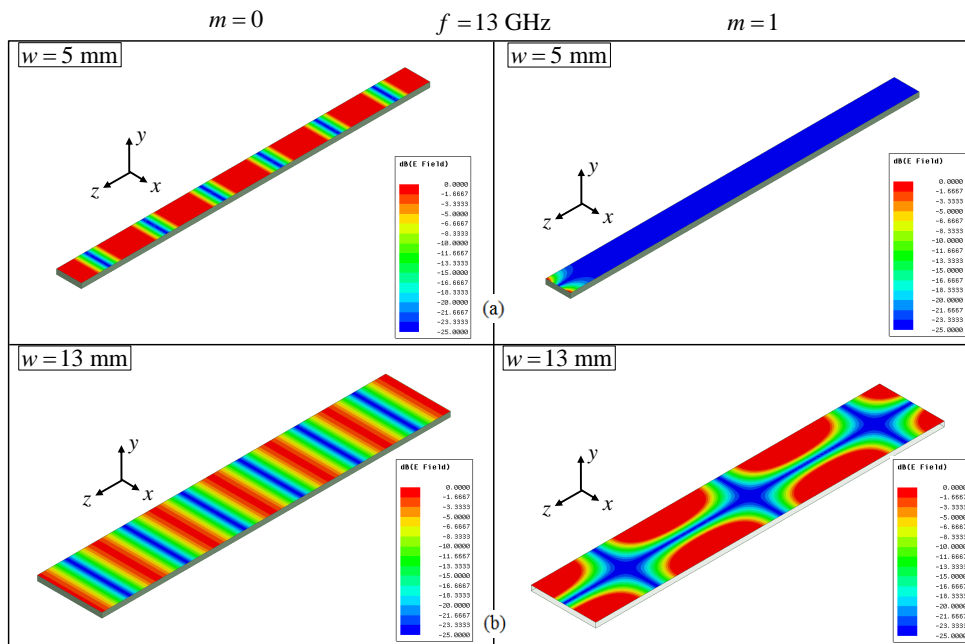


FIGURE 3.3: Field Distribution of the ideal PMC waveguide (a) at width of $w = 5mm$ for $m=0$ and $m=1$ and (b) at $w = 13mm$ for $m=0$ and $m=1$.

3.2 Hybrids PEC/PMC Coupler

Generally, the hybrid coupler is a kind of four ports directional coupler, which can be designed to achieve theoretical coupling levels as high as 0dB. The coupling phenomenon discussed in this part is mainly based on the concept of the Riblet coupler [74]. The Riblet coupler consists of two rectangular waveguides placed parallel to each other. The common wall is the short wall, and this wall is completely opened between the guides for a certain length, hence the name “short-slot” coupler. The main objective of this section is to develop the concept of the factitious type of hybrid coupler based on the Riblet coupler concept. We called this new type “Hybrid PEC/PMC” coupler. The configuration of the hybrid PEC/PMC coupler is illustrated in Fig.3.4 (a), where all the horizontal walls are PECs and vertical “short” walls are PMCs.

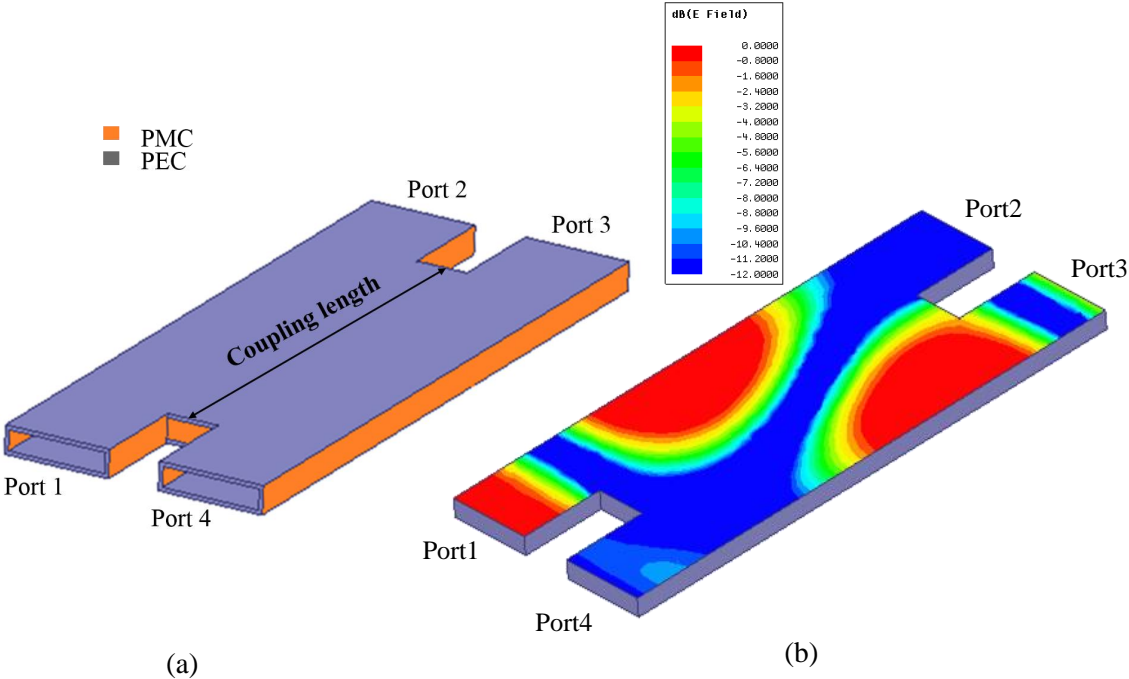


FIGURE 3.4: Hybrid PEC/PMC Coupler, (a) geometry, (b) electric field distribution at 13GHz

The proposed structure consists of two PEC/PMC waveguides parallel to each other. The common wall is the short PMC wall and this wall is opened between the guides for a certain coupling length. The required coupling level is achieved based on this specific

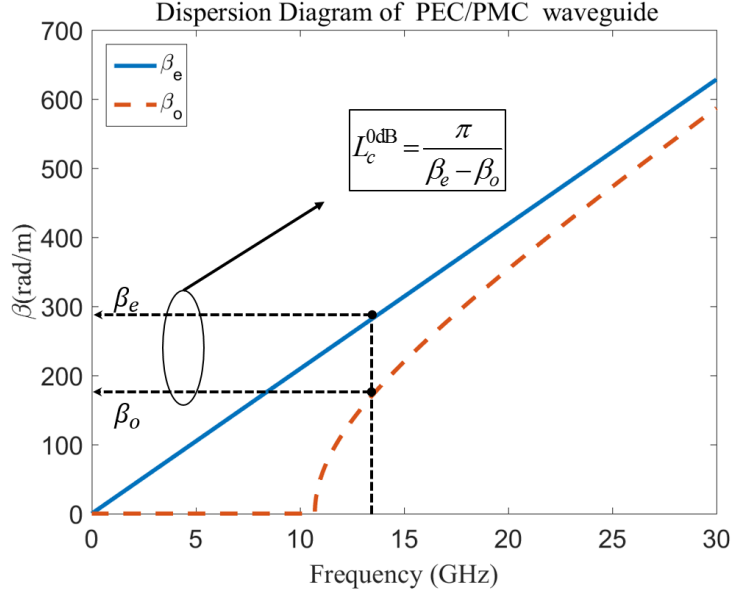


FIGURE 3.5: dispersion diagram of the common section of the hybrid PEC/PMC Coupler.

coupling length, l_c . The coupling length depends on the propagation constants of the even and odd-order modes in the common section between the two waveguides, in which they can be determined from the discussion presented in Sec. 3.1.1. In the ideal case, the power fed to the structure from port 1 is divided between ports 2 and 3 with no reflection at port1 and full isolation at port 4 [75]. The scattering parameters and power division between port 2 and port 3 can be formulated as [75].

$$S_{31} = \frac{e^{-j\beta_e l} - e^{-j\beta_o l}}{2} = -je^{-\frac{j(\beta_e + \beta_o)l}{2}} \sin\left[\left(\frac{\beta_e - \beta_o}{2}\right)l\right] \quad (3.5)$$

$$S_{21} = \frac{e^{-j\beta_e l} + e^{-j\beta_o l}}{2} = e^{-\frac{j(\beta_e + \beta_o)l}{2}} \cos\left[\left(\frac{\beta_e - \beta_o}{2}\right)l\right] \quad (3.6)$$

where S_{31} and S_{21} are the transmission coefficients, β_e is the propagation constant of the first even (dominant) mode in the common section, i.e. $\beta_e = \beta_{z0}$ defined in (3.3) and (3.3) for $m = 0$. Similarly, β_o is the propagation constant of the first odd mode in the common section, i.e. $\beta_e = \beta_{z1}$, defined also in (3.2) and (3.3) for $m = 1$. In (3.5) and

(3.6), l denotes the length of the coupling section. Equations (3.5) and (3.6) show that by obtaining the numerical value of the β_e and β_o , the required coupling length can be easily deduced without the need of empirical equations and optimizations. For example, if the input power should be completely transferred from port 1 to port 3, i.e. a coupling level of 0dB is required, then from (3.5), one can obtain the required coupling length according to,

$$S_{31} = 1 \rightarrow l = l_c = \frac{\pi}{\beta_e - \beta_o} \quad (3.7)$$

The design procedure for the discussed factitious Hybrid PEC/PMC coupler is illustrated in the following example. Suppose the operating frequency is chosen to be 13 GHz. For suitable operation of the coupler, the dimensions of the common section must be selected such that in this common area both the dominant and the first higher order modes are excited. At the same time, the dimensions of the input ports must be selected to guarantee that only the dominant mode is excited and no other mode can propagate.

As discussed in Sec. 3.1.1, the fundamental mode has no cutoff while the cutoff frequency of the first odd mode is $f_{c_PMC/PEC} = c/2w$, and the cutoff of the second higher order even mode is $2f_{c_PMC/PEC}$. Thus, for only the first two modes to exist at the operating frequency, the width of the common section must satisfy

$$\frac{c}{2f_{c_PMC/PEC}} < w < \frac{c}{f_{c_PMC/PEC}} \quad (3.8)$$

At 13 GHz, the width can be chosen to be .

Physically, the width of the input must be less than half of the width of the common part. This should also guarantee that only the dominant mode of each input waveguide can be excited. In this example, we select the width of the input ports to be $w_r = 5mm$. It is very clear from the field distribution in Fig.3.4 (b) that the required design conditions are satisfied at the operating frequency of 13 GHz. The last step is to determine the length of the common section which is the coupling length. To determine the coupling length, one can substitute in (3.2) and (3.3) by $w_r = 13mm$, $m = 0$ to get β_e and by $m = 1$ to

get β_0 at 13 GHz. After that substituting β_e and β_o in (3.7) gives the required coupling length, which is found to be 21 mm. The resultant dispersion curves are shown in Fig.3.5. With the obtained dimensions, full wave simulation gives the field distribution shown in Fig.3.4 (b). The field distribution illustrated confirms the occurrence of full coupling, where all the input power at port 1 is transferred to port 3 at the operating frequency.

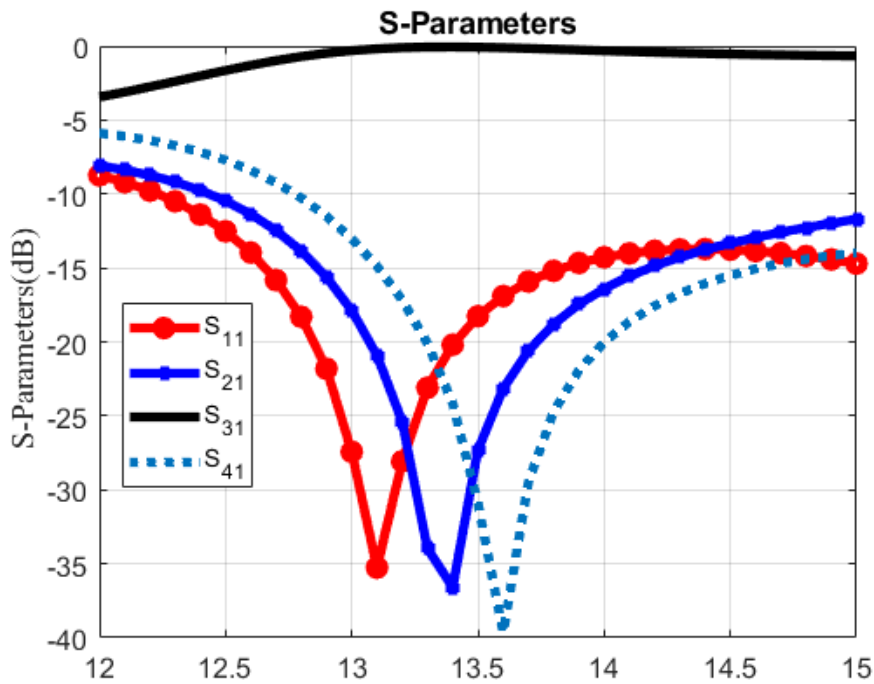


FIGURE 3.6: S-parameters of 0dB hybrid PEC/PMC waveguide coupler.

The simulated magnitude of the S-parameters of the proposed hybrid PEC/PMC waveguide coupler is shown in Fig.3.6 where the coupling level to port 3 is about 0dB from 13 to 15 GHz, the isolation level at port 4 and the through level at port 2 are below -15 dB. Consequently, it could be confirmed that the power is totally transferred from port 1 to port 3 at the center frequency with a bandwidth behaviour governed by the dispersion curves shown in Fig.3.5. Even though the proposed coupler in this section is factitious, this design procedure is found to be very useful to facilitate and simplify the design of realistic forward wave couplers based on modern technologies such as the ridge gap waveguide (RGW) technology. This is illustrated in the rest of this chapter.

3.3 Analytical Design of RGW Coupler

Artificial magnetic conductor (AMC) has been an emerging topic of research over the last few years. AMC is made of periodic metallic structures. The configuration and the periodicity of those structures are designed in such a way that gives a certain required behavior. The behavior of interest in this section is to design vertical guiding walls. The RGW technology is a relatively new type of waveguides realized by the concept of the AMC. In this chapter, RGW is modeled and developed by the factitious hybrid-type of waveguides discussed in Sec. 3.1.1. The main goal in the present section is to show the last step in the design procedure presented in Sec. 3.2. That is the design of realistic forward wave couplers using the RGW technology. The obtained parameters from the hybrid PEC/PMC waveguide model can be utilized directly in the implementation of the region where the wave propagates (values of h and w) in the realistic RGW.

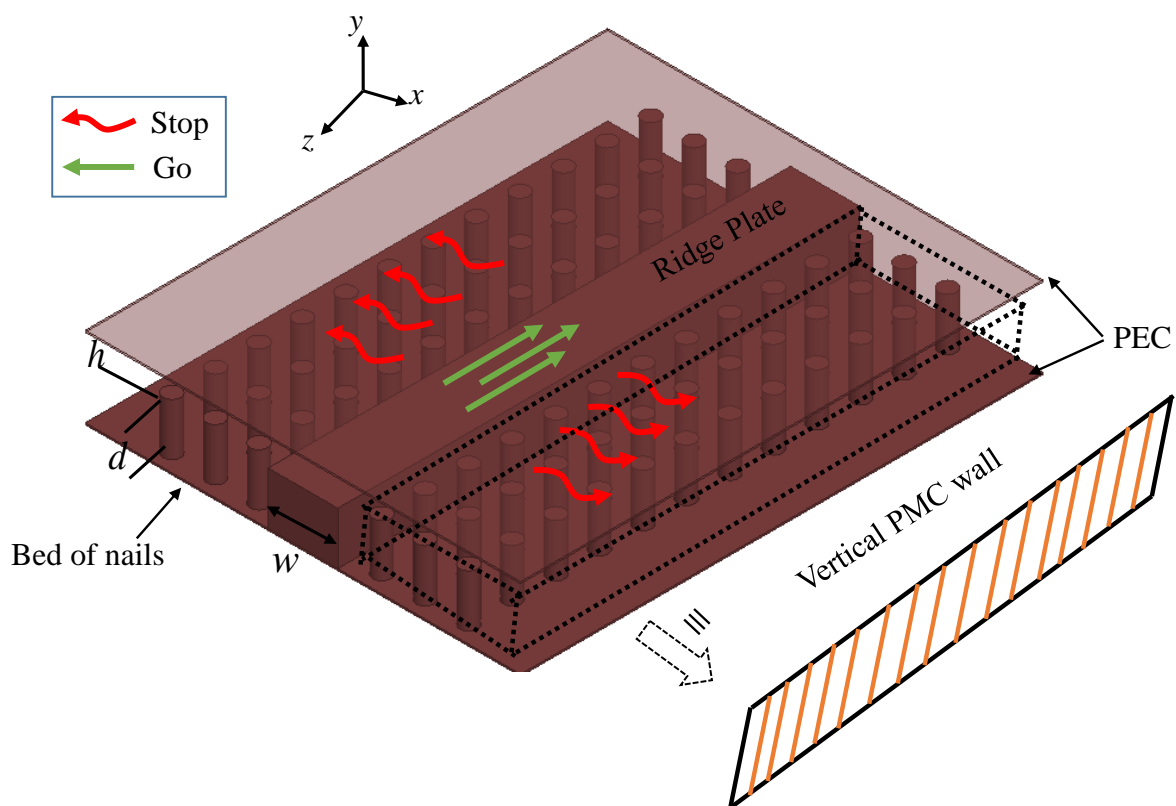


FIGURE 3.7: Complete Ridge Gap Waveguide configuration.

Moreover, the AMC boundaries in the proposed design are realized by periodic perfect conducting cells. As shown in Fig.3.7, the vertical PMC boundaries model the whole dotted region enclosed by the top and bottom PEC plates containing the periodic cells. This is the novelty in this work whereas the dotted region was previously modeled as horizontal PMC boundary. This periodic section is applied to stop the electromagnetic waves from leaking outside the region on top of the ridge within certain stopband. This structure with such boundaries supports a quasi-TEM mode as the fundamental mode. In [18] the analytical solution of the fundamental mode propagating through the RGW has been introduced. In [18], the dispersion diagram was obtained theoretically and verified by using a full-wave eigenmode solver. This part concentrates on summarizing the analytical solution discussed in [18] to obtain the appropriate dimensions of the periodic part in order to act as perfect as the PMC boundary at the required frequency band. In addition to the analytical solution provided in [18], we consider the first two modes not only the fundamental mode. The study of the higher order modes gives the potential of designing the RGW coupler analytically as explained in the following subsections.

3.3.1 Design of Unit Cell and Dispersion Diagram

The dispersion curves of the unit cells is obtained theoretically and then verified by a commercial software (HFSS). The configuration of unit cells is shown in Fig.3.8 (a), where the cells are shaped by metallic cylinders with height d , radius b , and with period a . The height of the nails d should be $\lambda/4$ [18] and the total height between the two horizontal metal plates which is $h + d$ equals $\lambda/2$, where h is the air gap between the bed of nails and the top metal plate, and λ is the free space wavelength. The characteristic impedance of AMC periodic structure depends on the dimensions of the unit cell.

The unit cell dimensions is selected to be the same as the dimensions presented in [18], where the radius of the unit cell $b = 0.5mm$, height of the unit cell $d = 7.5mm$, air gap is $h = 1mm$ and the unit cells period $a = 2mm$. The dispersion diagram with those dimensions of the periodic bed of nails are presented in Fig.3.8 (b) based on (2.3)-(2.5). The

resulting dispersion equations accuracy is confirmed when compared with simulation results obtained from the HFSS eigenmode solver. The dispersion curves in Fig.3.8 (b) gives a clear indication for showing the stop band of the periodic medium, where the dispersion relation is the relationship between the frequency and the propagation constant in z-direction which can be written as,

$$k_z = \sqrt{k^2 - k_y^2} \quad (3.9)$$

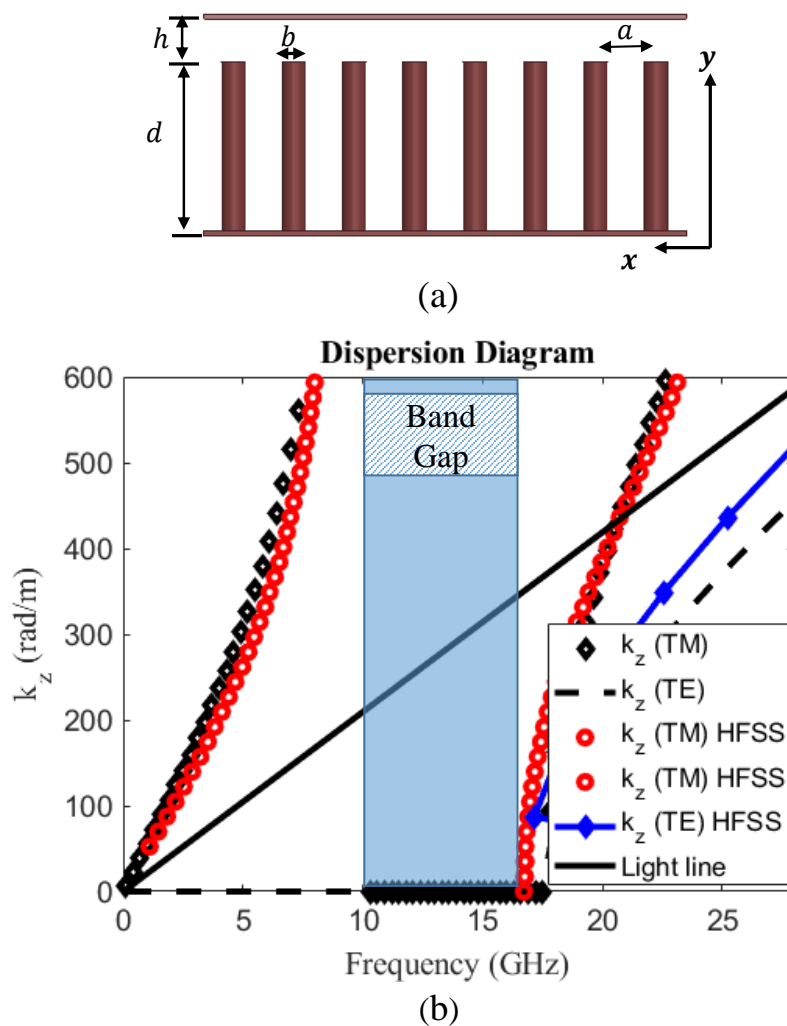


FIGURE 3.8: Periodic bed of nails, (a) geometry and (b) simulated and theoretical dispersion curves of the TE and TM modes.

Fig.3.8.(b) indicates that in the frequency range between 10 and 17GHz, there is no

solution for (2.3) and (2.4) which gives real solution for (2.5). This means there is no propagating waves on the bed of nails within this band of frequencies. In this band, a wave incident from the middle region in Fig.3.7 does not have the possibility of propagating on top of the bed of nails. The phase matching at this boundary ensures that the wave has to be totally reflected. Therefore, by using this bed of nails it is possible to replace the vertical PMC walls by the structure shown in Fig.3.7. Hence, the dispersion equations (2.3)-(2.5) of the bed of nails can be used for designing the operating band of a complete RGW coupler.

3.3.2 Dispersion Diagram of the Complete RGW

In order to form the complete ridge gap waveguide, a metal ridge with width w is placed into the bed of nails as shown in Fig.3.9 (a). Considering the above in Sec. 3.2, the width of the common section can be chosen as $w = 13mm$ in order to guarantee both the dominant (Q-TEM mode) and the first higher-order modes are excited over the bandwidth. Within such structure, Q-TEM mode and the first higher-order mode are propagating along z -direction with phase $e^{-jk_{zm}z}$.

To satisfy the boundary conditions of this design, where the cells act as PMC boundary at both ridge sides, one can write the expression for the electric field component on the ridge as follows,

$$E_y = \sum_{m=0,2,4}^{\infty} E_m \cos(k_{xm}x) e^{-jk_{zm}z} + \sum_{m=1,3,5}^{\infty} E_m \sin(k_{xm}x) e^{-jk_{zm}z} \quad (3.10)$$

where $x = 0$ is taken at the center of the ridgeline. By deriving the remaining field equations and applying the continuity of the fields along the edge of the walls ($x = \pm w/2$), the dispersion curves of the Q-TEM mode and the first higher order mode can be

stated, respectively, as follows [18, 46]:

$$\sqrt{k^2 - k_z^2} \tan \left(\sqrt{k^2 - k_z^2} \frac{w}{2} \right) (k^2 - \tilde{k}_y^2) + \frac{k_z^2 \tilde{k}_y^2 - k^2 \sqrt{k_z^2 - k^2 + \tilde{k}_y^2} \sqrt{k_z^2 - k^2 + \tilde{k}_y^2}}{\sqrt{k_z^2 - k^2 + \tilde{k}_y^2}} = 0 \quad (3.11)$$

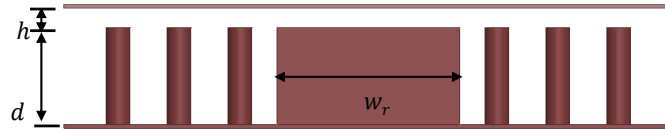
$$\sqrt{k^2 - k_z^2} \cot \left(\sqrt{k^2 - k_z^2} \frac{w}{2} \right) (k^2 - \tilde{k}_y^2) - \frac{k_z^2 \tilde{k}_y^2 - k^2 \sqrt{k_z^2 - k^2 + \tilde{k}_y^2} \sqrt{k_z^2 - k^2 + \tilde{k}_y^2}}{\sqrt{k_z^2 - k^2 + \tilde{k}_y^2}} = 0 \quad (3.12)$$

where $\tilde{k}_y = k_y$ for *TE* solution in (2.3), $\tilde{k}_y = k_y$ for *TM* solution in (2.4),

A Matlab code is employed to solve the above transcendental equations, from which the dispersion diagram of the Q-TEM mode and the first higher-order mode are obtained and shown in Fig.3.9 (b). From this figure, it is clear that there are only two modes propagating within the 10 to 17 GHz band. Those modes are the Q-TEM mode and the first higher order mode. The other modes that appear on both sides of the band gap are due to the truncated of the periodicity in the direction normal to the propagation direction. Fig.3.9 (b) shows there is a good agreement between the analytical solution and the full-wave solution.

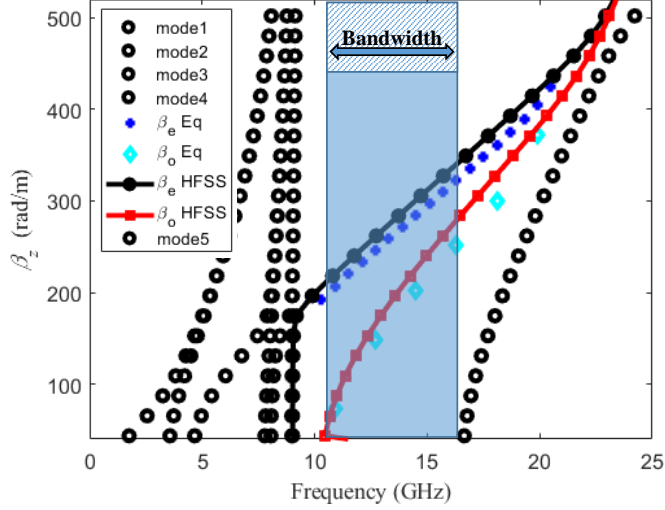
To validate the relationship between the Hybrid PEC/PMC waveguide and the real waveguide realized by the bed of nails, the result of Fig.3.5 is compared to those of Fig.3.9 (b) and shown in Fig.3.10. From the comparison in Fig.3.10, it can be depicted that the cut-off frequency of the higher-order mode relies on the width of the ridge. Also, it can be observed that there is an agreement in the behavior among the simulated, theoretical results and the hybrid PEC/PMC waveguide model. However, there is a slight variance in the cut off frequency of the odd mode of the RGW and the hybrid PEC/PMC waveguide model.

This observation reveals important information about how to utilize the design rules shown in Sec. 3.2 for RGW coupler without causing any shift in the coupler bandwidth. The interpretation of this deviation is that the electrical width of any RGW is slightly



(a)

Theoretical,PMC/PEC and simulated Dispersion Diagram at $w_r=13mm$



(b)

FIGURE 3.9: Comparison between dispersion curves of RGW obtained from HFSS and theoretically, at $w = 13mm$

Theoretical,PMC/PEC and simulated Dispersion Diagram at $w_r=13mm$

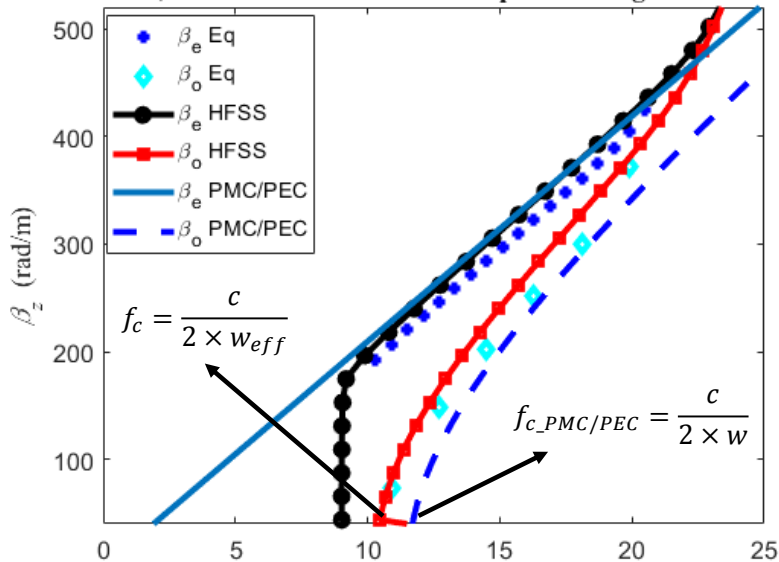


FIGURE 3.10: Dispersion curves for the common waveguide of RGW coupler obtained from, hybrid PEC/PMC theoretical model (solid lines), theoretical analysis of RGW coupler (circles and diamonds) and simulation results of RGW coupler (dashed lines) where $w = 13mm$.

different from PEC/PMC waveguide. Therefore, it is extremely important to find the relation between the effective width of the RGW and the hybrid PEC/PMC waveguide width. The effective width of this structure can be determined from the cutoff frequency obtained from the dispersion diagram where,

$$w_{eff} = \frac{c}{2f_c} \approx 1.1 \times w \quad (3.13)$$

The cut-off frequency of the odd mode is 10.57 GHz as shown in Fig.3.10, therefore its effective width w_{eff} is 14.2 mm which is about 10% wider than the actual width of the ridgeline. By using the effective width as the width of the hybrid PEC/PMC waveguide, the obtained dispersion diagram will be exactly the dispersion diagram required for designing the RGW coupler.

As a validation for the previously-mentioned concept, the dispersion diagram of the hybrid PEC/PMC waveguide coupler and the RGW coupler that has a width equal to the calculated effective width of the RGW are shown in Fig.3.11. From this figure, it is very clear that there is an agreement between simulation and theoretical results. This means that the width of any RGW is not the physical width, but it is an effective width that must be obtained from its dispersion. Thus, the required coupling length based on the obtained effective width is demonstrated in Fig.3.12 (b) based on the PEC/PMC waveguide dispersion of Fig.3.2 (a) or Fig.3.5.

As a conclusion, the design of any RGW-based microwave component is related to the effective width of the RGW not the actual width dimension. The relation in (3.13) is, of course, specific to this example. However, it is not expected to deviate much in other examples. Therefore, it is the task of the designer to recheck the performance of the final product if the dimensions are initially selected based on (3.13).

3.3.3 Excitation Based on PEC/PMC Circular Bend

Physically, it is impracticable to design two ports beside each other as in the hybrid PEC/PMC waveguide. Sufficient space must be kept for at least one or two rows of

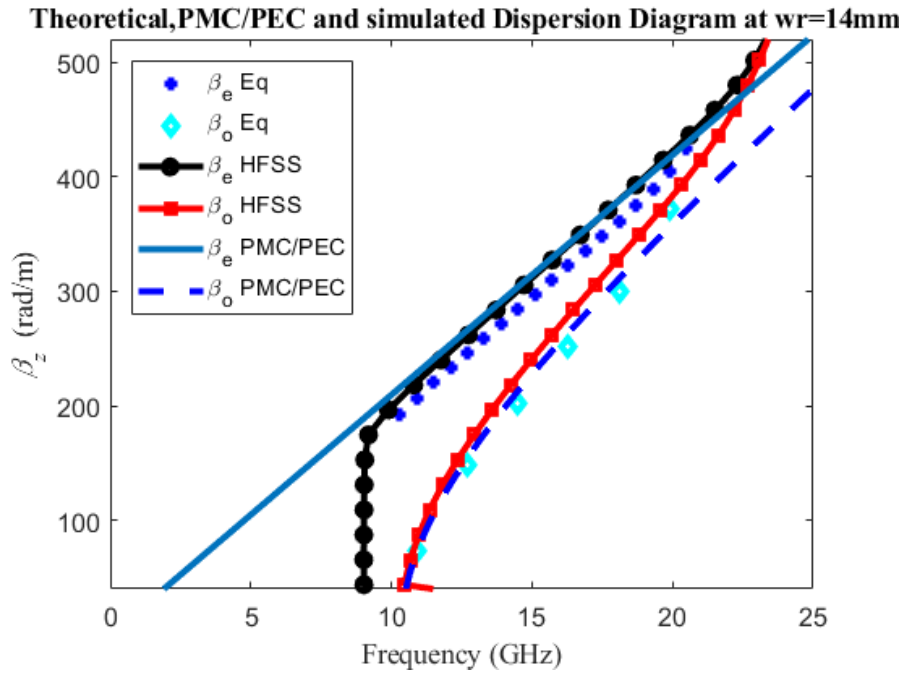


FIGURE 3.11: Dispersion curves of the RGW coupler and the hybrid PEC/PMC waveguide with width equal to the effective width.

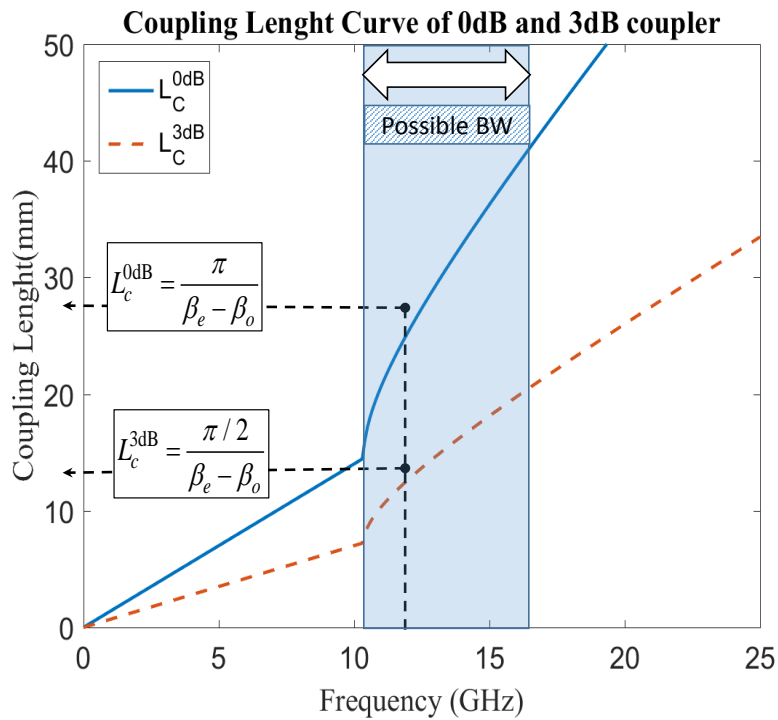


FIGURE 3.12: Coupling length versus frequency for both of a 0dB and a 3dB couplers.

pins to operate as a PMC. For that reason, it is chosen to deliver the signal through circular bends. The phase and amplitude responses of a circulating RGW is determined analytically in this section. The presented phase shift by circulating RGW has not been previously studied in details. In several applications, the phase shifter is considered as a critical element especially in beamforming networks. As usual, a phase shift is designed in bent shapes rather than in straight lines. Therefore, it is important to study the phase response in such a curve-shaped RGW. The hybrid PEC/PMC waveguide is applied to determine the phase response of circulating bends at the output and input ports of the RGW coupler. This is to simplify and facilitate the theoretical analysis which would be rather difficult if the RGW is analyzed directly in its complete form.

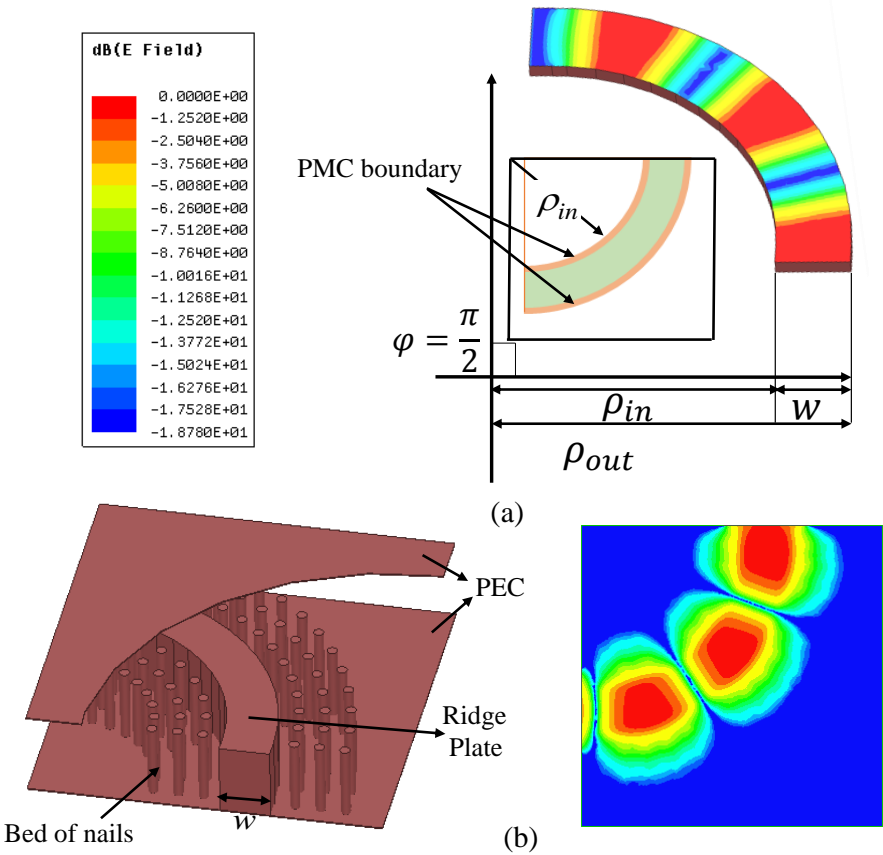


FIGURE 3.13: Circulating hybrid PEC/PMC and Realistic waveguide bends with the corresponding field distributions”

A circulating bend hybrid PEC/PMC waveguide equivalent to the curved RGW is shown in Fig.3.13. A simple theoretical design procedure for designing the circulating

bend hybrid PEC/PMC waveguide is introduced in this section. Also, the relation between this hybrid PEC/PMC waveguide and the realistic ridge gap circulating bend waveguide is explained. The suggested geometry of the output and the input ports is a circulating waveguide bend with cross section $w + h$, inner radius ρ_{in} and outer radius $\rho_{out} = \rho_{in} + w$. The same problem was introduced earlier for the traditional metallic rectangular waveguide [76]. Consequently, by using the same concept and changing the boundaries condition according to the proposed design, the resultant operation can be deduced. The wave function in circular bend waveguide can be written as [76]:

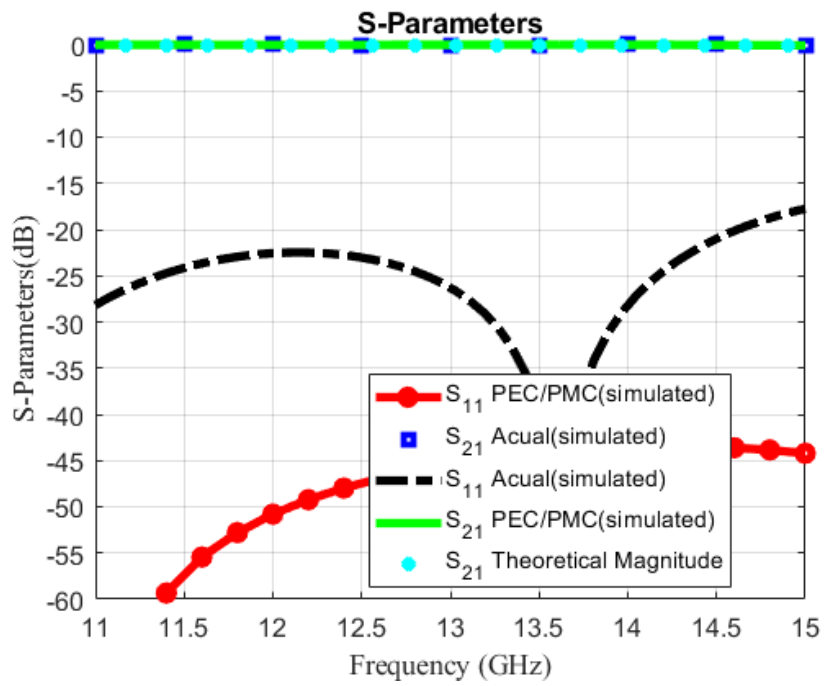
$$\psi = [AJ_n(k\rho) + BN_n(k\rho)]exp(-jn\varphi) \quad (3.14)$$

where $J_n(k\rho)$ is the Bessel function of the first kind of order n , $N_n(k\rho)$ is the Bessel function of the second kind of order n , and ρ, φ are the cylindrical coordinates and A is an arbitrary constant. The constant n represents the propagation constant in φ - direction. This is the unknown which needs to be calculated. The wave function ψ , in (3.14) is utilized to obtain the complete expressions for the electric and magnetic fields. However, this can be done for two types of possible solutions, namely the TE^z and TM^z . The boundary conditions in this problem at hand dictate that the solution of interest is the TM^z . The general solution for TM^z modes must satisfy [76]:

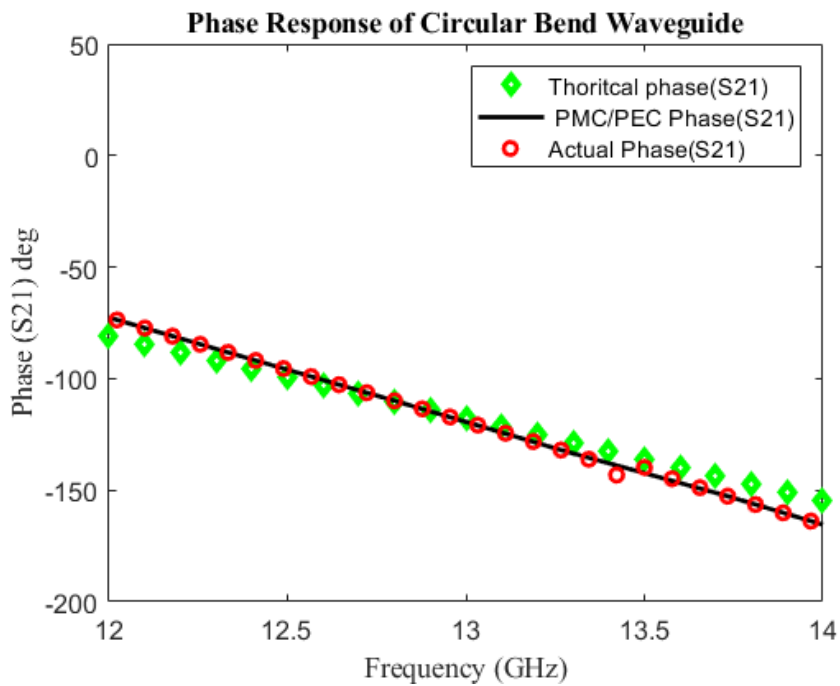
$$J'_n(k_\rho\rho_{in})N'_n(k_\rho\rho_{out}) - J'_n(k_\rho\rho_{out})N'_n(k_\rho\rho_{in}) = 0 \quad (3.15)$$

where $k_\rho = k$. Equation 3.15 is solved numerically for the unknown, n . For instance, suppose the circulating waveguide designed in Section 3.2 to be of inner radius $\rho_{in} = 17mm$, outer radius $\rho_{out} = 22mm$, and $\varphi = \pi/2$ as displayed in Fig.3.13. This radius is selected to minimize the reflections and maximize the transmission through the bend.

A Comparison among the hybrid simulated PEC/PMC waveguide bend, theoretical analysis, and the simulated realistic waveguide bend is shown in Fig.3.14. The phase and magnitude responses are displayed in Fig.3.14 (a) and (b), respectively. The phase response of such waveguide is more significant than the magnitude response, which is



(a)



(b)

FIGURE 3.14: Comparison among the theoretical, Realistic and hybrid PEC/PMC phase and magnitude response of circular bend waveguide: (a) Magnitude response, (b) phase response.

critical if the coupler is to be included in beamforming networks such as Butler matrix. From Fig.3.14 (a) and (b), it is clear that there is an agreement in the behavior of magnitude and phase responses among the theoretical, realistic simulated results and the hybrid PEC/PMC waveguide model from 12.5-13.5 GHz. However, there is a slight variance in the phase at frequencies far from the center frequency. The explanation of this deviation is that the bed of nails loses its perfect periodicity in the bent waveguide. The bed of nails surrounding the ridge act as PMC just around the 13GHz.

3.3.4 The Full RGW Coupler

In this subsection, the vertical PMC boundaries are replaced by the periodic unit cells. The dimensions of the unit cell are the same as presented in Sec. 3.3.1 to work over an approximate bandwidth of (10-17) GHz. The configuration of a 0dB RGW coupler with the designed input and output ports is shown in Fig.3.15. The coupling length is obtained from the graph shown in Fig.3.12 and (3.6) based on what is obtained from the hybrid PEC/PMC waveguide coupler. By using the obtained effective width, the required coupling length becomes 29 mm. For a physical connection to the input and output ports, they are designed based on circulating bends as explained in Sec. 3.3.3.

The field distribution and the scattering parameters of the designed RGW coupler are displayed in Fig.3.16 (a) and 3.16 (b), respectively. From the figures, it can be noted that the proposed design procedure resulted in an excellent operation of the RGW coupler exactly at the selected design frequency where full coupling occurs.

3.3.5 Frequency-Tunable RGW Coupler

One of the most valuable features that may exist in a microwave component is the tuning capability. The tunability of the RGW is not widely reported in the literature. For instance, in [77], an electrically-tunable planar groove gap waveguide resonant cavity is presented. A combline low-loss tunable resonator based on a SIW cavity loaded with

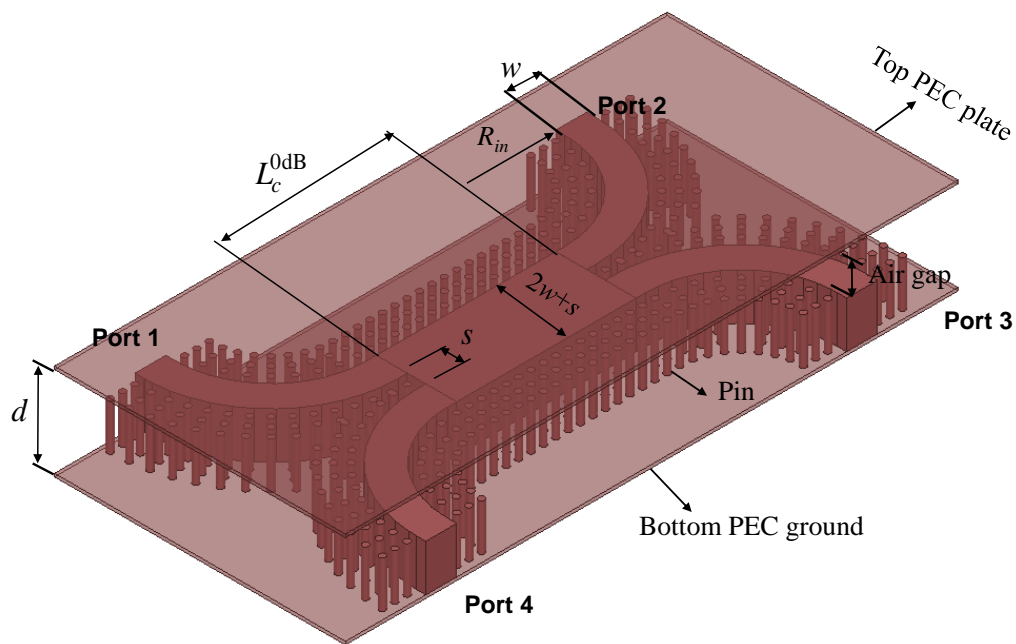


FIGURE 3.15: The physical structure of the RGW 0dB coupler.

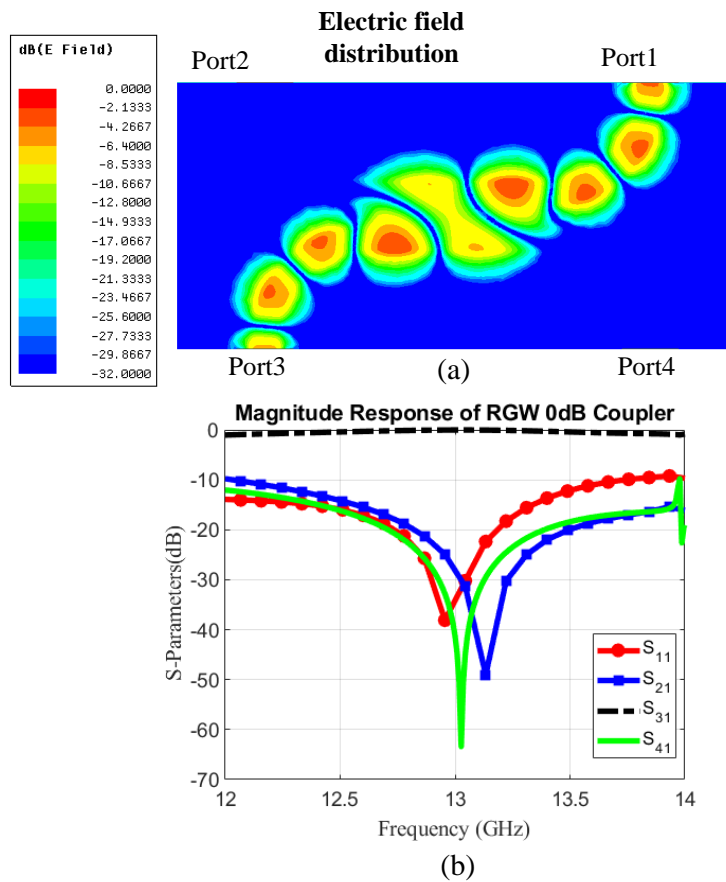


FIGURE 3.16: Full wave simulation for the 0dB RGW coupler at 13 GHz, (a) electric field distribution and (b) magnitude of S-parameters.

varactor tuning diodes is presented in [78]. In the referred examples, the tunability is achieved by applying a nonlinear varactor element.

In this section, it is noted that the frequency tuning could be obtained easily without the need for employing nonlinear elements. This could be achieved by just slightly moving the top conducting plate of the RGW which controls the height h of the RGW. The result of changing the height h is presented in Fig.3.17. It could be noticed from this figure that the propagation constant of the first higher-order mode (odd mode) has different values for different heights at every single frequency. The difference in the propagation constant reaches to $45.7\text{rad}/\text{m}$ with only 2.5 mm change in the height.

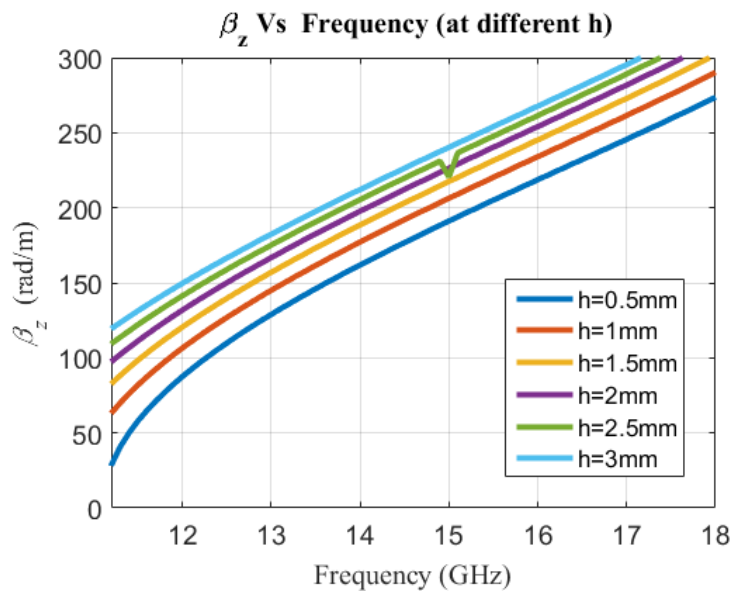


FIGURE 3.17: The behavior of odd mode versus the air gap height.

On the other hand, the propagation constant of the Q-TEM mode (even mode) is almost independent on the height. Therefore, the coupling length obtained from equation (3.6) may have different values for different heights as shown in Fig.3.18. This means that controlling the height of the upper conducting plate may tune the coupler center frequency as shown in Fig.3.19. The tunability mechanism is feasible, especially the upper conducting plate of the RGW is not attached to the lower plate.

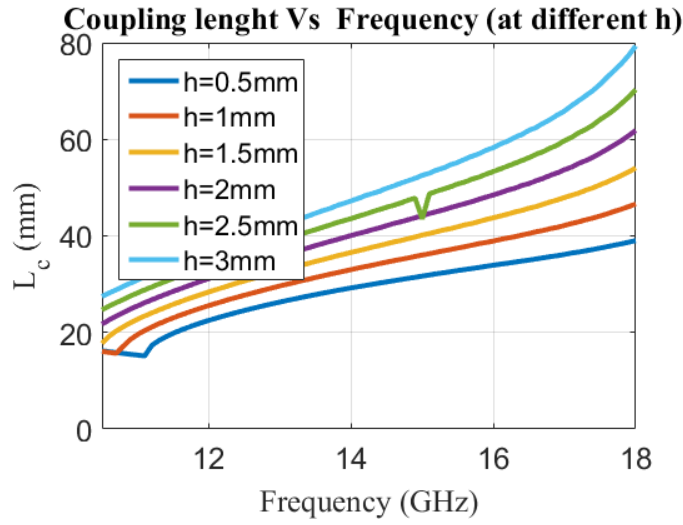


FIGURE 3.18: The coupling length versus the air gap height.

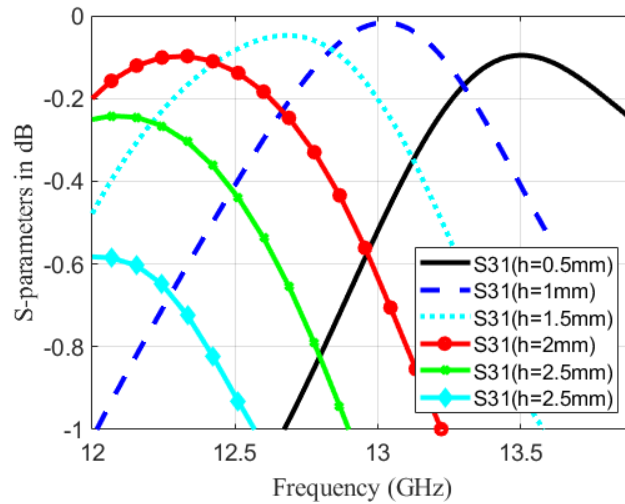


FIGURE 3.19: Full wave simulation for the 0dB RGW coupler at 13 GHz: magnitude S-parameters (S_{31} and S_{21}) versus the air gap height.

3.4 A Possible Setup for Prototyping the Proposed RGW Coupler

3.4.1 Microstrip to RGW Transition

To physically excite and measure the performance of the proposed structure by a Vector Network Analyzer (VNA), a microstrip transition to RGW is needed at all input and output ports. This transition should cover the entire bandwidth of our design with better

than 15 dB in back to back configuration. Different models of transition are presented in [79–81].as shown in Fig.3.20 the dominant mode in microstrip and RGW is Q-TEM mode, which is easy to design transition from microstrip to RGW. Based on previous references, a transition from microstrip waveguide to metallic RGW is designed and tested with the whole 0dB coupler structure. The microstrip transition is displayed in Fig.3.21. The proposed design is very simple, which the transition of microstrip is printed over Ro-3006 dielectric substrate with $\epsilon_r = 6.15$. In this transition, the microstrip line is located on the ridgeline of the RGW. Consequently, the microstrip mode will transform gradually to the air-filled ridge gap waveguide mode. Due to the standers of the substrate height of the microstrip line, the size of the air gap should be adjusted gradually to be identical to the substrate height. The changing of air gap size is realized by tapering the height of the matching section. Two microstrip transitions to RGW are used in a back-to-back design is illustrated in Fig.3.21. The result of the back-to-back transition is shown in Fig.3.22. It can be observed that the S11 is below -20 dB from 12.5 to 14.5 GHz, and S21 is about 0.2 dB.

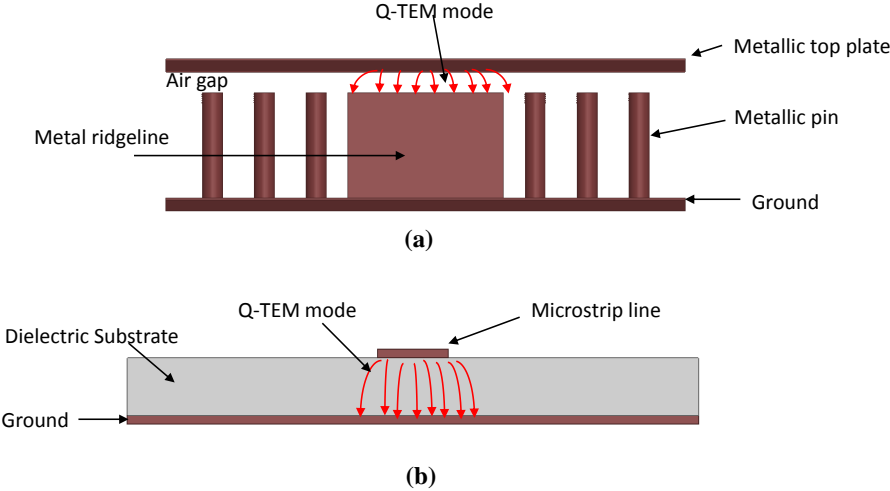


FIGURE 3.20: The fundamental mode in Microstrip and metallic ridge gap waveguide.

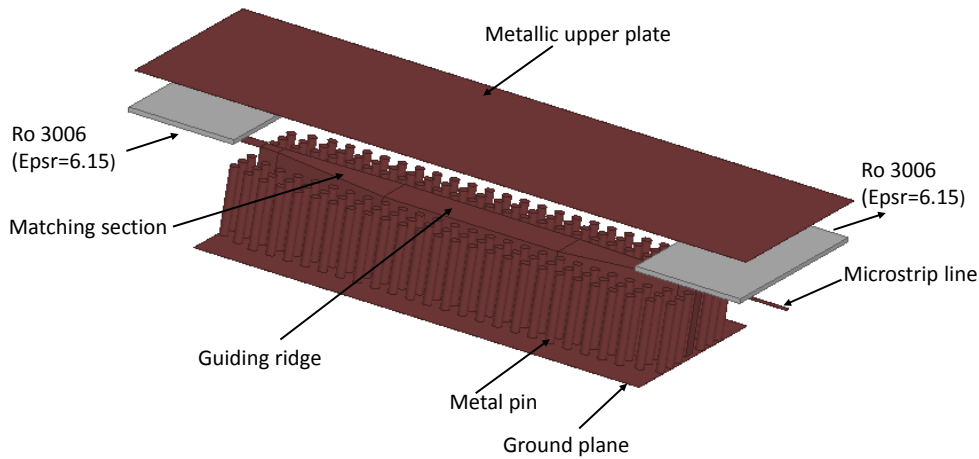


FIGURE 3.21: Microstrip to metallic Ridge gap waveguide transition.

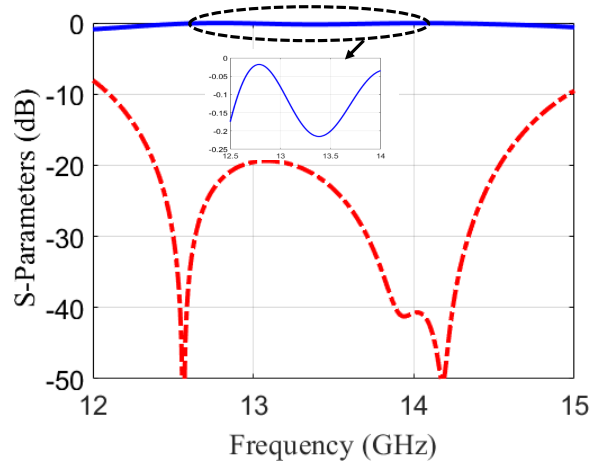


FIGURE 3.22: Simulated results microstrip to metallic ridge gap waveguide transition.

3.4.2 Whole Setup Model of 0dB Coupler Include the Microstrip Transition

The complete structure of the 0dB coupler with the designed transitions is solved numerically before the fabrication stage. Fig.3.23 shows the whole model setup of the 0dB coupler, where the top metal plate is displaced to up to show the internal details of the structure. The scattering parameters and field distribution of the designed RGW coupler are shown in Fig.3.24 (a) and (b), respectively. From this figure, it can be concluded that the proposed design procedure resulted in an excellent operation of the RGW coupler. Where a full coupling occurs specifically at the chosen design frequency.

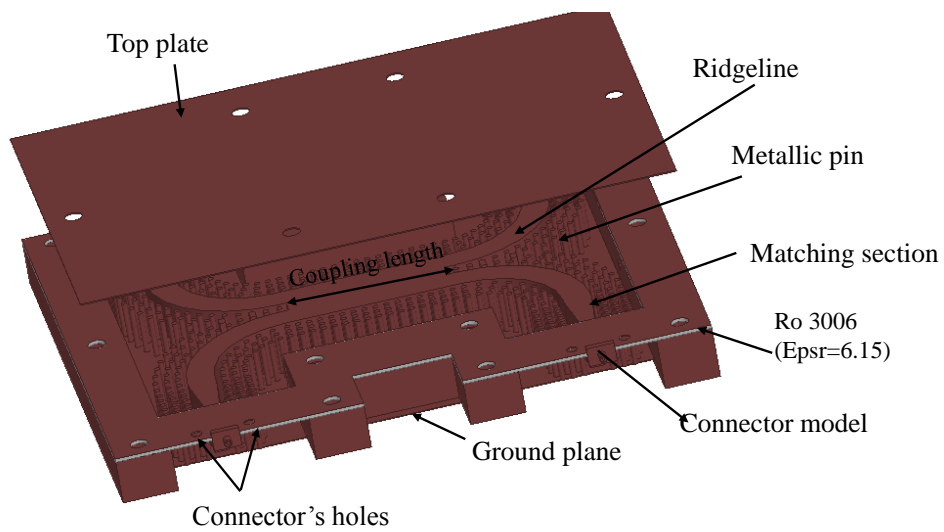


FIGURE 3.23: The whole setup model of 0dB coupler include the microstrip transition.

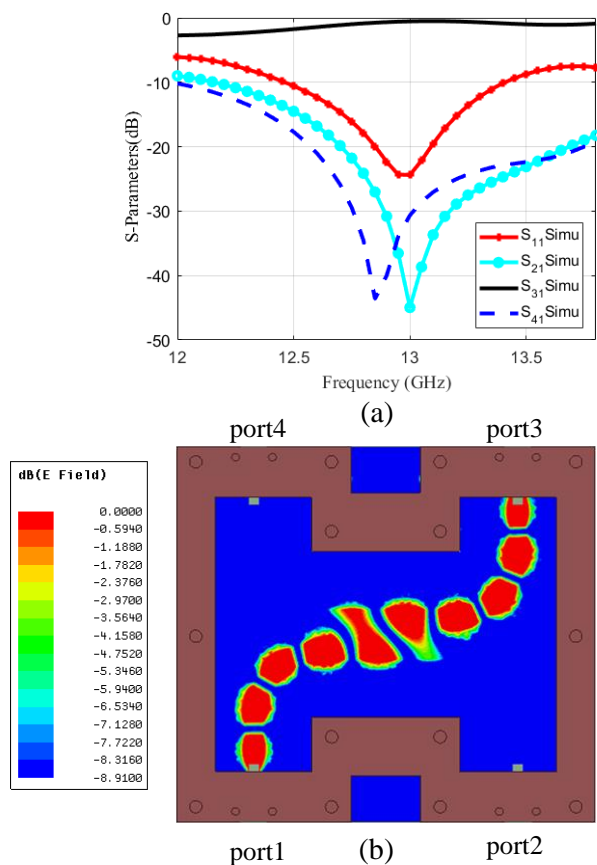


FIGURE 3.24: Simulated scattering parameters and Electric field distribution of the whole setup model of 0dB coupler include the microstrip transition. (a) Scattering parameters, (b) Electric field distribution.

3.4.3 Fabrication and Experimental Results

In order to verify the proposed structure, a prototype of the 0dB coupler is fabricated and measured, as shown in Fig.3.25. The main body of the 0dB coupler and the microstrip transition are built separately. After that, all parts are assembled by bolts. We use plastic 3D printing technology to build the main body of the structure of the 0dB coupler. The 3D printer uses an opaque white SLA plastic that acts similarly to polycarbonate and has elevated heat resistant. Then, the printed structure is electroplated with 0.02 mm thick copper material. Also, the PCB technology is used to fabricate the microstrip transition and the top plate. Fig.3.25 (a) and (b) show the individual parts and the assembled 0dB coupler with the connectors respectively.

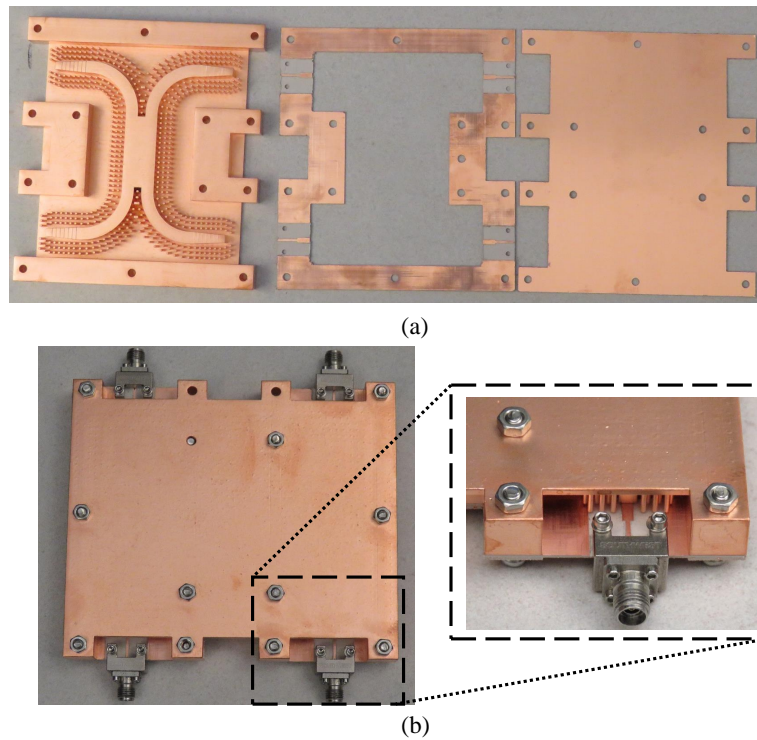


FIGURE 3.25: Pictures of the fabricated individual parts and assembled structure. (a) Individual parts of designed 0dB coupler, (b) Assembled 0dB coupler.

The simulated and measured S parameters of the proposed design are shown in Fig.3.26. From this figure, it can be observed that the measured and simulated results in good agreement. The designed coupler works perfectly at the chosen design frequency where

full coupling occurs at 13 GHz. Furthermore, the measured isolation better than 20dB over the whole band. The insertion loss in setups is around 0.7 dB, due to the fabrication tolerance and connectors. However, this affects the configuration dimensions, which can lead to a small shift and losses in the measurement results. Also, since the design is plated with copper, it can be oxidized over time. Therefore, it might increase the losses.

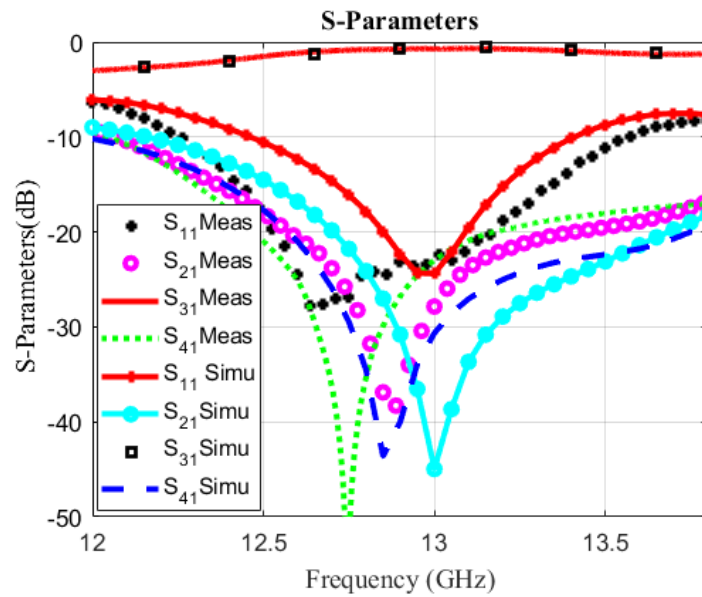


FIGURE 3.26: Measured and simulated scattering parameters of the whole setup model of 0dB coupler include the microstrip transition.

A design methodology is presented for a hybrid junction based on RGW technology In this chapter. This methodology relies on the operation of a hybrid PEC/PMC waveguide. the proposed waveguide shows great potential for an accurate estimation for the required dimensions of the RGW coupler to operate at a particular frequency band. It has been concluded from that model that an RGW acts with an effective width that requires to be determined precisely. The phase response analysis of a circulating RGW bend is introduced. The possibility of tuning the center frequency of an RGW coupler is introduced by moving the upper conducting plate of the RGW. The measurement and simulation results of the whole model setup of the 0dB coupler are compared to each other. The results display acceptable levels compared to each other's and shown that the 0dB coupler works effectively with calculated coupling length from the proposed PEC/PMC model.

Chapter 4

Odd Mode RGW-based Devices: Design

Procedure

4.1 Introduction

The main requirements in the components and antennas design are a low loss, a high gain antenna, and compact size, which are highly recommended to compensate various losses that conventional waveguides are suffered [82–84]. The antenna array is commonly used to achieve high gain, in which a complex feeding network is needed to excite each radiator element. However, the feeding network causes extra losses in addition to the conventional waveguide losses. Therefore, the mentioned issues must be considered to implement any wireless system.

Recently, substrate integrated waveguide (SIW) high order mode becomes more attractive to design antenna and network antenna. Based on the properties of high order mode, the antenna feeding can be implemented with a more compact size and low losses.

Several higher-order-mode (SIW) designed were implemented for high performance, cost reduction, and simple manufacture at mm-wave band [85–87]. In [88], A single-fed slotted cavity SIW antenna using high-order modes is introduced, which offers a wideband and high gain with low-cost. For mm-wave polarization changeable applications, a microstrip patch antenna based on SIW technology using high-order-mode is presented in [89]. Using high order mode SIW cavity, high-gain dual-polarization and dual-frequency high-gain cavity slot antennas are presented in [90,91]. Generally, most of

the works that based on high order mode are designed using substrate integrated waveguide (SIW) technology, which are suffering from the dielectric loss.

The ridge gap waveguide (RGW) has many advantages rather than conventional waveguides, which is low loss and integrated with planar circuits. Therefore, by using high order mode RGW, it is possible to gather between the aforementioned advantages of using high order mode and overcoming the dielectric loss.

The employment of ridge gap waveguide (RGW) higher-order modes can considerably to design several effective components and antennas at the millimeter-wave band, which led to reduce the number of metal pins and therefore simplify the component configuration. As the hybrid couplers, Y-junction power divider and antennas are a necessary for any wireless system, various components and antennas are designed based on high order mode RGW in this thesis.

4.2 First High Order Mode Ridge Gap Waveguide

In this chapter, two methods to excite the first higher order mode of the ridge gap waveguide (RGW) is presented. The fundamental mode of the RGW is well studied in a lot of papers while the higher order modes are ignored. However, they have some good properties that make them suitable for specific applications. First high order mode of ridge gap waveguide can be used in many applications, but this fact enormously depends on the performance of the transition that use to excite the first high order mode and the components that are suitable to use with RGW. The chosen frequency band, in this thesis, objective to design components and antennas works in Ka-band. The ka band is exploited for a diversity of applications such; police radar, satellite, and many different millimeter-wave applications [92, 93]. Because of that, it is needed a transition works at the specific frequency with a small size, acceptable bandwidth, low losses, and simple configuration. In this chapter, a two method to excite the first higher order mode of the ridge gap waveguide (RGW) is introduced.

4.2.1 Ridge Gap Waveguide Analysis and Unit Cell

The dimensions of the unit cell chosen to work between 25GHz and 40GHz. The unit cell structure is shown in Fig 4.1 (a), where the cell is formed by metallic cylinder with height $d = 2.3mm$, radius $b = 0.5mm$, period $a = 2.5mm$, and air gap height $h = 1mm$. The dispersion diagram of the unit cells is obtained by using commercial software (HFSS). The dispersion curves of the unit cell, shown in Fig 4.1 (b), is obtained based on assuming that the propagation is in the z -direction. It is very clear from the dispersion diagram in Fig 4.1 (b) that there is a bandgap from 22 GHz to 50 GHz.

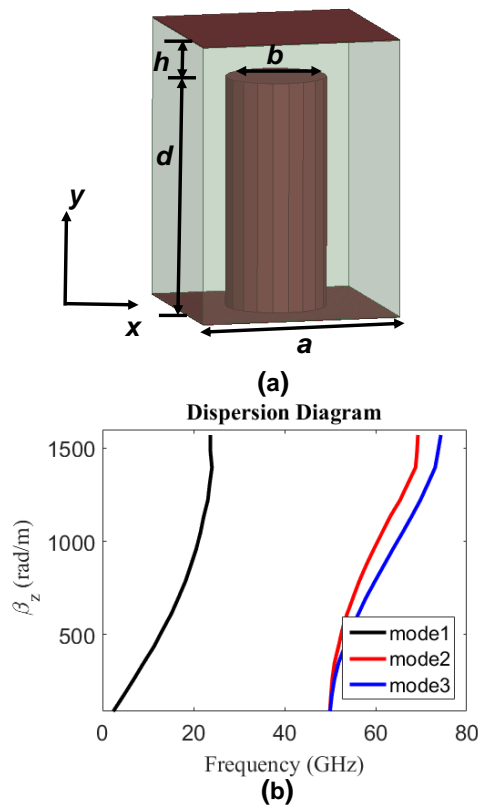


FIGURE 4.1: The configuration of unit cell and its dispersion diagram. (a) The configuration of the unit cell. (b) Dispersion diagram.

4.2.2 Ridge Gap Waveguide Section

To design the complete RGW, a metal ridgeline with width w is inserted into the bed of nails as shown in Fig 4.2 (a). The ridgeline width is selected to be $w = 7.5mm$ in order to ensure the excitation of the dominant (Q-TEM) and the higher-order modes (TE_{m0})

over the operating bandwidth. Using the Eigenmode solver in high frequency structure simulator (HFSS), the dispersion diagram of the RGW can be obtained as shown in Fig 4.2 (b). The RGW consists of a ridgeline surrounded by three bandgap unit cells from each side (Fig 4.2 (a)). Periodic (slave and master) boundary condition is applied along the z -axis, while a periodic or PMC boundary conditions are used in the $y - z$ planes at both ends of the RGW section. The perfect electric boundary condition is utilized to the top and bottom of the RGW section ($x - z$ planes). In the region of bandgap (from 25 to 43 GHz), there are three propagating modes along the ridge : (1) the Q-TEM mode, and (2) the first odd mode TE_{10}^{RGW} , and (3) the second even mode TE_{20}^{RGW} . The other modes that appear on both sides of the bandgap region are out of our scope.

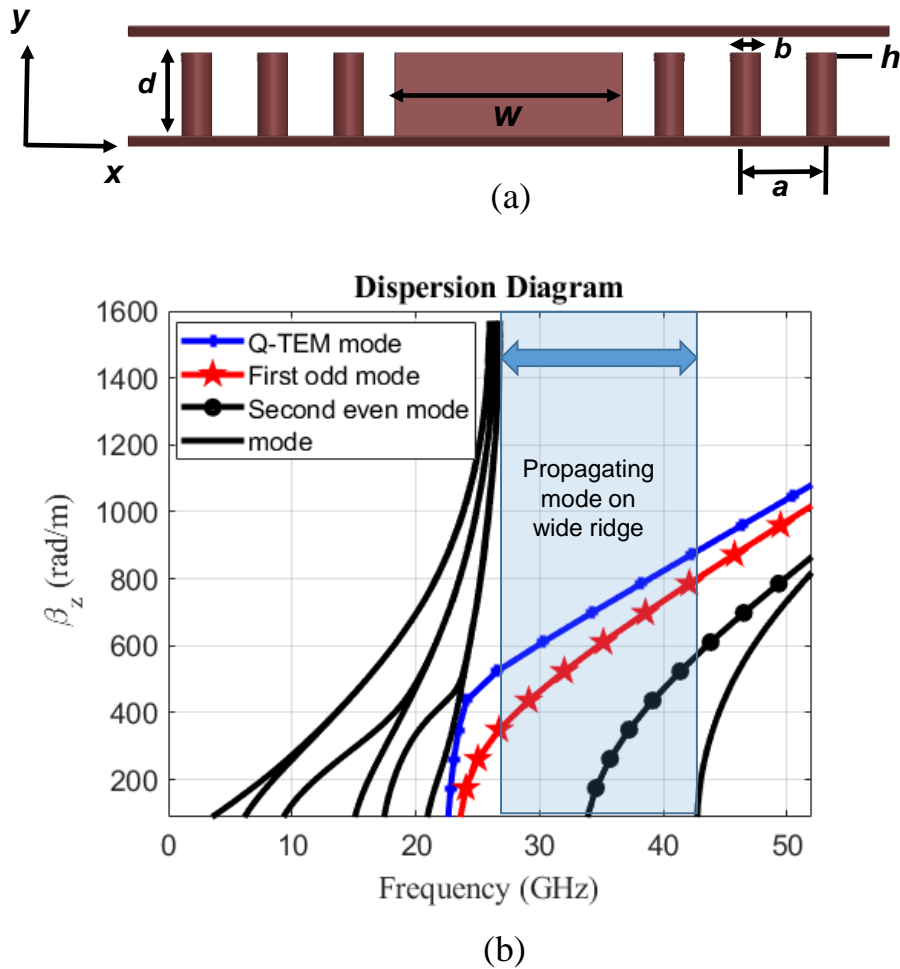


FIGURE 4.2: The configuration of wide RGW and dispersion curves of RGW obtained from HFSS. (a) The configuration of wide RGW. (b) Dispersion diagram.

Using HFSS, electric fields distribution of the first three modes propagate on the ridge between 25 GHz to 43 GHz can be obtained, as shown in Fig 4.3. From this figure, it is clear that both of the fundamental mode and second higher order mode have even symmetry while the first higher mode has odd symmetry. All the modes excited within this RGW are propagating along the z-direction. The periodic bed of nails acts as a perfect magnetic conductor (PMC) which satisfies the boundary conditions of this RGW structure.

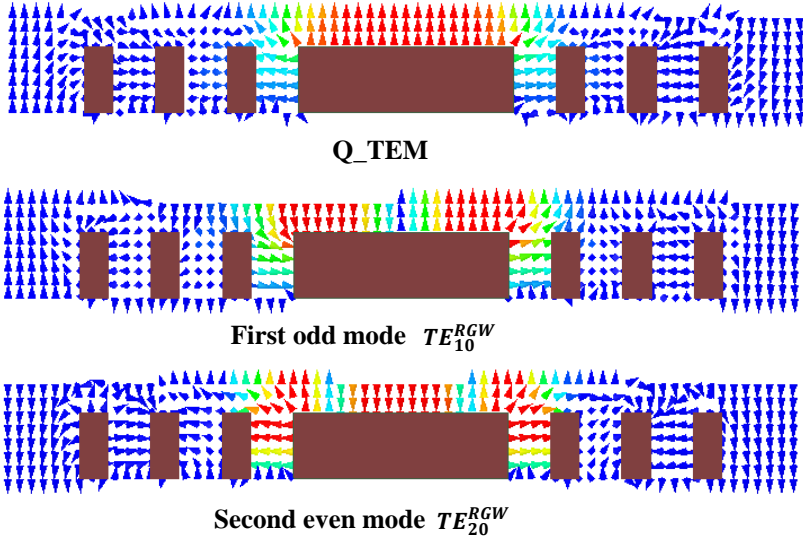


FIGURE 4.3: Electric field distribution of the first three modes proposed wide RGW.

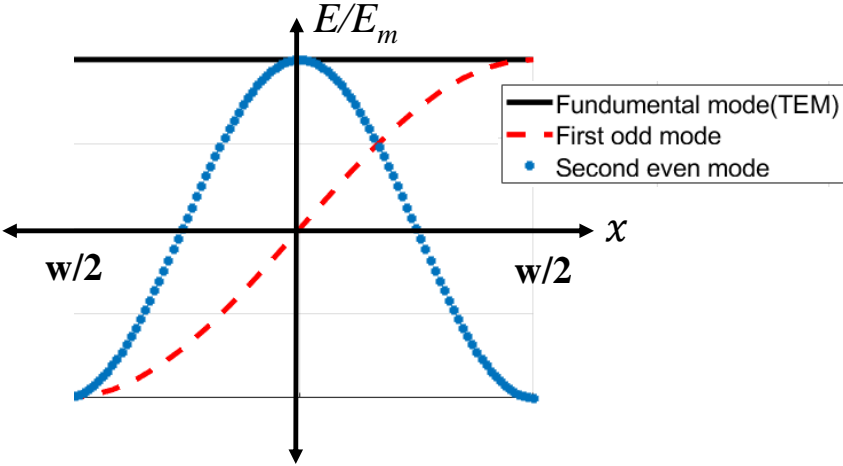


FIGURE 4.4: Cross sectional fields distribution of the first three modes.

By using the hybrid PEC/PMC waveguide, the electric field distribution for the TEM , TE_{10}^{RGW} and TE_{20}^{RGW} modes in the middle of the air gap along the x-axis can be obtained as shown in Fig.4.4 based on equation (3.10). From this figure, it can be shown that the field distribution of the TEM and TE_{20}^{RGW} modes in RGW is maximum in the center and at the PMC walls ($w/2$) while the TE_{10}^{RGW} mode is maximum at the PMC walls and vanishes at the center. Accordingly, both the Q-TEM and the TE_{20}^{RGW} modes shown in the dispersion diagram must be suppressed to guarantee a single-mode operation. Given Fig.4.4, if a vertical PEC wall located on the origin point (0,0) of the graph, the only first odd mode TE_{10}^{RGW} will satisfy the boundary condition at the PEC wall, while the other even modes (Q-TEM and TE_{20}^{RGW}) do not satisfy the new boundary condition, where those modes have a maximum E-field at the center. Therefore, in such a structure with such boundary conditions, only the odd mode will be propagated on the ridge. So by imposing a PEC wall in the middle of the ridgeline, the even modes are eliminated and only the odd mode exists. To prove that, the following ridge gap waveguide with a PEC wall at the middle is investigated and the corresponding dispersion diagram is shown in Fig.4.5 (a). From the dispersion diagram shown in Fig.4.5 (b), there is only one propagating mode TE_{10}^{RGW} , from 25 GHz to 43 GHz.

To verify this analysis, a simulated results of electric fields distribution of the propagated modes of RGW with PEC wall is obtained and shown in Fig.4.5 (c). From this figure, it is very clear that only the odd mode TE_{10}^{RGW} satisfies the new boundary condition. The simulated E-field distribution of the TE_{10}^{RGW} mode in such an RGW structure is shown in Fig.4.6. From this figure, one can notice the odd symmetry of the electric field with respect to the x-axis can be used to create two horizontal slots to differently feed the cavity.

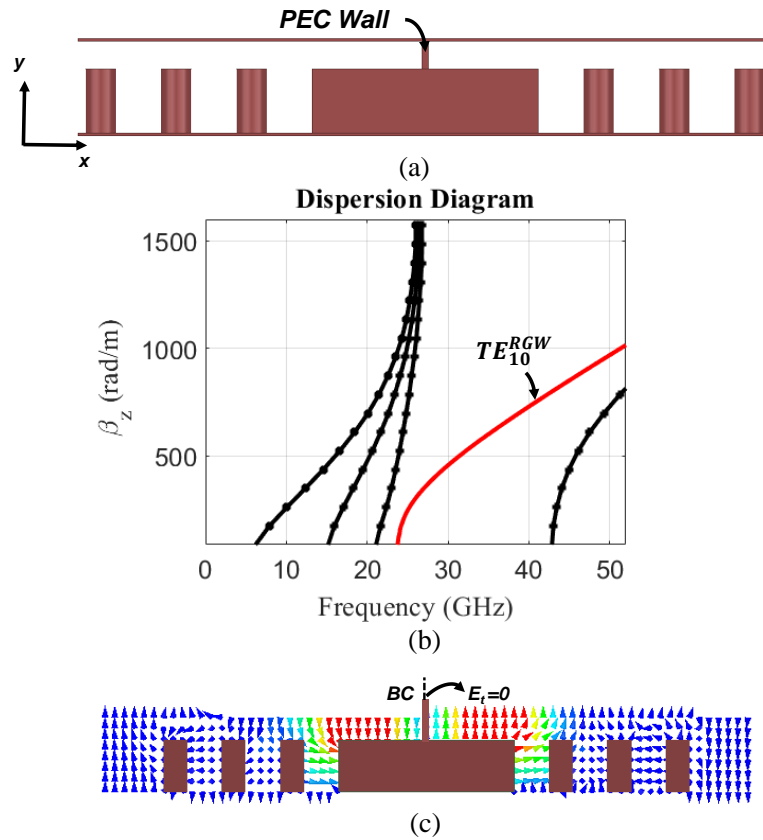


FIGURE 4.5: The configuration of RGW with PEC boundary at the middle and its dispersion curves. (a) The configuration of RGW. (b) Dispersion diagram. (c) Electric field distribution of the RGW.

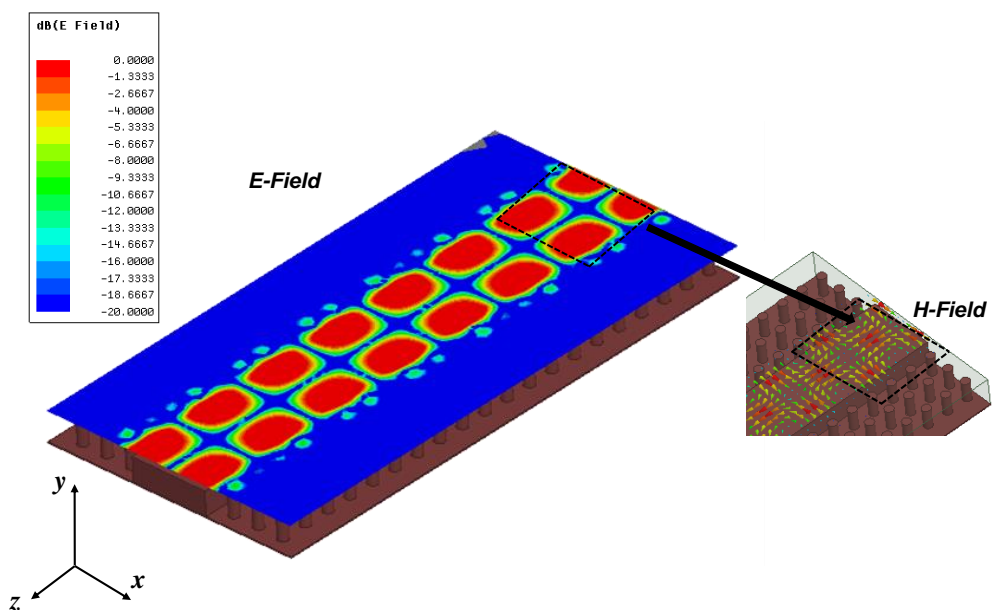


FIGURE 4.6: Electric and magnetic field distribution of the RGW first odd mode TE_{10}^{RGW} (proposed wide RGW).

4.3 Excitation of First High Order Mode by Magic Tee

4.3.1 Magic Tee Implementation

In order to suppress the undesired even modes, to guarantee the propagation of only TE_{10}^{RGW} mode over the bandwidth for single-mode operation, a vertical PEC wall over the ridge is necessary. However, vertical PEC in the form displayed in Fig.4.5 (a) is hard to physically construct. As an alternative solution, the magic tee structure shown in Fig.4.7 can be employed to obtain the same behavior, but with a realizable geometry. The magic tee provides a differential excitation to the ridgeline which imposes a virtual PEC wall in the middle of the ridge. Consequently, only the odd mode TE_{10}^{RGW} is excited on the ridge and the even modes (Q-TEM and TE_{20}^{RGW}) are suppressed. A magic tee is commonly used to feed microwave systems, which consists of four ports and can be utilized as an E-plane or H-plane power dividers. For instance, if the power is applied to the difference port of the magic tee, the power will be equally divided between two ports with a 180° phase shift and the remaining port is isolated. In this work, a short circuit is placed in the isolation port of the magic tee as it does not affect the magic tee performance. Fig.4.7 (a) shows a 3D view of the three-port magic tee configuration with all associated dimensions are listed in Table 4.1. In the shown structure, port 1 is the input port while port 2 and port 3 are the output ports. When exciting this structure at port 1, the power is equally divided between port 2 and port 3 with a 180° phase shift between them as clearly appears in the field distribution of Fig.4.7 (a). A hemisphere is applied as shown in Fig.4.7 (b) in order to improve the matching [50].

TABLE 4.1: Parameters of The Magic Tee

Parameter	W_{in}	L_{in}	W_p	H_p	W_s	L_s	L_{is}	L_p
Value(mm)	7.212	3.556	5.5	0.9	4.4	3.7	5.5	3.4

The simulated magnitude and phase responses of the S-parameters of the designed magic tee are shown in Fig.4.8 (a) and (b), respectively where the transmission levels to

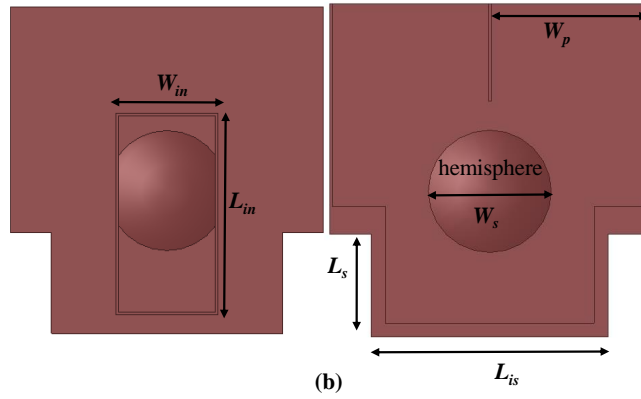
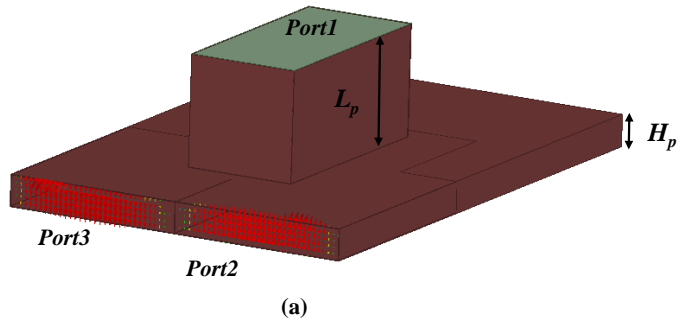


FIGURE 4.7: The configuration of the magic tee transition. (a) 3D view with the electric field distribution. (b) Top view right, middle cut left.

port 2 and port 3 are about -3 dB from 26 to 40 GHz, the reflection level at port 1 is below -20 dB and the phase difference between port 2 and port 3 is 180° degrees.

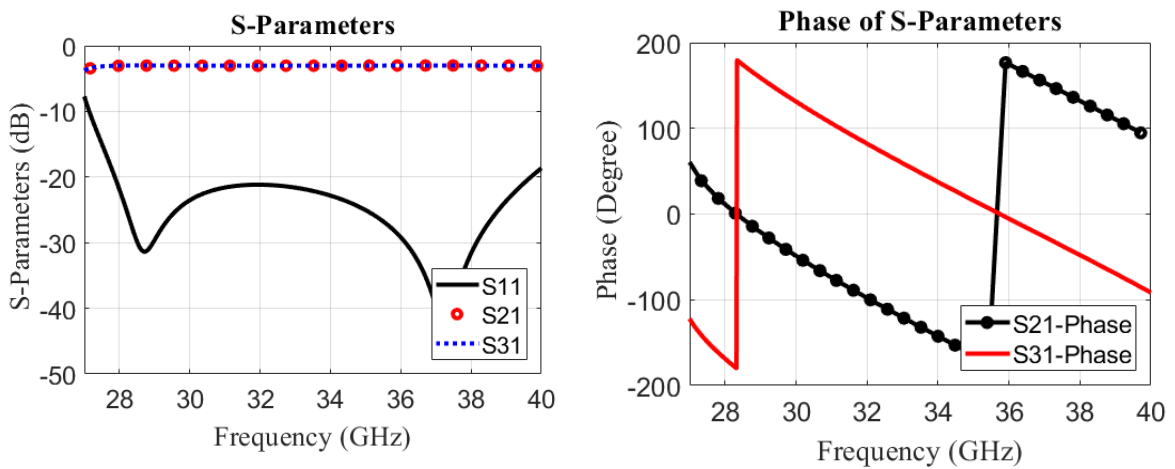


FIGURE 4.8: The magic tee S-parameters. (a) Magnitude. (b) Phase.

4.3.2 RGW Excitation by Magic Tee

To excite the proposed wide RGW, the magic tee shown in Fig.4.7 is used where its output ports 2 and 3 are the inputs to the wide RGW as shown in Fig.4.9, the top metal plate is hidden to show the inside structure. By applying the power to port1 of the magic tee, the power is equally divided between port 2 and port 3 with 180° phase shift. Then those outputs are used as inputs of the proposed wide RGW. Fig.4.9 shows the electric field distribution of the mode that can propagate in this ridge . From the E-field distribution, it is clear that there is only one propagating mode TE_{10}^{RGW} within the ridge with the tangential electric field is zero in the middle of the ridge and maximum on its sides.

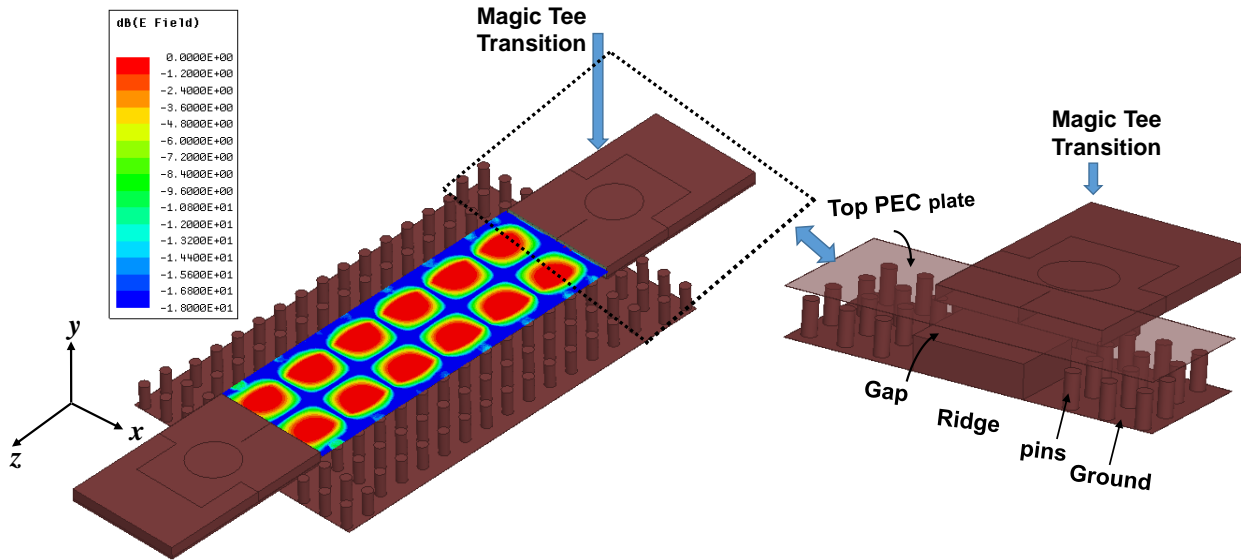


FIGURE 4.9: RGW with the magic tee transition. (a) Electric field distribution of the TE_{10}^{RGW} mode in the proposed RGW.

By applying the superposition method of these two inputs, the even modes are eliminated while only the odd mode propagates inside the wide RGW. The simulated E-field distribution in RGW with the magic tee transition is shown also in Fig.4.9 (a). A very good matching is achieved over the whole bandwidth between 28 GHz and 39 GHz which is shown in Fig.4.10.

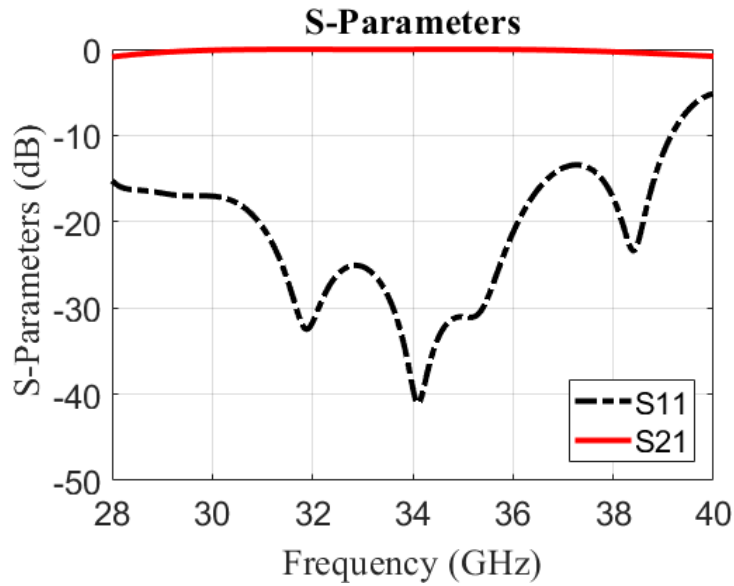


FIGURE 4.10: S-parameters of back to back transition.

4.4 Excitation of First High Order Mode by L-Shape transition

In the this section, the excitation of the first higher order modes is achieved by using an L-shape transition and vias that converts the fundamental Quasi-TEM mode of the RGW to the first higher order mode (first odd mode) and suppress the even modes. The proposed transition has a simple configuration and designed by using metallic (RGW) technology. The proposed structure is simulated using a full wave simulator (CST Microwave Studio).

4.4.1 Odd Mode RGW Transition Design

The odd mode RGW transition is designed based on transforming the regular Q-TEM mode to the desired odd mode. This is achieved by using an L-shape transition. The L-shape provides a 180° phase delay between the two edges of the wide ridgeline. After that, a row of metallic pins in the middle of the wide ridgeline is used to suppress the Q-TEM and the TE_{20}^{RGW} mode. The top view of the proposed structure and all dimensions are shown in Fig.4.11 and table 4.2, respectively. The top plate is hidden to show the internal details.

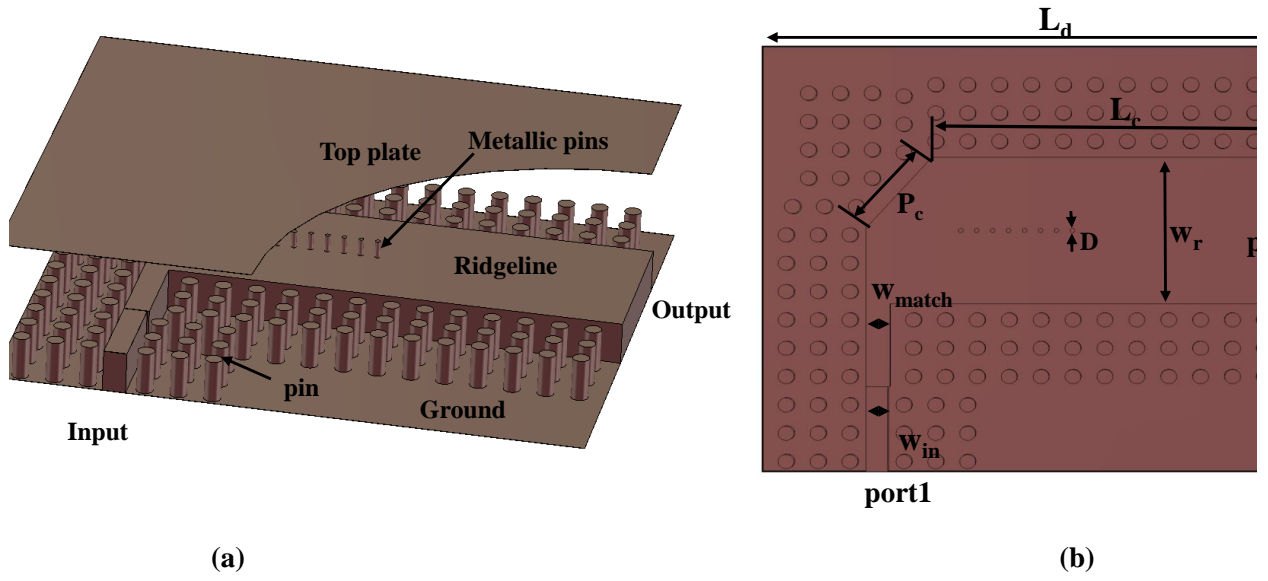


FIGURE 4.11: (a) Odd mode RGW configuration (b) Top view .

TABLE 4.2: Parameters of the transition

Parameter	Value(mm)	Parameter	Value(mm)
P_c	6.5	W_r	10
W_{match}	1.5	W_d	30
W_{in}	1.4	L_d	25
L_c	14.3	D	0.3

The matching is achieved by using a quarter wave transformer between the input port which supports only the Q-TEM mode and the output port that supports the odd mode. The equation of the strip line can be used to have the starting dimension of the ridge line [94].

$$Z_{RGW} = \frac{\eta_0}{2} \left[\frac{W_r}{2h} + 0.0441 \right]^{-1} \quad (4.1)$$

where η_0 is the intrinsic impedance of the air.

An optimization process is carried out to have a wide bandwidth matching. The S-parameters of the proposed odd mode transition is shown in Fig.4.12. The reflection coefficient of this structure is less than -10 dB over 8GHz from 28 to 36 GHz. Where more than 93% of the input power has been transformed into the odd mode at the output port. Fig.4.13 illustrates the electric field distribution on the proposed transition at 32

GHz. It is clear that the Quasi-TEM mode at the input is efficiently converted to the odd mode TE_{10}^{RGW} at the output port.

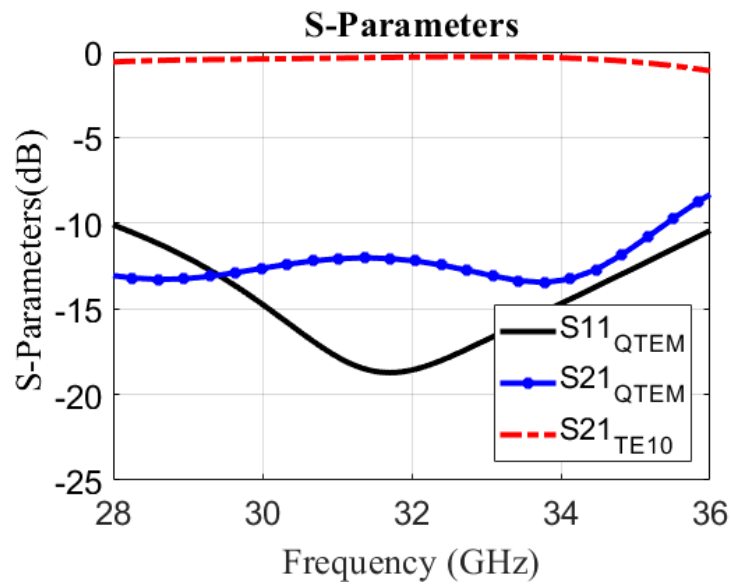


FIGURE 4.12: The magnitude of the proposed RGW odd mode S-parameters

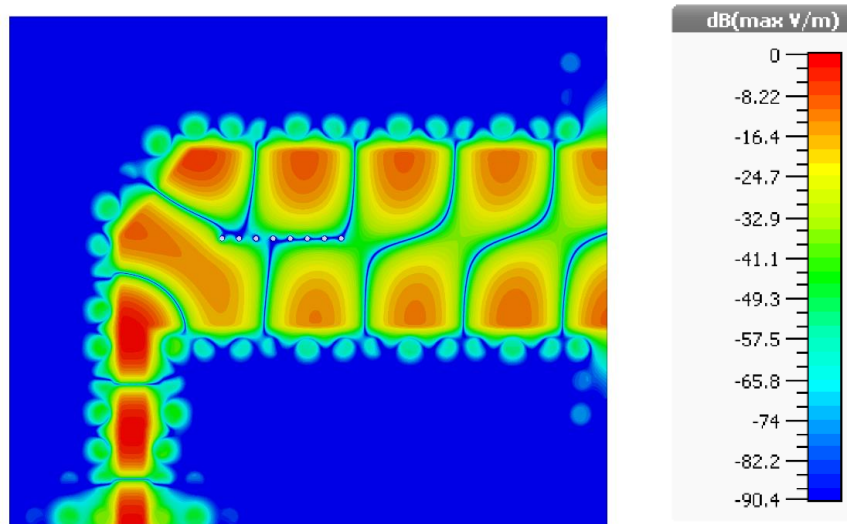


FIGURE 4.13: The field distribution for the proposed odd mode RGW transition at 32 GHz .

The proposed transition introduces simple structure to excite the first higher order mode of the RGW as a fundamental mode instead of the conventional Q-TEM mode. The

structure is fed by a Q-TEM mode at the input port then it is transformed into the odd mode at the wide ridgeline. The whole structure has achieved a matching level of less than -10 dB from 28 to 36 GHz. With the proposed waveguide, the odd mode can be used which has a great potential for millimeter-wave devices that needs the use of higher order modes.

4.5 RGW Y-Junction Based on First High Order Mode

Ridge gap waveguide and slot array antennas have been a remarkable topic among microwave components and the antennas designers. Typical RGW components and antennas can be lightweight and compact. Also, it can offer low losses as the field propagates in the air rather than propagates in a dielectric substrate which suffers from dielectric losses, especially at high frequencies. Moreover, when design an array antenna based on conventional waveguide for high gain or multiple beam application, the efficiency of antenna decreases as losses increased. Furthermore, any discontinuities in the feeding network cause a radiation loss [95].

Recently developed the RGW technology verified in [96,97] which can be used to address most mentioned issues. Thus, the RGW power divider to feed slot array antenna can be used in many applications. As we discussed necessity exploit high order mode in RGW to improve the performance of antenna feeding network, till now, there has not been any work on high order mode RGW antennas. Therefore A novel Y-junction power divider structure based on the first higher order mode (TE_{10}^{RGW}) mode of RGW is introduced.

The proposed odd mode power divider has a simple configuration based on metallic (RGW) technology. The fundamental mode through this structure is the odd mode of RGW (First high order mode) rather than the usually-studied quasi -TEM mode. The first higher order mode of the RGW (TE_{10}^{RGW}) is used to excite the Y-junction by expanding the ridge width, and suppressing both of the Q-TEM and (TE_{m0}^{RGW}) modes, where ($m = 2,4,6..$). Due to the nature of the field distribution of an odd mode through RGW, two

of half wavelength can be generated successively. This kind of field distribution allows etching two horizontal slots successive in phase during half wavelength, in which this completely removes grating lobes in E-plane and reduces the beamwidth in H-plane. The resulting proposed structure is implemented through well-known full wave simulator, Ansoft HFSS.

4.5.1 First High Order Mode RGW Y-Junction Design Procedure

Y-junction is a basic component of an array antenna as a feed network, where commonly consists of transformer sections. It is well-known that the even and odd modes have different impedance, so each kind of mode could suit various applications. From this point, we decided to study the design of the odd mode RGW Y-junction power divider. Where the propagating mode in the structure is odd mode rather than the usually-studied even mode. Here we describe how the proposed Y-junction based on higher order mode RGW is designed, and how it works in two cases:

1. Ideal Case

The ridge line of proposed Y-junction is designed with a width supports first high order mode as shown in Fig.4.14. A suitable transformer section is used to match different parts of ridge line. As an ideal case, we use vertical PMC boundary conditions surround the ridge instead of using bed of nails as shown in Fig.4.14 (a). In this figure, the upper ground is hidden to show the internal details of the structure. Two rows of matching vias and matching steps, which are symmetrical with respect to the x -axis, and are used to improve the matching level. The structure is designed and optimized using HFSS. Considering the boundary conditions, two vertical PMC boundaries on the YZ -plane on the both sides of the ridge line are set in software. This helps in saving the processing time and improves the accuracy of the results. Then, dimensions have been optimized in order to reach the best values as they are listed in table 4.3. The three arms of Y-junction are divided such away in order to

set the bed of nails that required to create PMC boundary. The simulated magnitude and phase responses of the S-parameters of designed Y-junction are shown in Fig.4.15 (a) and (b), respectively where the transmission levels to port 2 and port 3 are about -3 dB from 28 to 34 GHz, the reflection level at port 1 is below -15 dB and in phase.

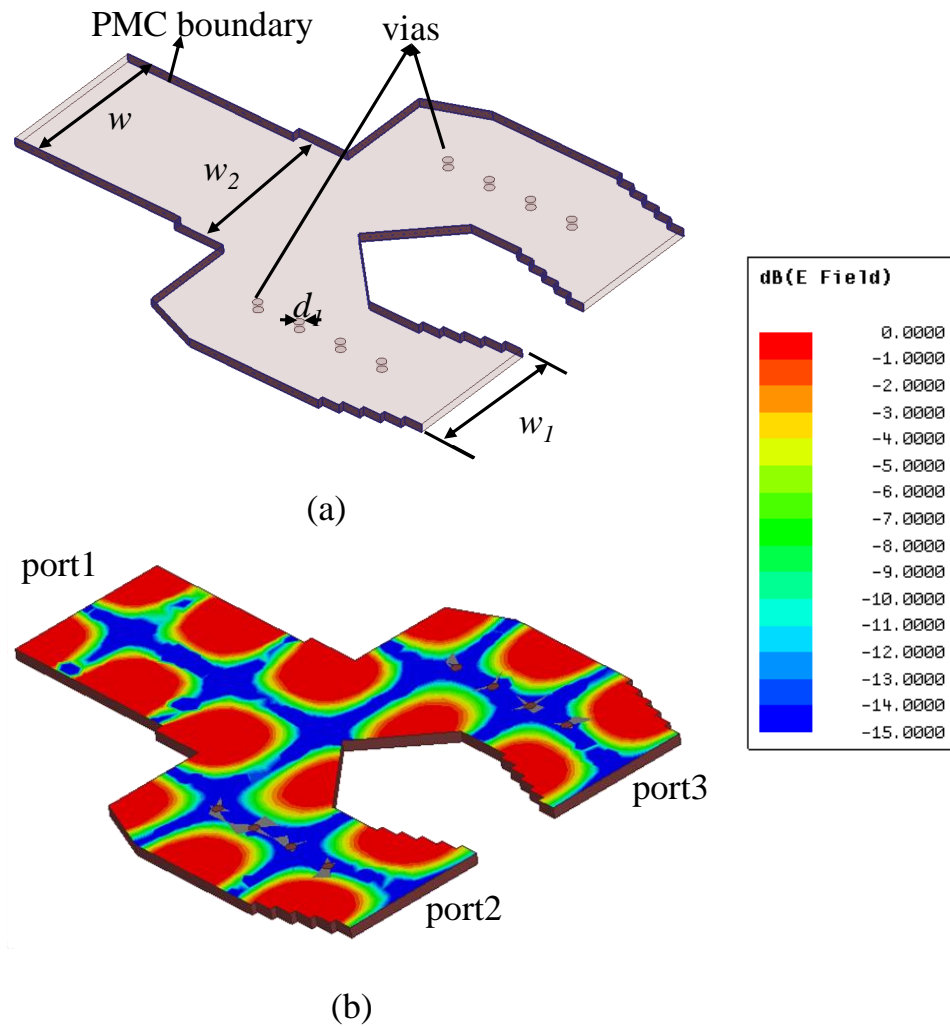


FIGURE 4.14: Y-Junction RGW based on first higher mode with ideal PMC boundary conditions. (a) Structure top view. (b) Simulated electric field distribution

TABLE 4.3: Parameters of the Y-Junction

Parameter	W	W_1	W_2	d_1
Value(mm)	8.1	7.28	9.2	0.5

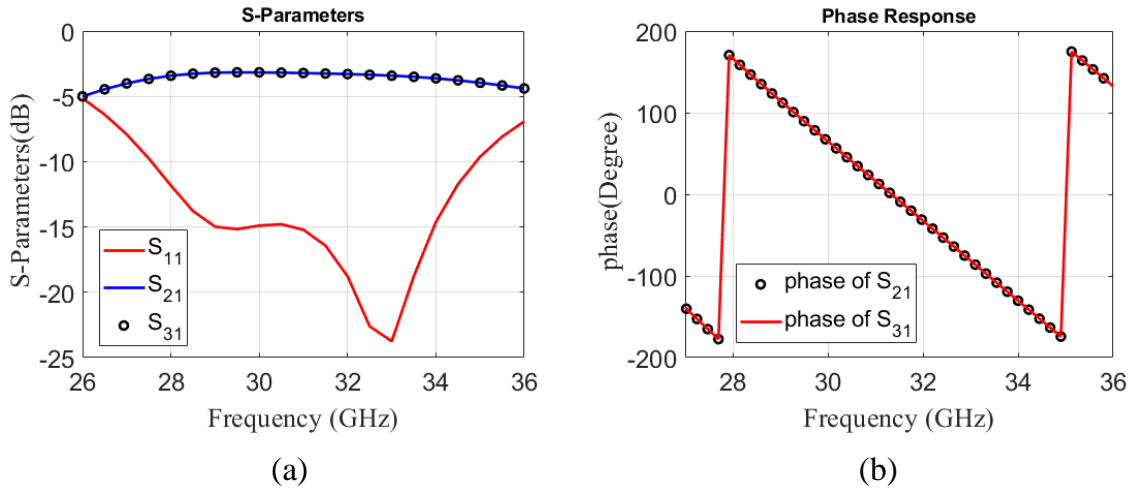


FIGURE 4.15: The Y-junction S-parameters. (a) Magnitude. (b) Phase

2. Realized Case

The realized case of Y-junction is to replace the vertical PMC boundary with periodic nails. The configuration of the unit cell and its dispersion diagram is shown in Fig. 4.1 (a,b). It can be illustrated from the dispersion diagram of the unit cell that the stopband of the unit cell covers from 25 to 40 GHz. The structure of the unit cell and dispersion relation are designed and obtained using the eigenmode solver.

The realized structure of RGW Y-junction is shown in Fig.4.16 (a). Fig.4.16 (b) shows the electric field distribution of the mode that can propagate in this structure. From the E-field distribution, it is clear that there is only one propagating mode within the ridge with the tangential electric field is zero in the middle of the ridge and maximum on its sides. The simulated magnitude and phase responses of the S-parameters of the designed Y-junction are shown in Fig.4.17 (a) and (b), respectively where the transmission levels to port 2 and port 3 are about -3 dB from 28 to 34 GHz, the reflection level at port 1 is below -15 dB. From the results, it clear that there is an agreement between the ideal case results and realized case, in which this will be helped to save the processing time and improve the accuracy of results. By using the Magic tee designed in Sec 4.3.1, we can implement effective Y-Junction based on the first order mode RGW.

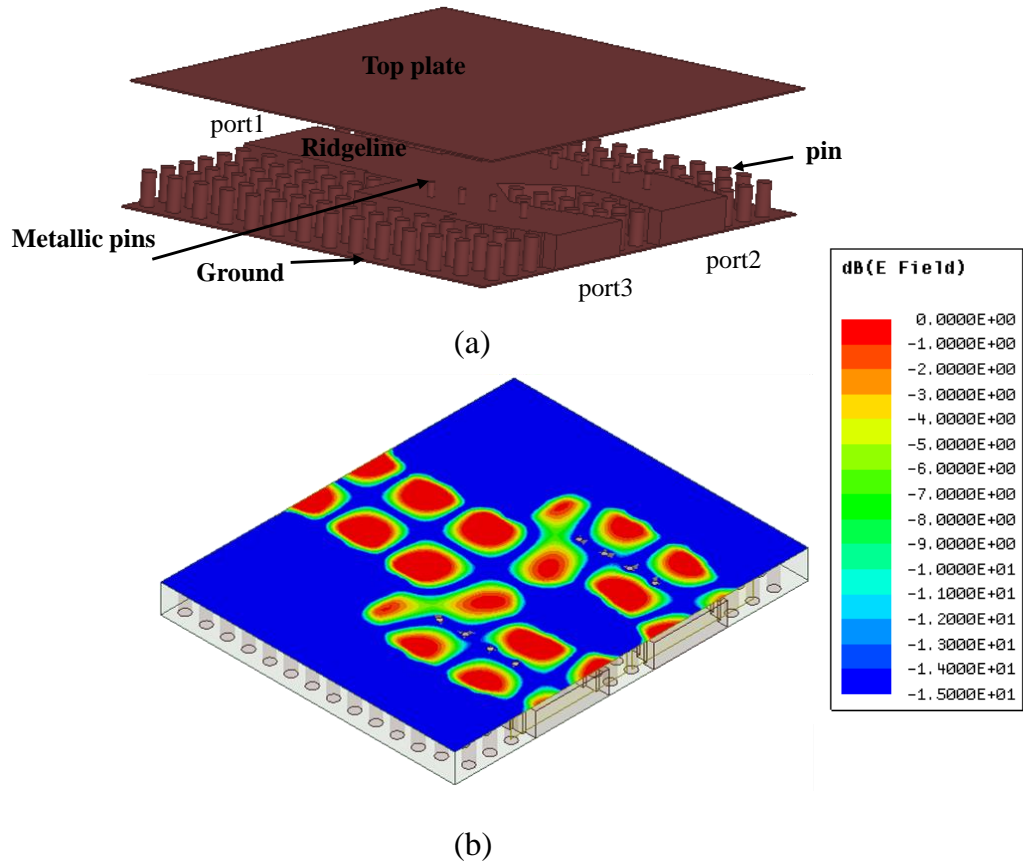


FIGURE 4.16: The Y-junction RGW based on first higher mode with bed of nails. (a) Structure side view. (b) Electric field distribution.

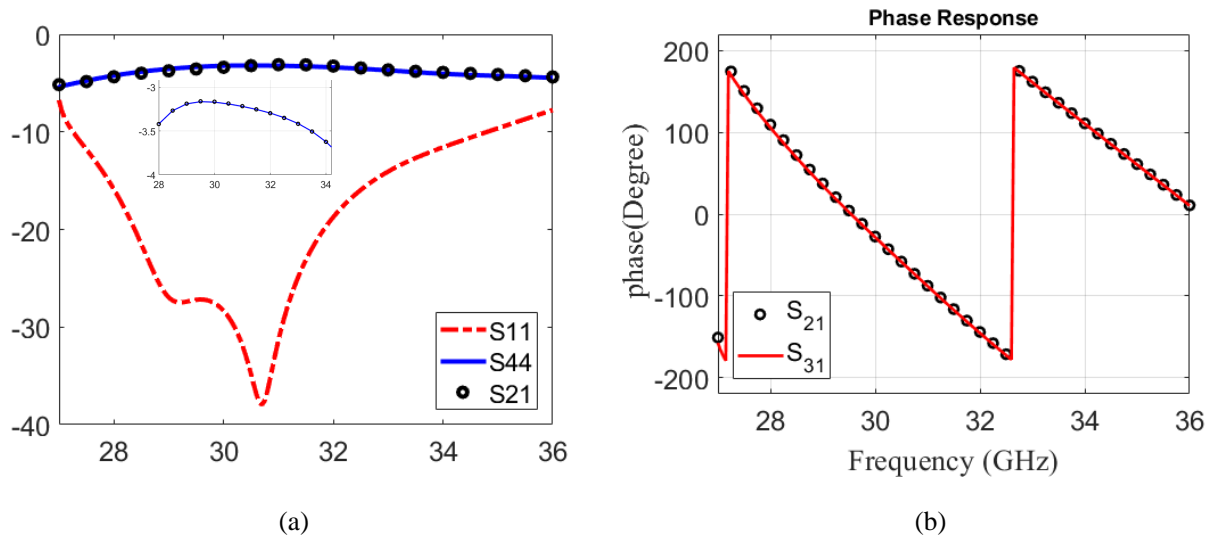


FIGURE 4.17: The Y-junction RGW based on first higher mode with bed of nails. (a) Structure top view. (b) Electric field distribution.

4.6 Hybrid Forward Coupler Based on First Higher Order Mode RGW

In general, the hybrid coupler can be designed to achieve theoretical coupling levels as high as 3 dB or 0 dB. The coupling phenomenon discussed in this section is mainly based on the concept of the Riblet coupler [41]. The Riblet coupler consists of two rectangular waveguides placed parallel to each other. The common wall is the short wall and this wall is totally opened between the guides for a certain coupling length, hence the name “short-slot” coupler. The main goal in this section is to develop the hybrid coupler based on the odd mode RGW. We call this new type “RGW Odd Mode” coupler. Where the fundamental propagating mode in the input ports of this coupler is first high order mode rather than the usually-studied quasi-TEM mode.

4.6.1 3dB Hybrid Coupler

Starting with the same analysis of Riblet coupler. Since, the fundamental mode through the input ports of this structure is first high order mode of RGW TE_{10}^{RGW} rather than the usually-studied quasi-TEM mode, the coupling length depends on the propagation constants of the first higher order mode and second higher order mode in the common section between the two waveguides. Hybrid PEC/PMC coupler which is presented in Chapter 3 is deployed in order to calculate the coupling length. The required coupling level is achieved based on this specific coupling length l_c . The width of coupling section in this design should be more than two times of the waveguide width to allow the third high order mode to propagate in the waveguide. The configuration of the hybrid PEC/PMC coupler is shown in Fig. 4.18 (a), where all the vertical “short” walls are PMCs and the horizontal walls are PECs. Ideally, the power fed to the structure from port1 is divided equally between ports 2 and 3 with phase shift $\pi/2$ between the outputs 1 and 2, and with full isolation at port 4.

Since the input of the coupler is odd mode and designed frequency is 32 GHz, the ridge width is selected to be 6 mm to support TE_{10}^{RGW} mode. As shown in Fig 4.18 (a). in order to improve the matching and isolation level, a row of vias is centered in the air gap between the top and bottom plate in all ports.

TABLE 4.4: Parameters of the 3dB Coupler

Parameter	Value(mm)	Parameter	Value(mm)	Parameter	Value(mm)
l_{total}	29.5	w_c	16	L_c	9.1
L_{sin}	10	w_B	4	$d_{matching}$	0.4
d_{center}	0.5	h_{gap}	0.5	d_{period}	2

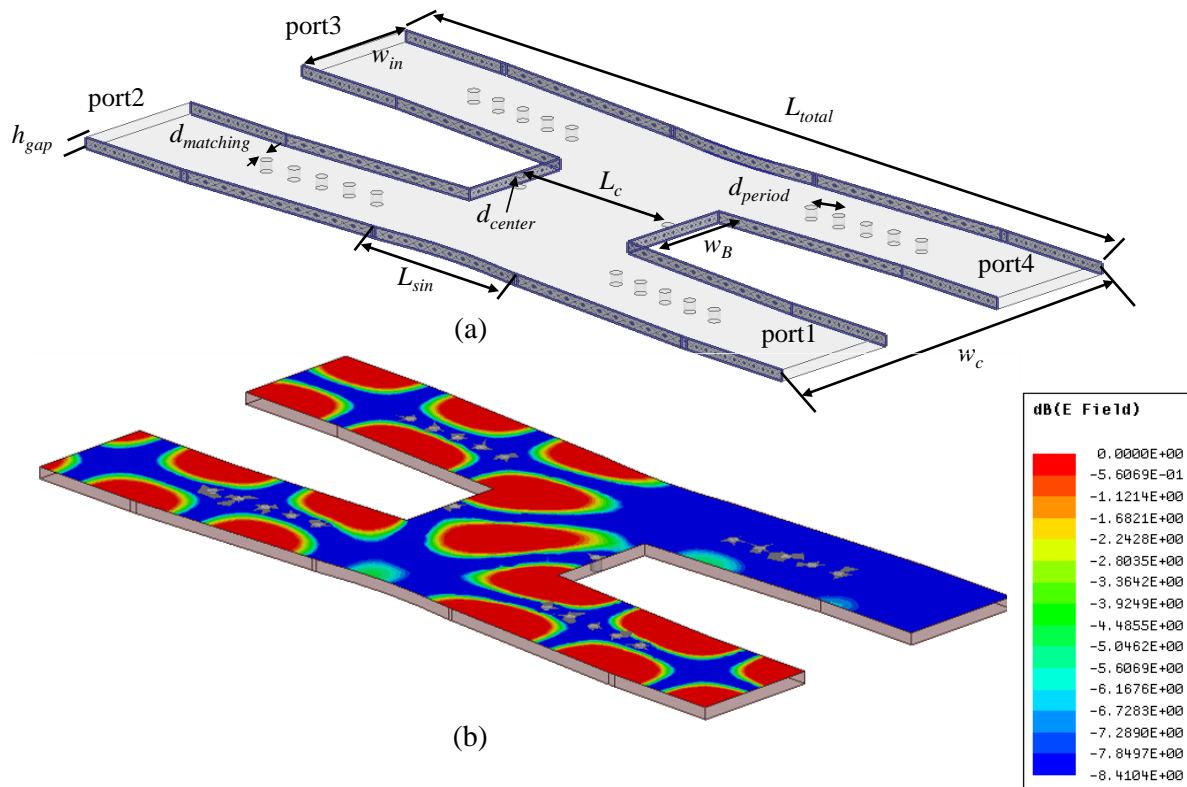


FIGURE 4.18: 3dB Hybrid PEC/PMC Coupler, (a) geometry, (b) electric field distribution at 32GHz.

The simulation results expose the ability to design a forward coupler, where the coupling occurs in the coupling section. The simulated S-parameters of the proposed hybrid PEC/PMC waveguide coupler is shown in Fig. 4.19, where the coupling level at port 2 and port 3 is about about 3 dB from 28 GHz to 35 GHz, the isolation level at port 4 is below -15 dB. Accordingly, it could be confirmed that the power is divided equally between

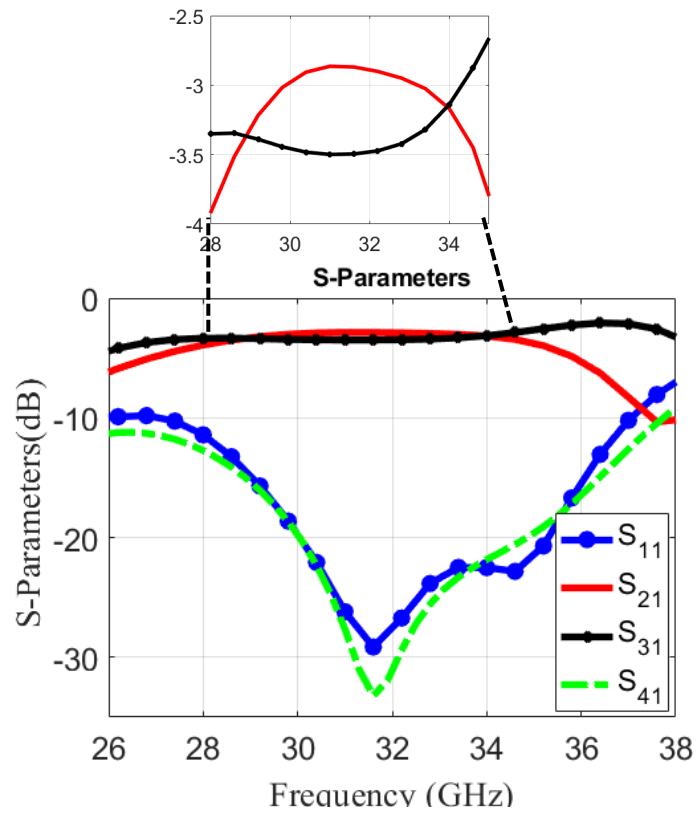


FIGURE 4.19: S-parameters of the proposed 3dB hybrid PEC/PMC waveguide coupler

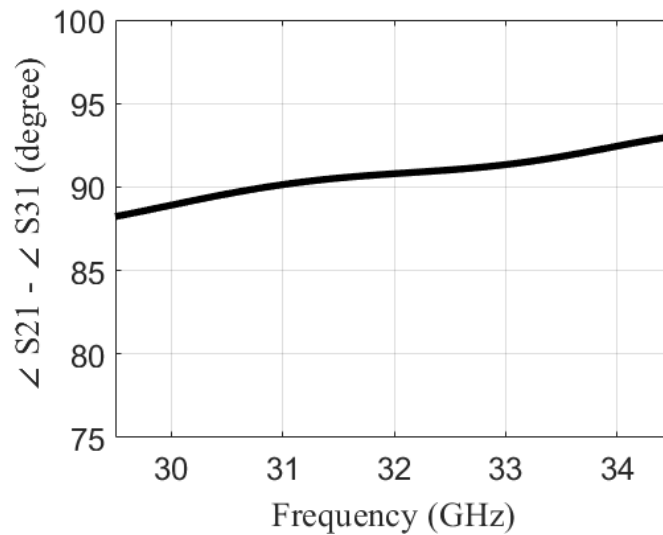


FIGURE 4.20: Phase response of the proposed 3dB hybrid PEC/PMC waveguide coupler

port 2 and port 3 at the design frequency. Fig.4.20 illustrates the phase difference between $|S_{21}|$ and $|S_{31}|$ which equal a 90° with a phase imbalance of $\pm 5^\circ$.

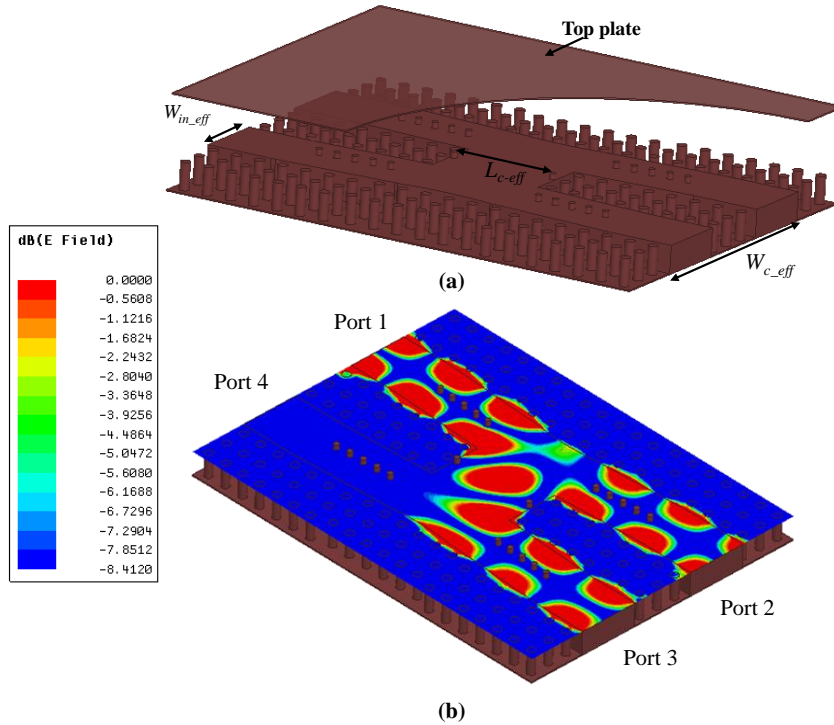


FIGURE 4.21: 3dB Hybrid Coupler, (a) geometry, (b) electric field distribution at 32 GHz.

The final phase in the design of 3 dB coupler is to replace the PMC boundary walls with bed of nails. The unit cell design is presented in Sec4.2.1. Using the HFSS, the proposed 3dB coupler can be simulated to obtain of the S parameters, where all the dimensions are the same what is listed in Table 4.4 except the width of the input and coupling section. The width of any RGW is not the physical width, but it is an effective width that should be obtained from its dispersion. Two unit cell rows should be located between the ports of 3 dB coupler RGW to guarantee the period cell and bottom plate act as PMC boundary. The final configuration is displayed in Fig.4.21 (a), while the electric field distribution illustrated in Fig.4.21 (b). From the figure of the electric field distribution, it is clear that the power is divided between Port 2 and Port 3 with $\pi/2$ phase difference.

simulated scattering parameters of the 3 dB coupler with using bed of nails instate using PMC/PEC boundary are shown in Fig.4.22. From s-parameters results its clearer

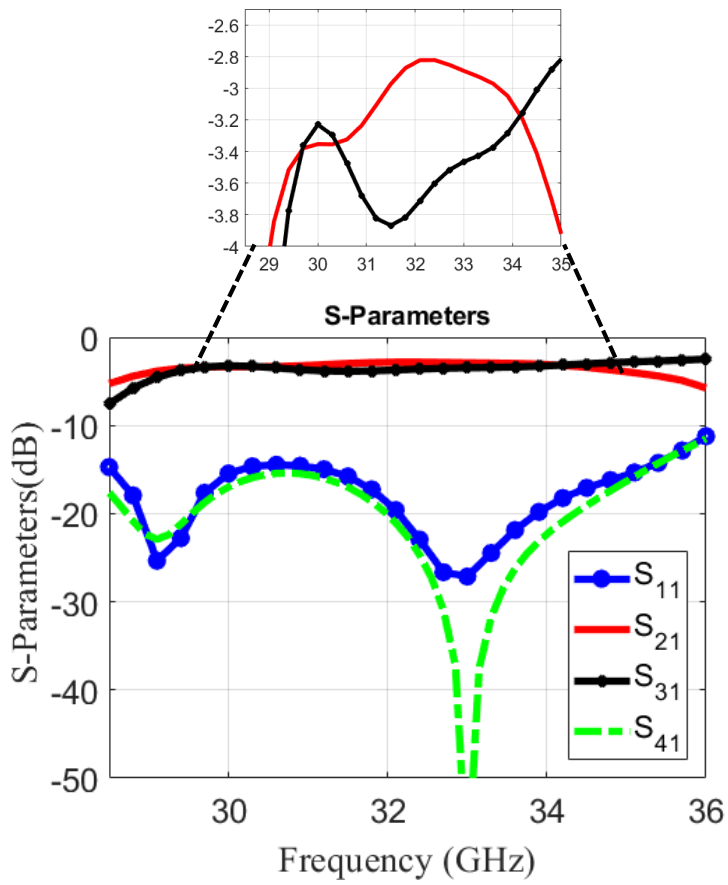


FIGURE 4.22: Scattering parameters of the 3dB coupler.

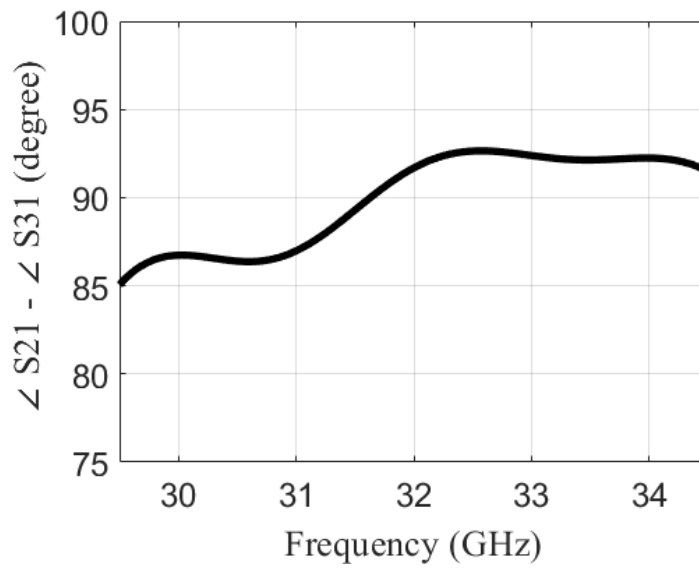


FIGURE 4.23: Phase difference between Port2 and port3($\angle S_{21} - \angle S_{31}$).

that the reflection coefficient and isolation between ports 1 and 4 are better than 15 dB from 29 to 35 GHz . Accordingly, it could be confirmed that the power is completely divided equally between port 2 and port 3 at the design frequency. Fig.4.23 illustrates the phase difference between $|S_{21}|$ and $|S_{31}|$ which equal a 90° with a phase imbalance of $\pm 5^\circ$.

4.7 Design of Dual Mode Ridge Gap Waveguide

Currently, a wide bandwidth (high channel capacity) is required to meet the requirements of new applications such as augmented reality, virtual reality, and the internet of things (IoT), as limitations of the channel bandwidth restricts the system performance. Therefore, high data rate and wide bandwidth transmission channels are in demand. Usually, a parallel structure design with some transmission lines is utilized to provide high data rates [98]. However, the parallel systems' performance is restricted by the number of lines and by the bandwidth of each line, which is relatively narrow. Using a high number of line leads to fabrication challenges, as they need to have high isolation and occupy a large area. Various solutions, such as multilevel coding, differential signaling, and equalization are used to provide high data rates [99–102]. However, these solutions result in increasing the system complexity and the power consumption.

Due to the advantages of using the substrate integrated waveguide (SIW) in communication systems, multimode SIW devices have been investigated and utilized to increase the channel capacity. SIW technology offers low losses compared to the traditional microstrip technology [103,104], as the radiation losses are eliminated, but it still suffers from dielectric loss.

Over the last two decades, SIW interconnections have been introduced to achieve high data rates for signal transmission [105,106]. However, the main restriction in using a SIW is the need for a large transmission line width compared to the microstrip or the strip line technologies. This problem was addressed in [85,107] by reusing the volume of the waveguide to transmit another signal with the SIW fundamental signal. This reuse

was accomplished by inserting a stripline into the waveguide which allowed multimode transmission in the same waveguide; this method is called a hybrid SIW.

Furthermore, since the SIW interconnections have an enclosed structure, the wave is totally confined in this structure, which result in elimination of the crosstalk between the channels and the electronic circuits [28, 108, 109]. The multimode transmission concept is applied in [13] by using the TE₁₀ and TE₂₀ modes to provide a high data rate to an SIW interconnect. Meanwhile, the bandwidth of the TE₁₀ channel is limited by the cutoff frequency of the TE₂₀ channel. That method uses two separate bands for each mode, contrary to the orthomode transducer (OMT), which uses the same band with different polarizations.

In [57, 58], an orthomode transducer is used for receiving and transmitting two signals with orthogonal polarizations through the same waveguide. The OMT is bulky, which is not directly compatible with printed circuit feeds, and it requires expensive machining to be implemented at the high-frequency band.

A dual-mode concept is exploited in this work to double the channel capacity of millimeter wave guiding structure. A ridge gap waveguide transmission line is implemented to feed a sum and difference beam switching antenna. The fundamental mode (Q-TEM) and the first higher-order mode (TE_{10}^{RGW}) are excited to the guiding structure using a magic tee junction. The dual mode transmission line design achieves a matching level less than -10 dB for the two modes over the operating band 28.77 GHz to 34.61 GHz with high isolation between the input ports. The proposed structure is fabricated using CNC technology. The simulated and measured results are in a good agreement. It is demonstrated that the proposed dual mode waveguide can be used to generate two different radiation patterns depending on the excited mode.

In this section, a four-port magic tee is used to excite the quasi-TEM and the first higher-order (TE_{10}^{RGW}) of RGW simultaneously. Both of these modes have the same polarization. After that, a dual mode transmission line is designed, fabricated, and measured. The advantage of the proposed work is the use of the same frequency band for both modes simultaneously.

4.8 High order modes concept of RGW

In order to achieve a dual-mode RGW, two steps are required. First, the design of a bandgap unit cell is needed, to confine the wave on the ridge line. Second, the design of a wide ridge line that can support two modes is required. In this section, the modes on a wide ridge line are investigated.

4.8.1 Bandgap of unit Cell

The band gap of the unit cell is chosen to be from 25 GHz to 42 GHz that cover the whole ka band. The design is close to the one presented in the this chapter where the cell is formed by metallic cylinder with height $d = 2.3$ mm, period $a = 2.5$ mm, radius $b = 0.5$ mm, and air gap height $h = 1.25$ mm. Computer simulation technology (CST) is used to obtain the dispersion diagram of the unit cell as shown in Fig.4.24, where the band gap is from 22 GHz to 42 GHz.

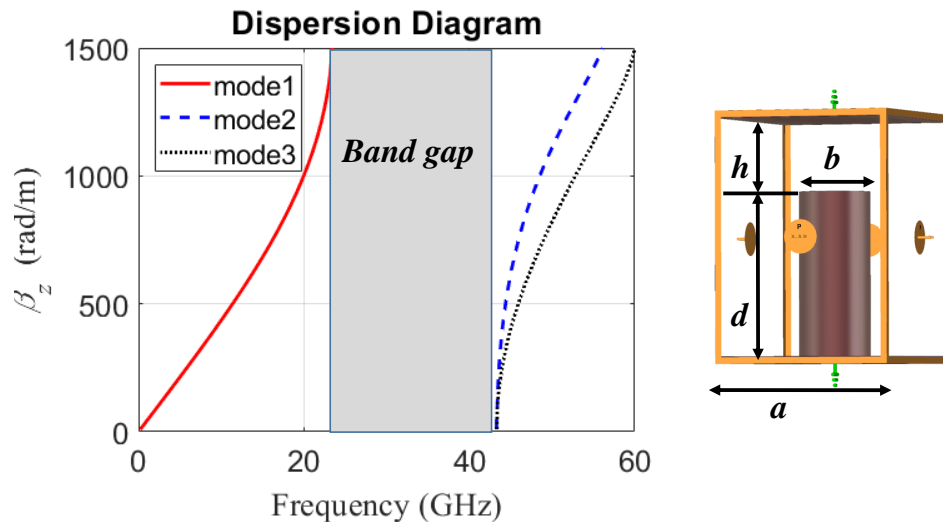


FIGURE 4.24: The configuration of unit cell and its dispersion diagram.

4.8.2 RGW Section

The RGW consists of two parallel plates, an upper metal plate, and a bottom plate which has a metal ridge line in the middle surrounded by the designed unit cells from each side.

In order to design a dual-mode RGW, the ridge width is chosen to guarantee the presence of both fundamental and first higherorder modes over the operating bandwidth. When the wide ridge is excited properly, the two modes can simultaneously propagate along the ridge line.

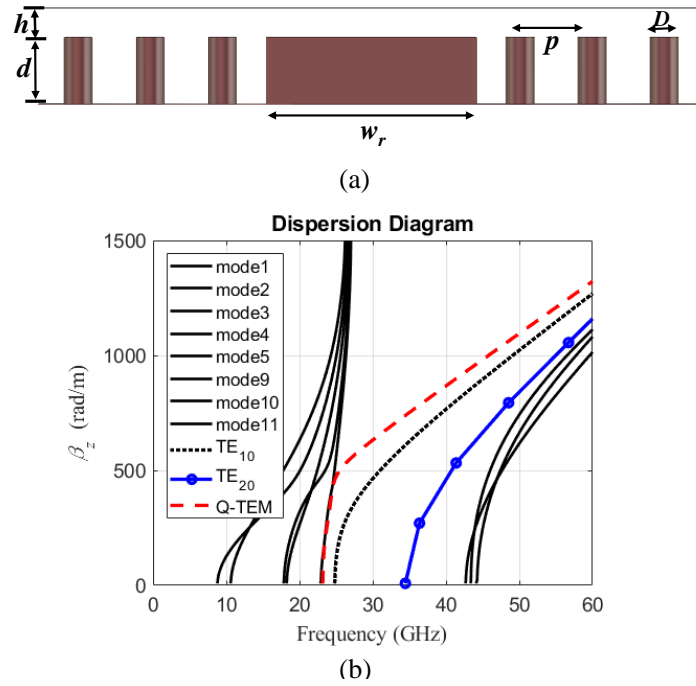


FIGURE 4.25: The RGW section and its dispersion diagram.

In Sec 4.3, the first higher order mode is excited using an E-plane T- junction. In this section, a magic Tee is used to excite both the fundamental mode Q-TEM and first higher mode TE_{10}^{RGW} simultaneously on the same ridge line. The width (w) of the ridge is chosen to be 7.288 mm that guarantee the propagation of both modes. The propagating modes on the ridge line are: (1) the quasi-TEM mode, (2) the first high order mode TE_{10}^{RGW} , and (3) the second high order mode TE_{20}^{RGW} as depicted in Fig.4.25 (b). The bandpass region of the dual-mode is from 25 to 34.5 GHz, that avoids the presence of the TE_{20}^{RGW} mode. The other modes that appear on both sides of the bandpass region are out of the scope of this work. The simulated E-field distributions of the first three modes of RGW structure (Q-TEM, TE_{10}^{RGW} and TE_{20}^{RGW}) are shown in Fig.4.26. It is clear that the fundamental mode Q-TEM and the second higher order mode TE_{20}^{RGW} have even symmetry while the TE_{10}^{RGW}

mode has odd symmetry. The electric field distribution of the first three modes of RGW as shown in Fig.4.26 are generated by defining the port and setting these modes.

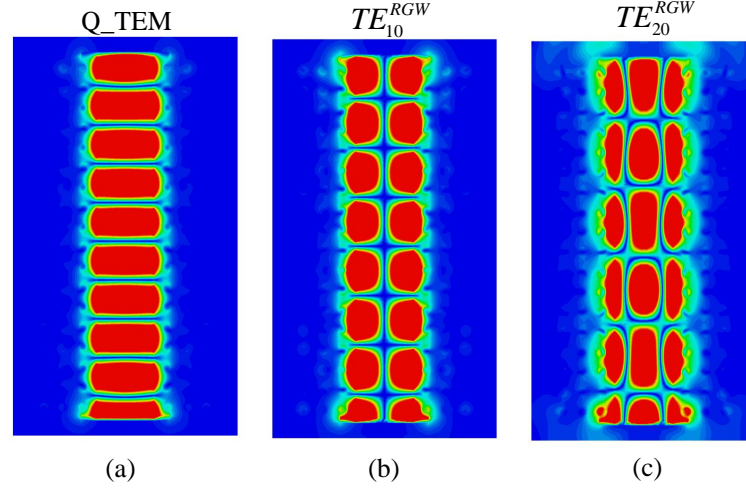


FIGURE 4.26: Electric field distribution of (a) Q-TEM mode (b) TE_{10}^{RGW} mode. (c) TE_{20}^{RGW} mode.

The quasi-TEM and TE_{m0}^{RGW} modes are orthogonal modes in the RGW structure. Consequently, these modes can be used for carrying several signals with low interference through the same waveguide. Therefore, by using proper excitation for RGW, Q-TEM and TE_{10}^{RGW} modes can be sent simultaneously on the same waveguide. This is achieved, in this work, by using a four-port magic tee to feed the wide RGW.

4.9 Higher order Mode Excitation

Generally, several transitions are used to excite high order mode in the conventional waveguides. For example, many different techniques use to excite the SIW high order mode [12, 14, 86]. However, there is no enough reported information about transitions to excite high order mode in RGW. In this thesis, the magic tee is used to excite the Q-TEM and the TE_{10}^{RGW} on the ridgeline. The magic tee is commonly used to feed microwave systems, where it consists of four ports and can be used as an E-plane or H-plane power dividers. Fig.4.27 shows a 3D view of the four-port magic tee structure and the associated dimensions are in Table 5.1. A hemisphere is used, as shown in Fig.4.27 (b), to improve

the matching level [44]. When power is applied on the difference port (Port 1) of the magic tee, the power is equally divided between the two output ports (Port 2 and Port 3) with 180° phase shift as shown in Fig.4.28 (a) while Port 4 is isolated (Port 1 is used to excite the TE_{10}^{RGW} mode on the ridgeline). When power is applied on the sum port (Port 4) of the magic tee, the power is equally divided between the two output ports (Port 2 and Port 3) with the same phase as shown in Fig.4.28 (b) while Port 1 is isolated (Port 4 is used to excite the Q-TEM mode on the ridgeline).

TABLE 4.5: Dimensions of the magic tee

Parameter	Value(mm)	Parameter	Value(mm)
W_{in}	3.556	L_{s2}	1.55
L_{in}	7.212	W_s	4.4
W_p	6.2	d_{iv}	3.5
L_{s1}	1.42	W_d	3.4

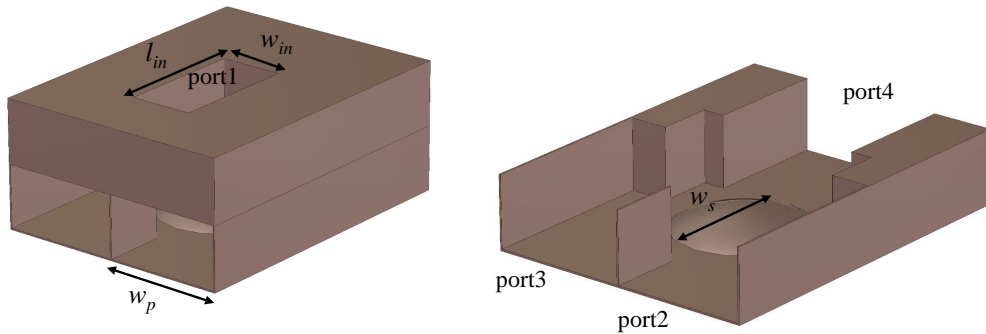


FIGURE 4.27: The configuration of the magic tee transition. (a) 3D view without the top plate. (b) 3D side view of the magic tee transition.

The simulated magnitude responses of the S-parameters of the designed magic tee are shown in Fig.4.29 (a,b) where the transmission levels to Port 2 and Port 3 are about -3 dB from 28 to 35 GHz. The reflection coefficient at Port 1 is below -15 dB and the phase difference between Port 2 and port 3 is 180° as shown in Fig.4.29 (a) and Fig.4.30 (a) , while the reflection coefficient at Port 4 is below -20 dB and the output ports are in phase as shown in as shown in Fig.4.29 (b) and Fig.4.30 (b), respectively.

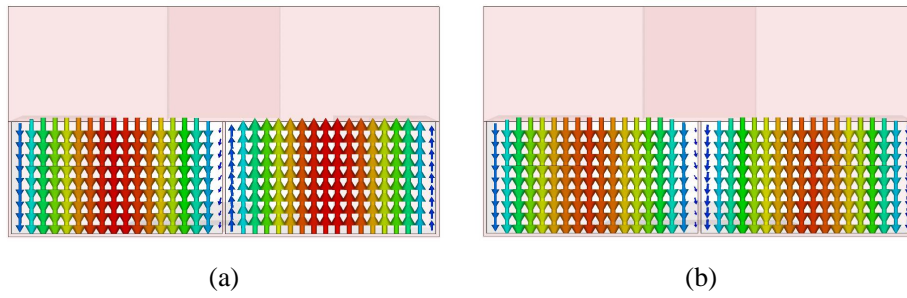


FIGURE 4.28: 2D view with the electric field distribution in port2 and port3 (a) the electric field distribution in port2 and port3 when the input from port1, (b) the electric field distribution in port2 and port3 when the input from port4.

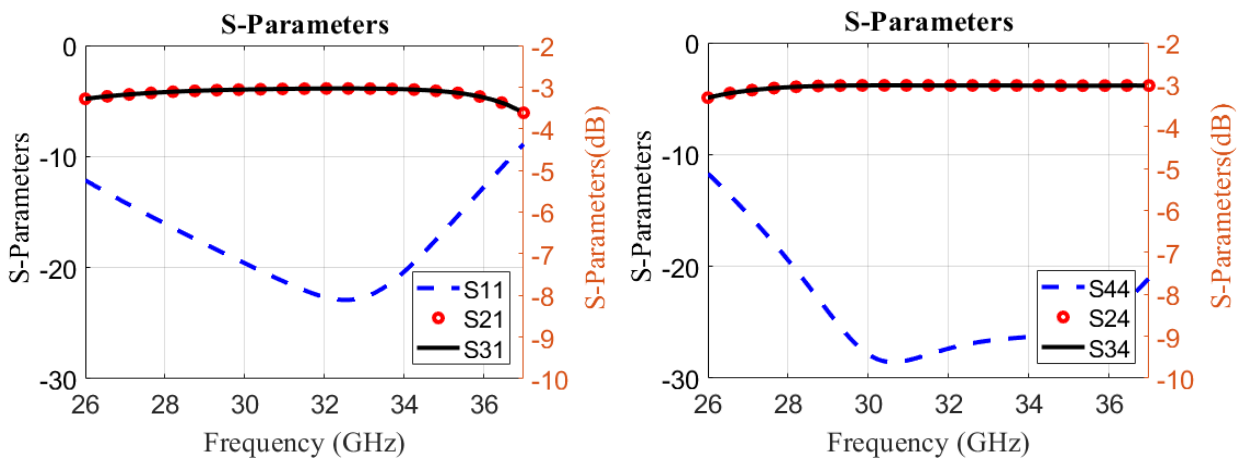


FIGURE 4.29: The magnitude of magic tee S-parameters.

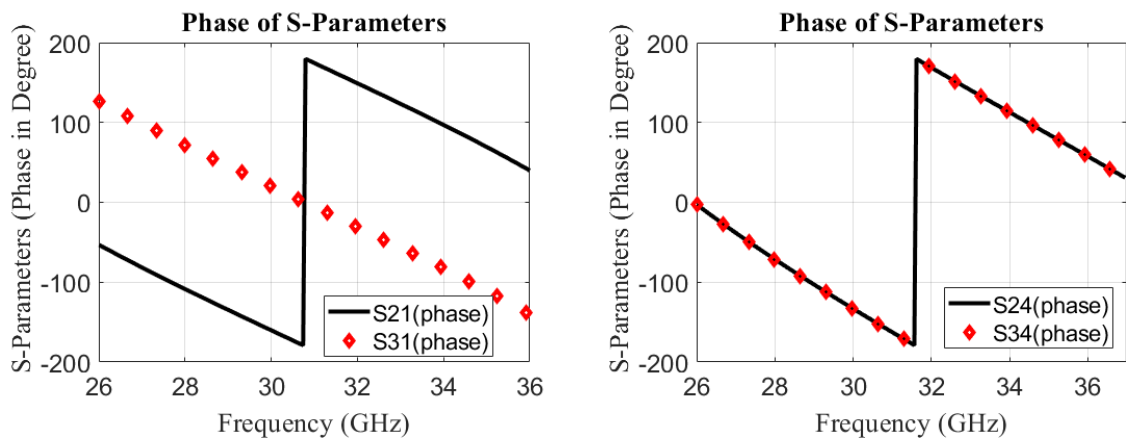


FIGURE 4.30: The phase of magic tee S-parameters.

4.10 Design of Dual Mode RGW

The Q-TEM mode and other modes of RGW are orthogonal. Therefore, there is no coupling between the modes, theoretically. Therefore, the dominant and first higher-order mode can be used for guiding two different signals without interference through the RGW. Using the fundamental mode and the first high order mode on the same waveguide provide many advantages. First, the channel capacity is increased, which helps to improve system performance. Second, a dual pattern antenna is designed with each pattern corresponding to one mode. Third, the number of pins utilized to build RGW can be reduced compared to two parallel lines, which reduces the fabrication cost.

Fig.4.31 shows a dual mode RGW with the magic tee (used for the excitation of the two modes). The outputs ports of the magic tee are designed with total width greater than the wavelength at center frequency. If the magic tee use to feed the RGW directly with same width, the second high order mode TE_{20}^{RGW} can propagate from the beginning of the band. Therefore, a tapered section is used, from the magic tee outputs to the designed ridge line, to have a ridge line width that supports the first two modes only. Moreover, using the tapered section is very important to improve the matching for both modes. By applying the power on Port 4 of the magic tee, the power is equally divided between Port 2 and Port 3 with the same phase as shown in Fig.4.30 (b). Then, those outputs are used to excite the proposed wide RGW. In this case, the magic tee provides excitation to the ridgeline, which imposes a high even symmetry along ridge line. Therefore, only the Q-TEM mode is excited on the ridge and the odd modes are suppressed. Fig.4.32 (a) shows the electric field distribution of the Q-TEM mode that can propagate in this ridge. On the other hand, by applying the power to Port 1 of the magic tee, the power is equally divided between Port 2 and Port 3 with 180° phase shift as illustrated in Fig.4.30 (a). Then, those outputs are used to feed the proposed wide RGW. In this case, the magic tee provides a differential excitation to the ridge line, which imposes a virtual PEC wall in the middle of the ridge. Therefore, only the odd mode is excited on the ridge and the even modes are suppressed. Fig.4.32 (b) shows the electric field distribution of the TE_{10}^{RGW} that can propagate in this

ridge. From the E-field distribution, it is clear that there is only one propagating mode on the ridge with zero tangential electric field in the middle of the ridge and maximum on its sides.

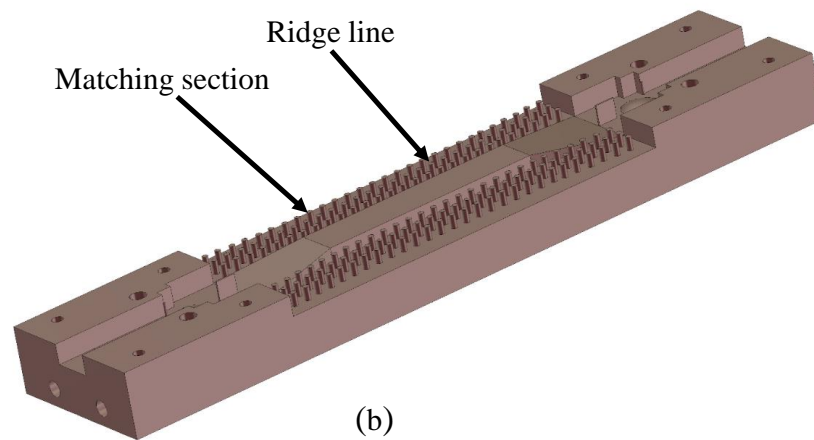
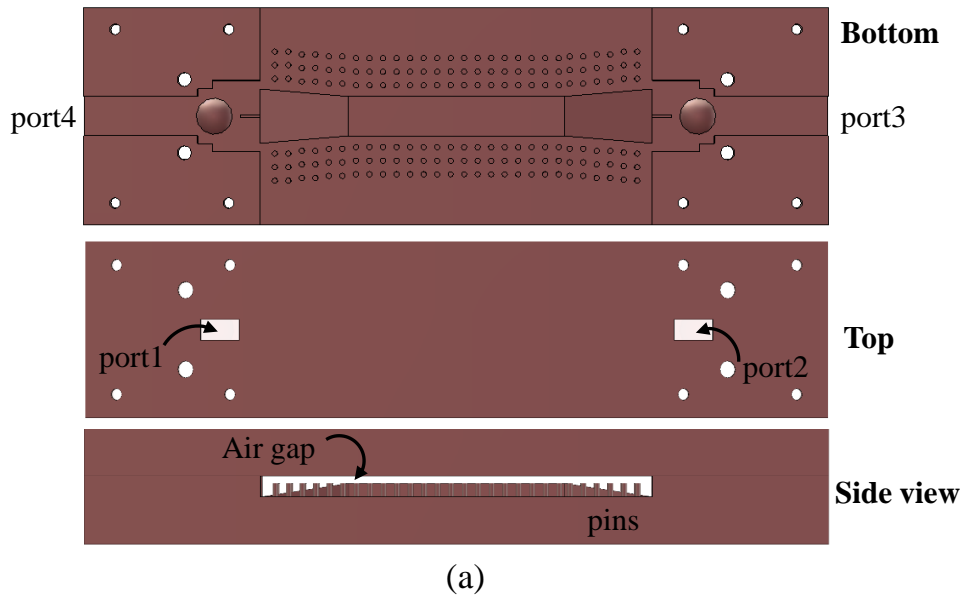


FIGURE 4.31: The geometry of the proposed dual-mode RGW structure. (a) Top and side views. (b) 3D view of the RGW.

The simulation of the proposed design shows good performance in a back-to-back configuration. The simulated S-parameters of the designed dual-mode RGW are depicted in Fig.4.33 (a) where the transmission levels (S_{21} and S_{34}) are ≥ -0.7 dB from 28.7 to 35 GHz whereas the reflection coefficients at Port 1 (S_{11}) and Port 4 (S_{44}) are below -10 dB from 28.77 to 34.61 GHz. Furthermore, the isolation between the two modes is very high

(> 30 dB) at center frequency, as illustrated in Fig.4.33 (b). In the proposed structure, the matching for both modes starts from the same frequency. Therefore, an actual and useful dual-mode RGW is achieved, in which the two modes operate in the same frequency band. The proposed design has attractive performance where the bandwidth is more than 18.5% at 31.5 GHz.

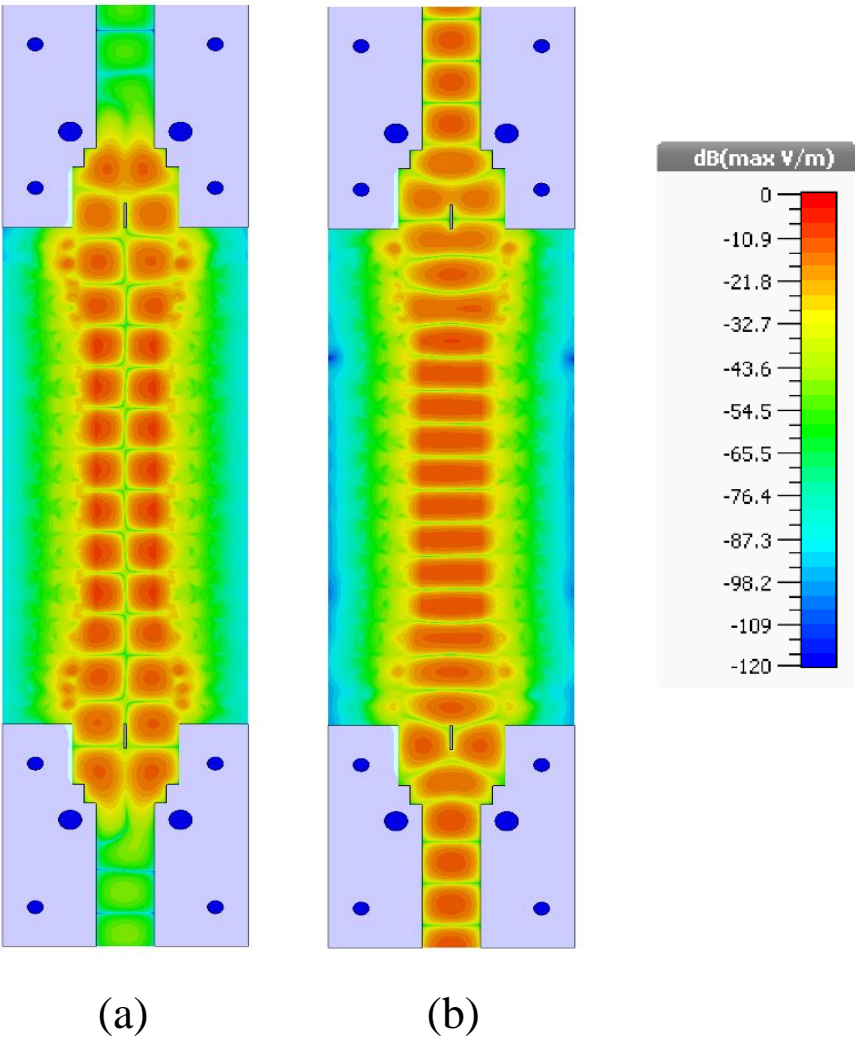


FIGURE 4.32: The field distribution for the proposed RGW dual mode structure. (a) Q-TEM mode. (b) TE_{10}^{RGW} mode.

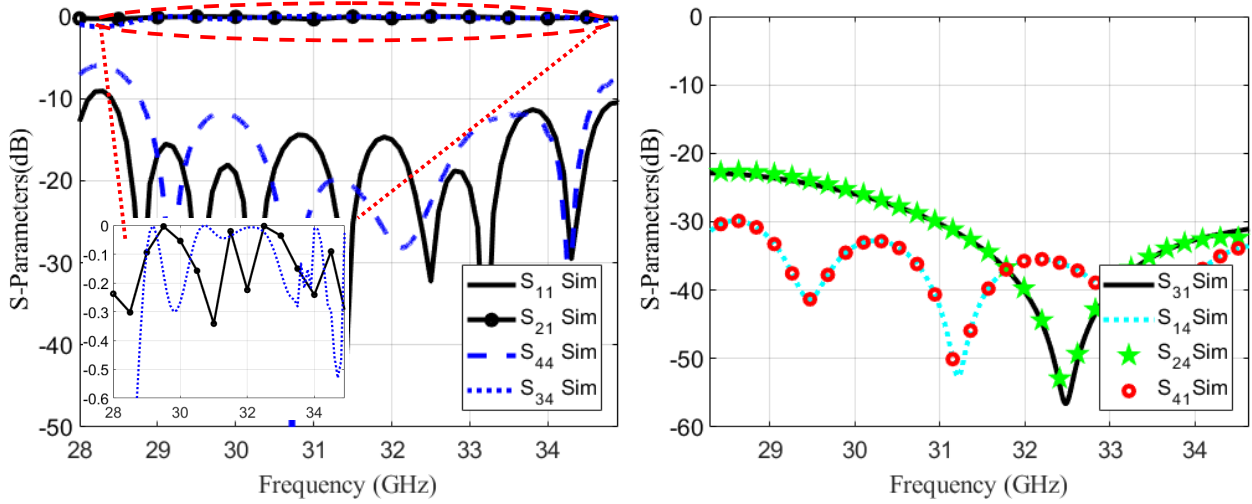


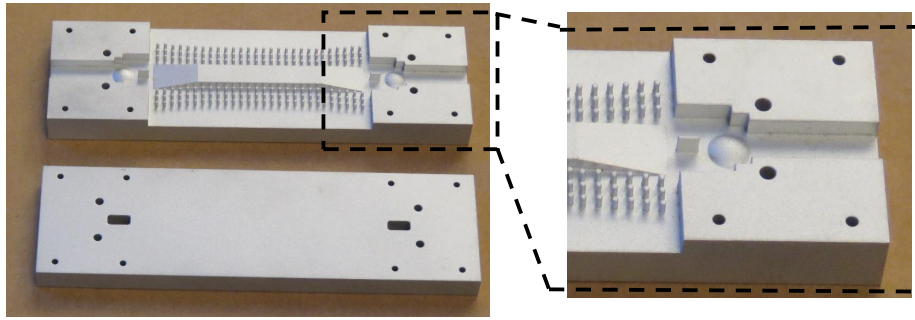
FIGURE 4.33: S-parameters of the proposed RGW dual mode.

4.11 Fabrication and Measurement

To validate the proposed design, a prototype of the whole dual-mode RGW structure is fabricated as displayed in Fig.4.34. Top and bottom parts are manufactured separately, then they are joined together by screws. The technology used for the fabrication of this structure is the CNC technology. According to the machine used, the fabricated dimensions tolerance is ± 0.001 mm, and all corners in the proposed structure are formed by the smallest possible milling tool.

The fabricated structure is measured using two WR-28 waveguide and two matching terminations. Fig.4.35 shows the measurement setup of the proposed design. The simulated and measured S-parameters of the proposed dual-mode RGW are compared to each other as shown in Fig.4.36. It is clear that there is a good agreement between simulated and measured results, where the transmission coefficient (S_{21} and S_{34}) are about -0.42 dB from 29 to 34.5 GHz with a variation of ± 0.25 dB. The reflection coefficients at Port 1 (S_{11}) and at Port 4 (S_{44}) are below -10 dB over the operating band. Furthermore, the isolation between the two modes is very high, as illustrated in Fig.4.37 .

A comparison between previous related works and this work is listed in Table 5.2 .



(a)



(b)

FIGURE 4.34: The fabricated dual-mode RGW structure (a) individually parts. (b) Assembled parts.

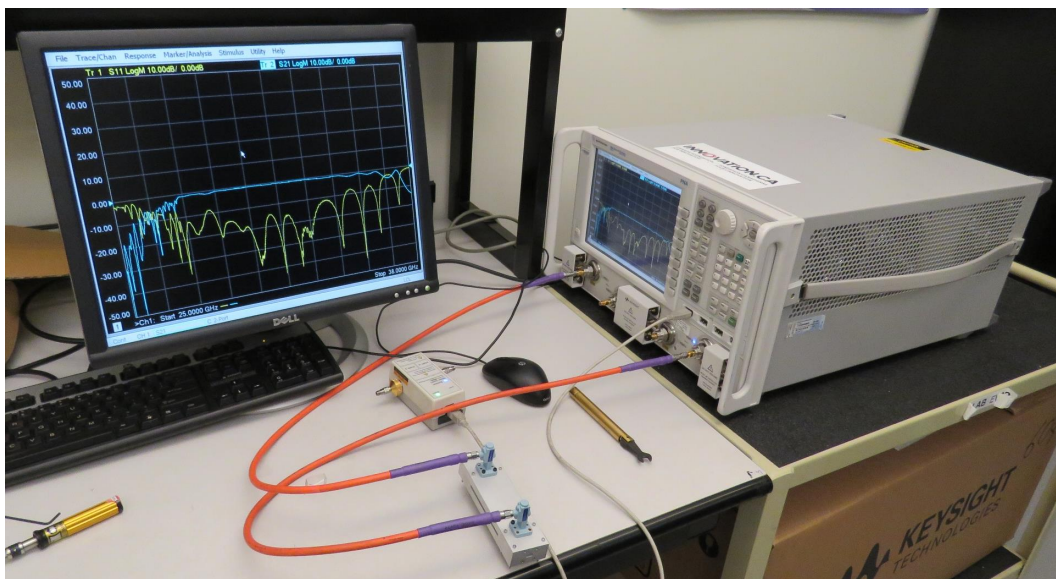


FIGURE 4.35: Dual-mode RGW measurements setup.

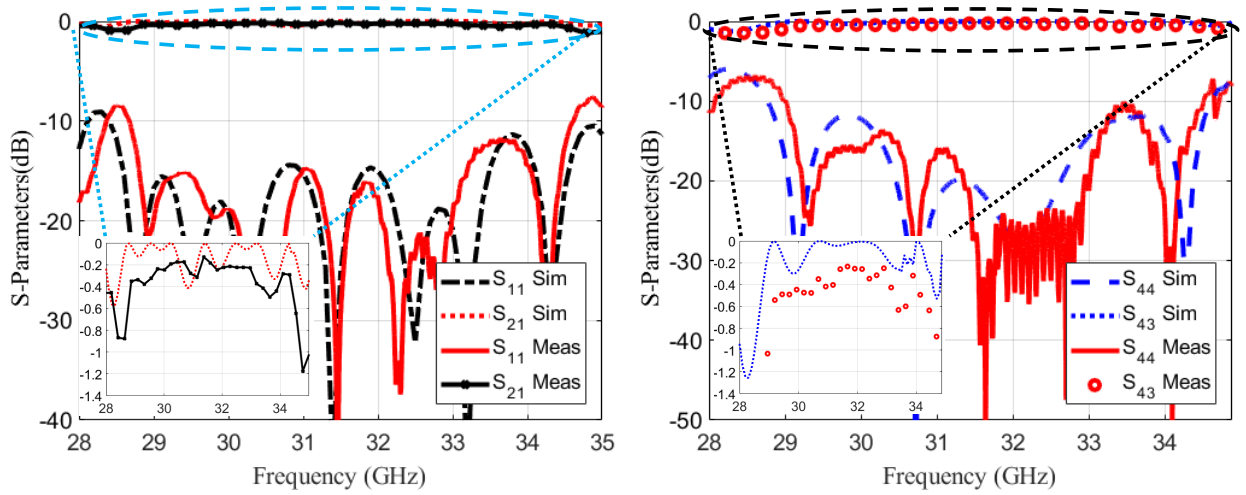


FIGURE 4.36: Dual-Mode RGW results using back-to-back setup. (a) Measurements and simulations obtained from port1 and port2. (b) Measurements and simulations obtained from port3 and port4.

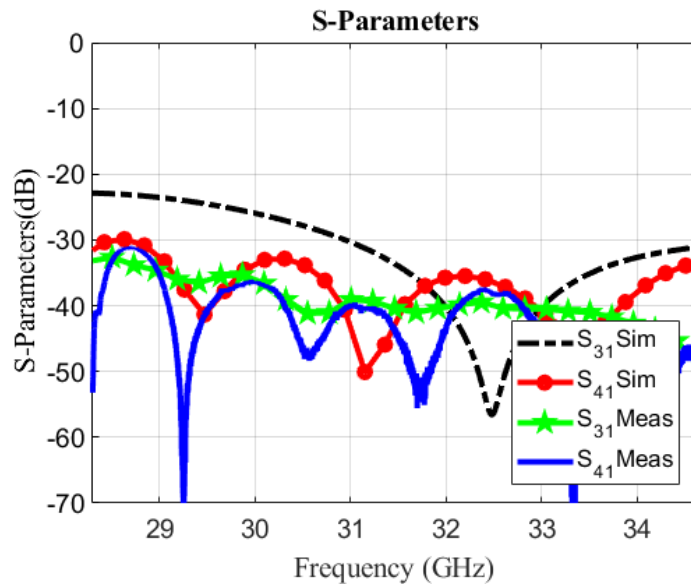


FIGURE 4.37: Measurements and simulations the Isolation of proposed dual-Mode RGW. .

As indicated, this work has benefits compared to other listed works. The proposed dual-mode RGW takes the advantages of wide impedance bandwidth, high isolation level between the propagating modes, and low insertion loss for both modes compared with the listed works. In [57], an OMT is designed to carry two orthogonal modes (TE₁₀ and TE₀₁ modes) using a square waveguide. Yet, the device is bulky and difficult to fabricate at

TABLE 4.6: Comparison with previously related works

Ref	Technology	Freq (GHz)	Modes / pol	Bandwidth (dB)	Insertion loss	Isolation (dB)
[13]	SIW	9.8 13.24	TE ₁₀ ,TE ₂₀ Single pola	17.3%(TE ₁₀) 7.9%(TE ₂₀)	-	>30
[57]	RWG	19	TE ₁₀ ,TE ₀₁ Dual pol	15.7%	-1	>30
[59]	Microstrip and WG	30	TE ₁₀ ,TE ₀₁ Dual pol	6.7%	TE ₁₀ (-2.2 to -3) TE ₂₀ (-1.2 to -2)	>30
This work	RGW	31	Q-TEM,TE ₁₀ Single pol	18.7%	TE_{10}^{RGW} (-0.14 to -0.7) Q-TEM(-0.2 to -0.6)	>30

high-frequency bands as the dimensions become very small, contrary to the proposed RGW dual-mode, which can be implemented in the printed RGW form. On the other hand, an SIW technology is used to have compact dual-mode waveguide (TE₁₀ and TE₂₀ modes) [13]. However, the two modes operate at different frequencies that does not efficiently use the bandwidth. Moreover, in SIW technology, the wave suffers from dielectric losses as it propagates in a dielectric material. Conversely, the proposed design has superior performance as the RGW has low loss compare with SIW technology since the wave propagates on an air gap.

Chapter 5

Antennas Design Based on Odd Mode of Ridge Gap Waveguide

5.1 4x4-element Cavity Slot Antenna Differentially-fed by Odd Mode Ridge Gap Waveguide

In this section, a differential feeding, based on the first higher-order mode (TE_{10}^{RGW}) of the ridge gap waveguide (RGW), for a cavity slot antenna is presented. This feeding is based on a simple mechanism rather than the conventional complex networks that suffer from high losses. It is based on exciting the first higher-order mode TE_{10}^{RGW} of the ridge gap waveguide (RGW) by expanding the ridge width. This expansion would excite some undesired even modes that are suppressed by embedding a vertical perfectly electric conducting (PEC) wall in the middle of the waveguide based on the concept of magic tee operation. The proposed 4x4 cavity slot antenna is realized using substrate integrated waveguide (SIW) technology. Two horizontal slots on the top of proposed wide RGW, representing the differential feeding approach, are etched to feed the cavity slot antenna. The slots couple the fields with the same amplitudes and 180° phase difference to the cavity. The electric fields of the two coupling slots have odd symmetry in the x-axis and subsequently, uniform electric field distribution of the TE_{440} mode of a cavity can be excited. The 4/4 radiating slots are etched on the top of the cavity in a specific distribution

to ensure having in-phase fields for broadside radiation with low cross-polarization levels. The simulation and measurement results of the cavity slot antenna are in good agreement. The results confirm that the proposed cavity antenna achieves a relative bandwidth of 7.1% for -10 dB return loss, a gain of about 16.5 dBi and side lobe level about -17 dB in E-plane and -13.8 dB in H-plane. Furthermore, the proposed antenna provides low cross-polarization levels (-35 dB in E-plane and -27 dB in H-plane) within the operating frequency band of 32.5 GHz to 34.9 GHz. With this achieved a high gain and high efficiency of the proposed antenna, it may have a great potential for millimeter-wave (mm-wave) applications. Up to the authors' knowledge, this proposed TE_{10}^{RGW} -mode RGW and its use as a differential feeding is presented for the first time in literature.

5.1.1 Antenna Design

Generally, microwave resonator builds from a closed waveguide, where called waveguide resonators. They are commonly short-circuited at ends to form a closed cavity. The energy stores in the cavity where a part of the power is wasted in the metallic walls and in the dielectric that might use to fill the cavity [4]. A cavity resonator usually feeds by coaxial probe or slot. The location of the feeding probe or slot plays an essential role to define the resonant modes of the cavity, based on the field changes along the three dimensions of the cavity. Starting the design with the same analysis of a rectangular cavity, The resonant frequency of TE_{mnl} mode can be stated as follows [4]:

$$f_{mnl} = \frac{c}{2\pi\sqrt{\mu_r\epsilon_r}} \sqrt{\left(\frac{m\pi}{a}\right)^2 + \left(\frac{n\pi}{b}\right)^2 + \left(\frac{l\pi}{d}\right)^2} \quad (5.1)$$

where m, n, l is are integer number indicate the variation of wave in x,y,z direction, respectively.

In our design, since we interest to design 4x4 SIW cavity antenna, 4x4 standing waves uniformly distributed in the cavity should be generated which demonstrates that the resonant mode is TE₄₄₀ mode. By using resonant frequency equation we can calculate all the cavity dimensions.

Fig.5.1 displays the E-field and H-field distribution inside a square waveguide cavity which is fed using two horizontal slots. From Fig.5.1 (b), it is clear that there are 4×4 standing waves uniformly distributed in the cavity which shows that the excited mode is TE₄₄₀. Therefore, it is possible to excite this mode by using two horizontal slots as differential feeding in both sides of the cavity center as shown in Fig.5.1 (a) (dotted black slot).

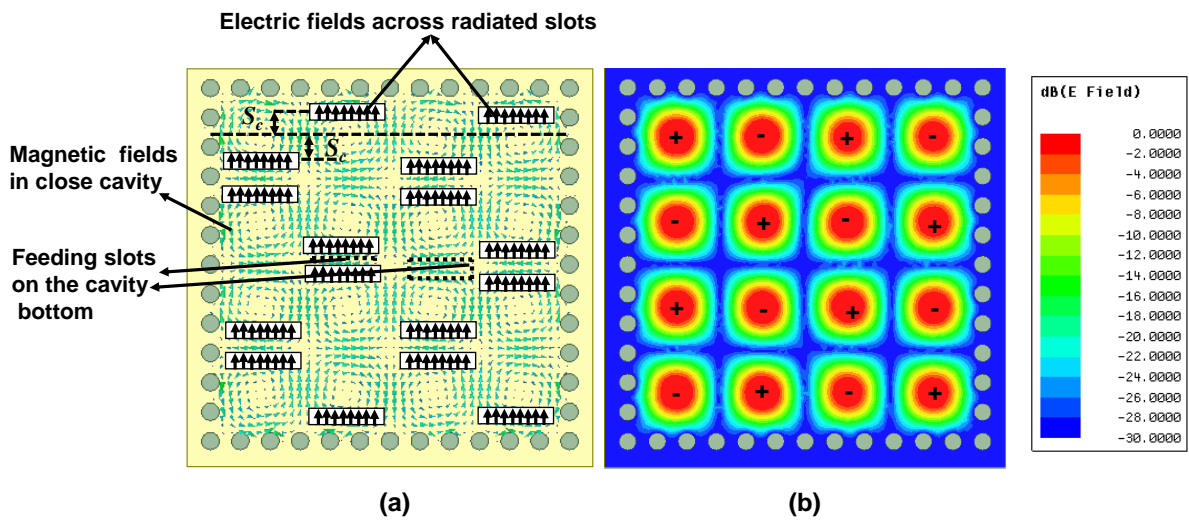


FIGURE 5.1: Magnetic and electric fields distribution of TE₄₄₀ mode in square waveguide cavity. (a) The electric field in square waveguide cavity. (b) The magnetic field in the cavity and Electric field across the slots.

5.1.2 4×4 Cavity Slot Antenna with Differential RGW Feeding

Fig.5.2 shows the configuration of the proposed cavity antenna and its feeding structure. An SIW cavity antenna is designed and excited by the RGW odd mode as a differential feeding technique to excite the TE₄₄₀ mode inside the cavity. This antenna is designed using Rogers 5880 ($\epsilon_r = 2.2, \tan\sigma = 0.002$) substrate with a thickness $hc = 1.58\text{mm}$. As shown in Fig.5.2 (a), the cavity walls built by metallic vias, which are used to form the square cavity.

Based on the fields distribution inside the cavity, sixteen slots can be etched in phase on the top of the cavity as shown in Fig.5.2 (a) where 4×4 standing waves are uniformly distributed in the cavity. As shown in Fig.5.1 (a), the slots distribute with equal shift

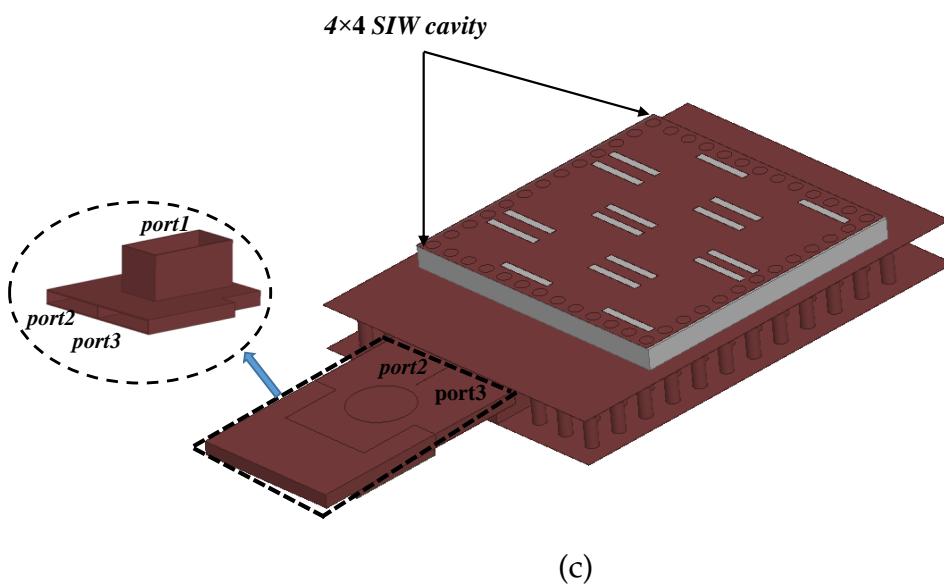
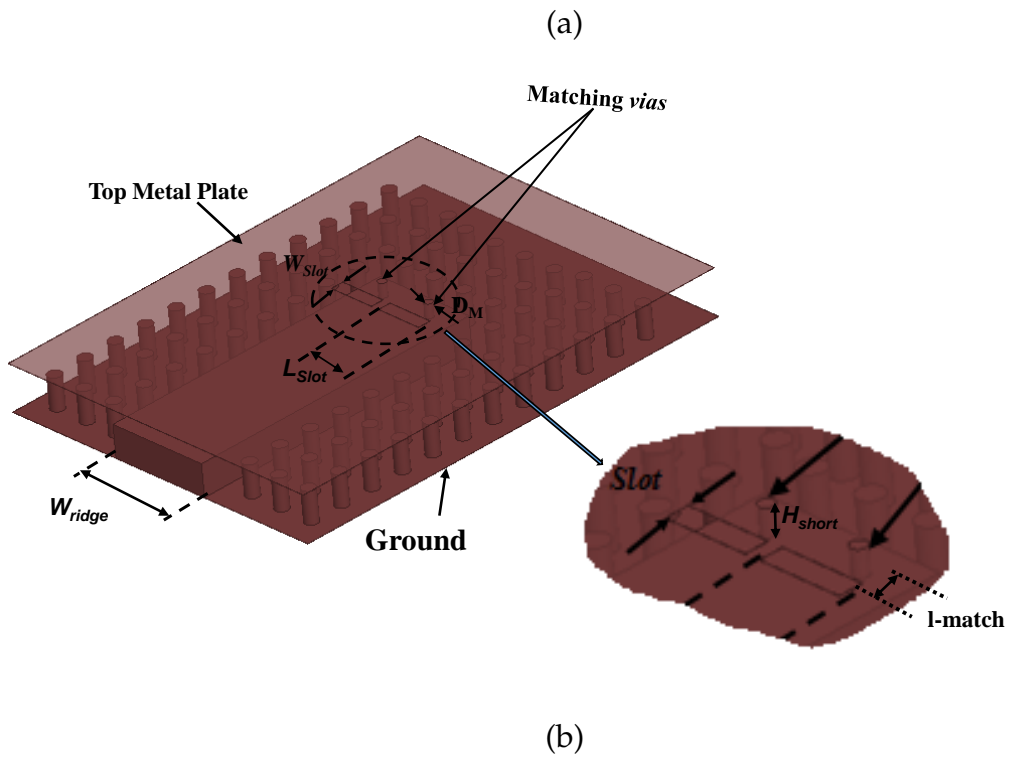
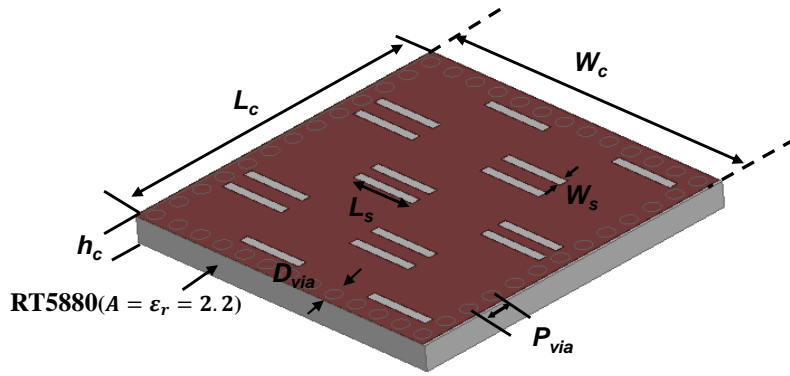


FIGURE 5.2: The geometry of the proposed cavity antenna structure. (a) 3D view of the SIW cavity. (b) Cavity excitation structure. (c) Whole cavity slot antenna structure.

TABLE 5.1: Dimensions of the proposed antenna

Parameter	W_{ridge}	L_{slot}	W_{slot}	D_{via}	h_c	P_{via}
Value(mm)	7.5	3.3	1.1	1	1.58	1.7
Parameter	$W_c = L_c$	l_{match}	W_s	L_s	D_M	H_{short}
Value(mm)	19.8	2.5	0.6	4.4	0.27	1

distance ($S_c=1.4\text{mm}$) from the dotted line. The electric field across the slots is shown in Fig.5.1 (a), where the black arrows describe the orientation of the electric field. Since all the slots are etched in phase, all the sixteen slots of the antenna radiate in phase. The cavity antenna is excited by the structure shown in Fig.5.2 (b). All the dimensions of the proposed structure are listed in Table 5.1.

The whole structure of the 4×4 cavity slot antenna is shown in Fig.5.2 (c). The field propagates from the magic tee ports along with the wide RGW structure and couples to the cavity through the two horizontal slots that are etched on top of the RGW. In order to improve the impedance matching, two vias with a radius of D_M and a height of H_{short} are placed at the centers of the two coupling slots of the RGW.

The simulated results of the reflection coefficient and gain of the proposed cavity antenna are obtained using two full-wave solvers, namely the HFSS and CST. The purpose of this comparison is to provide a solid verification of the results before the fabrication stage.

As shown in Fig.5.3, a very good agreement between the results is obtained. The fractional bandwidth is about 7.1% with a center frequency of 33.5 GHz. The simulated gain is about 16.5 dBi over the bandwidth.

5.1.3 Parametric Study

A parametric study has been carried out to show the effect of the most critical dimensions on the proposed antenna performance, in terms of the gain and the reflection coefficient. The length of slot that etched on the top plate of RGW to feed the cavity (L_{slot}), matching pin position (l_{match}), substrate thickness (h_c), and cavity slot length and slot center offset

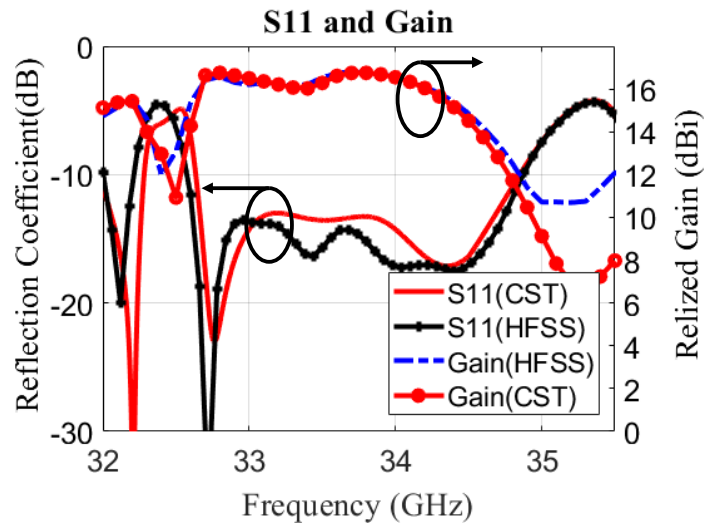


FIGURE 5.3: Comparison of the HFSS and CST simulated reflection coefficients and gains of the proposed cavity antenna.

(L_s and S_c) are selected for this parametric study. The parametric study can be concluded in followed points:

- The length of the feeding slot (l_{slot}) and matching pin position (l_{match}) have the same effect on the antenna's gain and matching performances, where increasing any one of them improves the gain and the matching until it reaches the optimum value. Then, the performance degrades again when moving away from the optimum value. This is illustrated in Fig.5.4 where the gain and reflection coefficient with different values of the l_{match} and l_{slot} are presented. The optimum value of l_{match} and l_{slot} are 2.5 mm and 3.3 mm respectively. The gain drops more than 1.5 dBi when moving away from the optimum values.
- The parametric study carry outed on cavity parameters h_c , and l_s , shows a shift on the resonance frequency toward lower frequencies when increasing any of them. This is depicted in Fig.5.5 (a), (c) where the gain and reflection coefficient for different values of h_c and l_s is presented. The optimum values of h_c and l_s are 1.58 mm and 4.4 mm respectively. Also, there is a gain drop and degradation on the matching away from the optimum values.

- Varying Sc has a slight impact on the peak gain and the reflection coefficient as displayed in Fig.5.5 (b). There is a drop in the gain at high frequencies for high values of Sc where the slots reach the edge of the cavity. The optimum value of Sc is 1.4 mm.

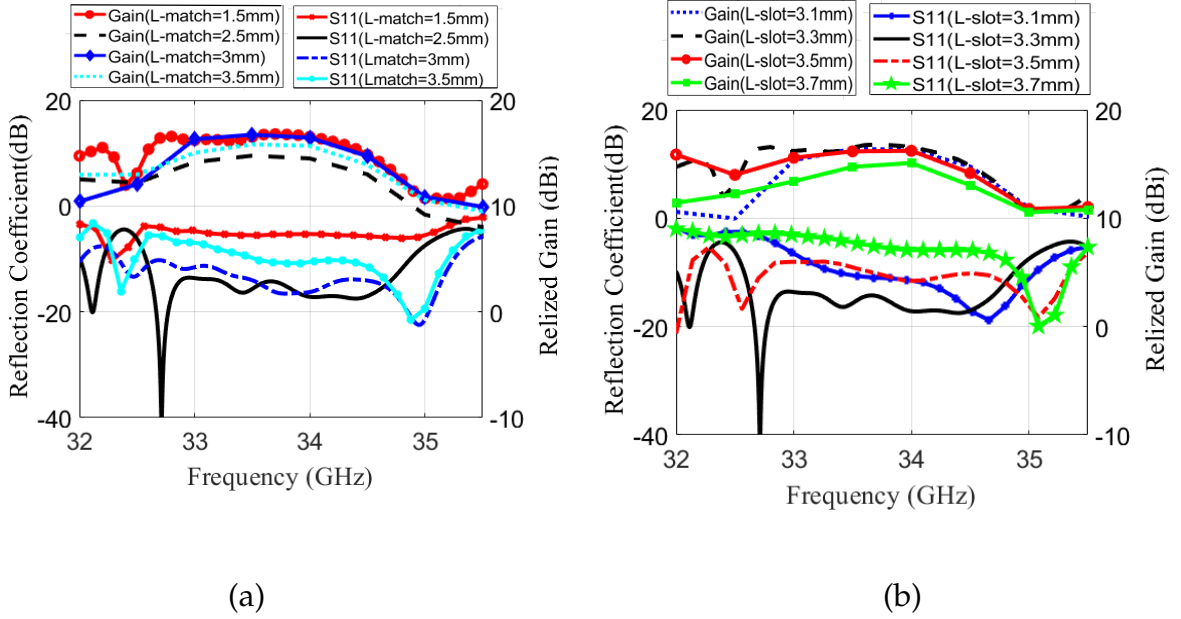
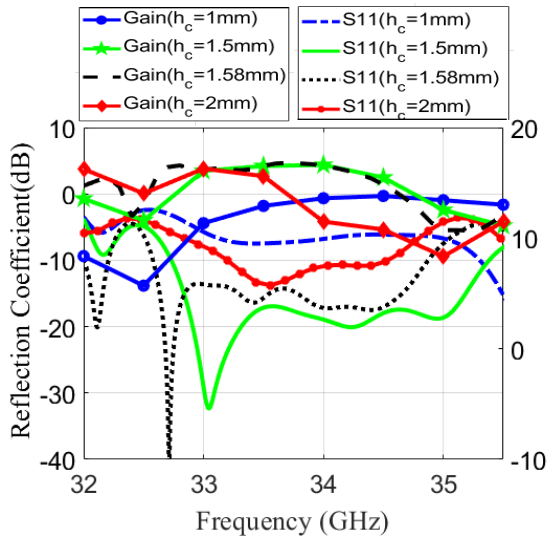


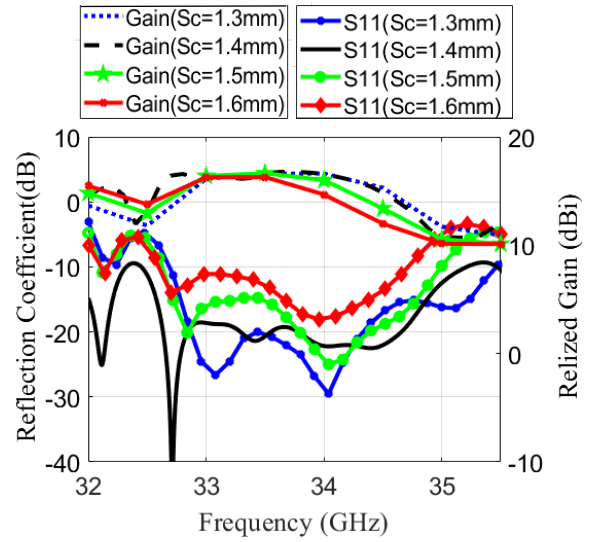
FIGURE 5.4: Simulated reflection coefficients and gain of the proposed antenna considering the impact of varying different geometric parameters of cavity feeding: (a) l_{match} ; (b) l_{slot} .

5.1.4 3D Printing Implementation and Measurements

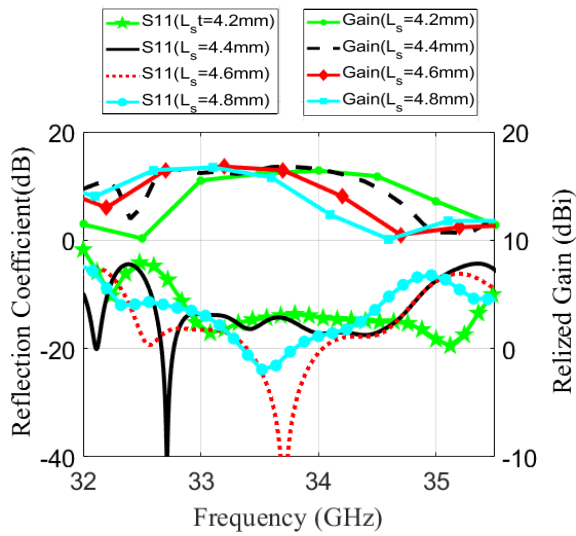
To test the proposed design, a prototype of the cavity slot antenna with differential feeding is fabricated and measured. Fig.5.6 (a,b) show the individual part and assembled parts. The feeding part, the SIW cavity antenna, and the transition are fabricated individually, then they are combined by screws. The standard WR-28 waveguide is used to excite the antenna at the Ka-band. The technology utilized for the implementation of this structure is the three-dimensional printing of plastic material, then the structure is plated with copper. In the measurement setup, the antenna is mounted on the fixture as shown in Fig.5.7. The reflection coefficient of the antenna is measured by the Agilent



(a)



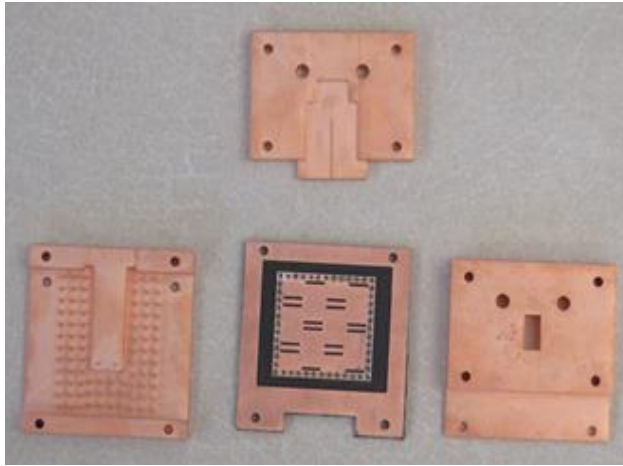
(b)



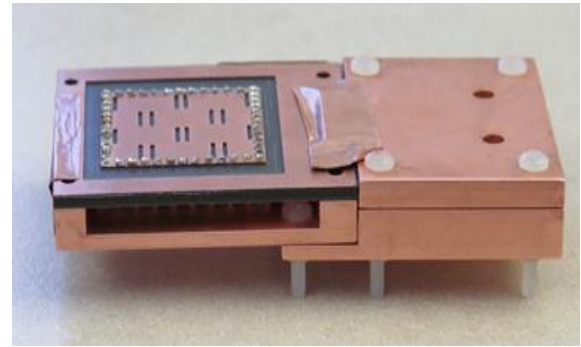
(c)

FIGURE 5.5: Simulated reflection coefficients and gain of the proposed antenna considering the impact of varying different geometric parameters of the cavity: (a) h_c ; (b) Sc ; (c) L_s .

N52271A network analyzer while the antenna radiation pattern and gain are measured in the antenna anechoic chamber by NSI far-field measurement system.



(a)



(b)

FIGURE 5.6: The fabricated 4 x 4 cavity antenna (a) individually parts. (b) Assembled parts.

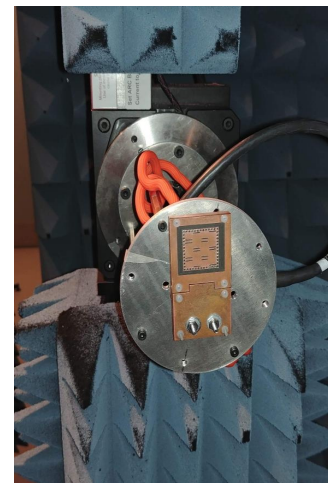


FIGURE 5.7: Photos of the measurement set up.

- **Gain and Reflection Coefficient**

The measured and simulated results of the reflection coefficient and gain of the proposed antenna are compared to each other as shown in Fig.5.8. There is a good

agreement between simulation and measurement results. The measured fractional bandwidth of the structure is 8.3% (from 32.5 GHz to 35.3 GHz). The measured and simulated gains of the proposed antenna are also shown in Fig.5.8 where both of them are around 16.5 dBi in the operating bandwidth. The slight difference between the simulated and measured results is due to the effect of the manufacturing accuracy.

- **Radiation Pattern**

The measured and simulated H-plane and E-plane radiation patterns of the proposed cavity antenna are depicted in Fig.5.9. The results are in good agreement in both H- and E-planes. The sidelobe levels of E-plane and H-plane patterns at 33.5 GHz are -17 dB and -13.8 dB, respectively. Since the cavity has symmetric shape and excited by differential feeding, the radiation patterns of the cavity are mainly symmetric, especially in H-plane. The results show that the cross-polarization level is below -35 dB and -27 dB in the E-plane and H-plane, respectively, across the whole the operating bandwidth.

A comparison among related reported works and this work is listed in Table 5.2. Using the second-order mode as a differential feeding for the cavity slot antenna presented in this work has some advantages compared to other antennas listed in the table. The proposed cavity has a superior radiation performance which has low cross-polarization level, relatively higher gain, low sidelobe level, symmetrical radiation pattern, and good aperture efficiency. Moreover, the matching bandwidth has been enhanced compared to the reported works.

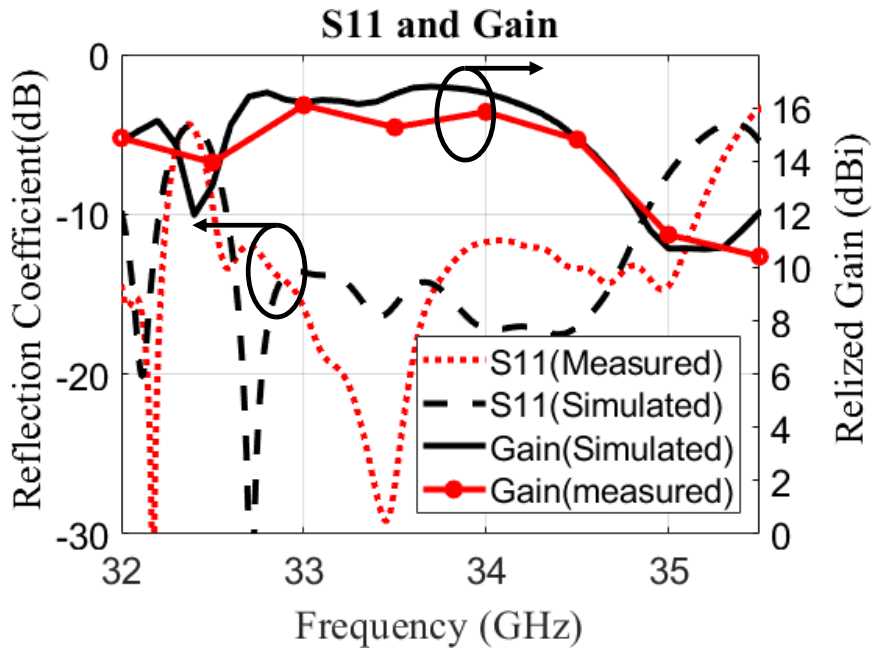


FIGURE 5.8: Comparison of simulated and measured reflection coefficients and gains of the proposed cavity antenna.

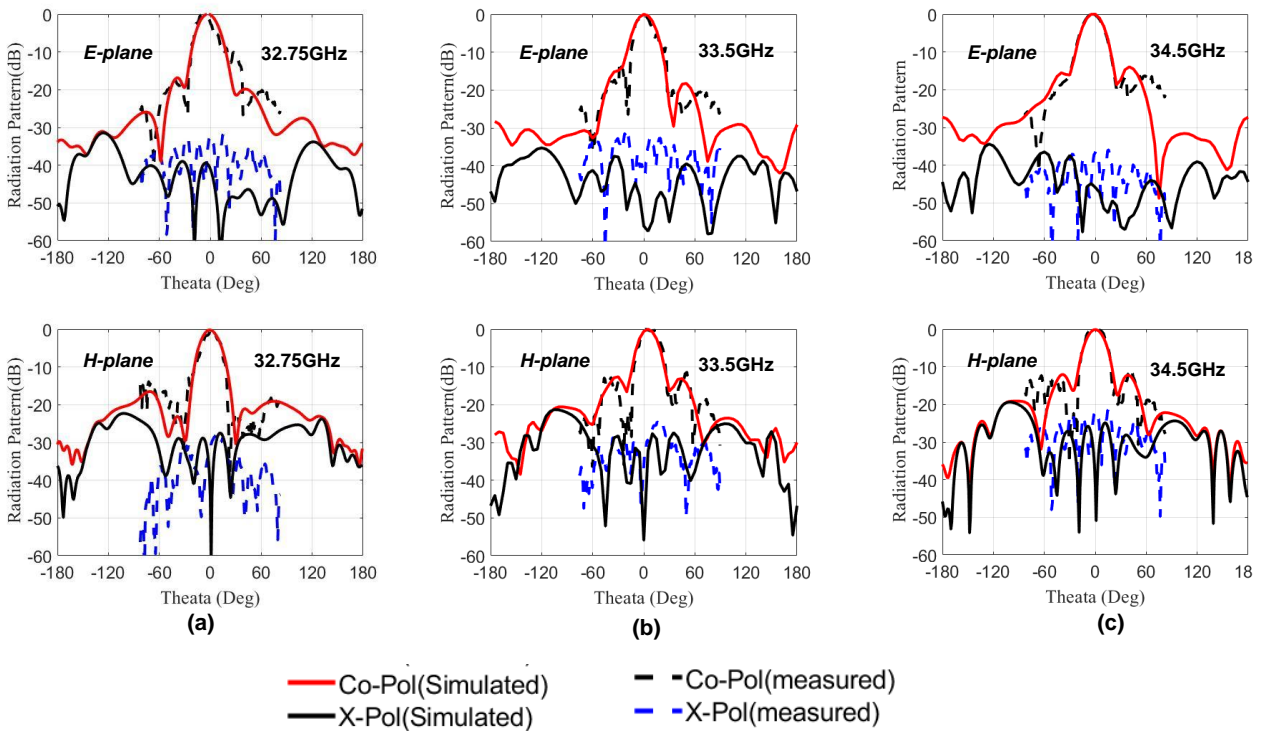


FIGURE 5.9: Measured and Simulated radiation patterns of the proposed cavity antenna. (a) 32.75 GHz. (b) 33.5 GHz. (c) 34.5 GHz.

TABLE 5.2: Comparison with previously related works

Ref	Freq GHz	Feeding Type	Size (λ_0)	Elements	Gain (dBi)	BW (-10dB)	Aperture Efficiency	X-pol Level E and H plane
Ref[13]	5.8	Coaxial probe	$1.6\lambda_0 \times 1.6\lambda_0 \times 0.029\lambda_0$	3×3	13.6	4.7%	71%	N.A
Ref[14]	28	Coaxial probe	$2.16\lambda_0 \times 2.16\lambda_0 \times 0.17\lambda_0$	4×4	16	4.6%	83%	-23dB
Ref[15]	5.8	Coaxial probe	$2.1\lambda_0 \times 2.1\lambda_0 \times 0.125\lambda_0$	4×4	15.2	3.4%	43%	-24dB
Ref[25]	35.25	SIW	$5.83\lambda_0 \times 5.83\lambda_0 \times 0.18\lambda_0$	8×8	24.4	2.8%	65%	-30dB
Ref[26]	60	SIW	$6.8\lambda_0 \times 4.95\lambda_0 \times 0.17\lambda_0$	6×8	21.6	1.8%	34.2%	-20dB
Ref[27]	35	SIW	$4\lambda_0 \times 4\lambda_0 \times 0.3\lambda_0$	8×8	19.98	5.1%	47%	N.A
Ref[28]	10	SIW	$1.03\lambda_0 \times 1.01\lambda_0 \times 0.05\lambda_0$	2×2	9.6	5.5%	69.8%	N.A
This work	33.5	RGW	$2.22\lambda_0 \times 2.22\lambda_0 \times 0.17\lambda_0$	4×4	16.5	7.1%	72.8%	-35dB and -27dB

5.2 Frequency Beam-Scanning Antenna Array Using First Higher Order Mode Ridge Gap Waveguide

Here we introduce the design of a frequency scanning antenna (FSA) based on the first higher order mode ridge gap waveguide (RGW) technology. This FSA is designed so that it can be used with the proposed Y-junction to build a 1x2 FSA array. Below we explain the steps we followed to design an RGW-FSA based on odd mode.

5.2.1 Single-Element Frequency Beam Scanning Antenna

This section describes the design of a single-element frequency scanning slot antenna (FSA), based on exciting the first higher-order mode TE_{10}^{RGW} RGW mode and suppressing the fundamental mode Q-TEM modes. The single FSA is excited by a wide ridge gap waveguide that carries an odd mode, as shown in Fig.4.6. This antenna is designed to work in the 28-32 GHz frequency band. Fig.5.10 shows the configuration of the single-element FSA in which slots are etched in the top plate of the RGW. The behavior of the first higher-order mode field is 180° out of phase and is of equal magnitude, as shown in Fig.4.6. This notable behavior can be exploited to design an FSA. The slots are positioned based on the electric field distribution of the odd mode of an RGW. Therefore, the slots are etched alternatively on the sides of the wide ridge center, carrying the odd mode with less than $\lambda/2$ separation. The slot widths are gradually increased to equally distribute the

power among all radiation slots. Thirteen rectangular slots were etched in the top plate of the metal ridge gap waveguide to achieve the desired radiation pattern. The proposed FSA structure is designed by using commercial software (HFSS) in which the wave ports are used to excite both sides of the proposed antenna. The phase constant varies as the frequency varies, which allows the main beam to be scanned. The slot length design is determined to be 4mm, which is almost equal to half of the wavelength in the RGW.

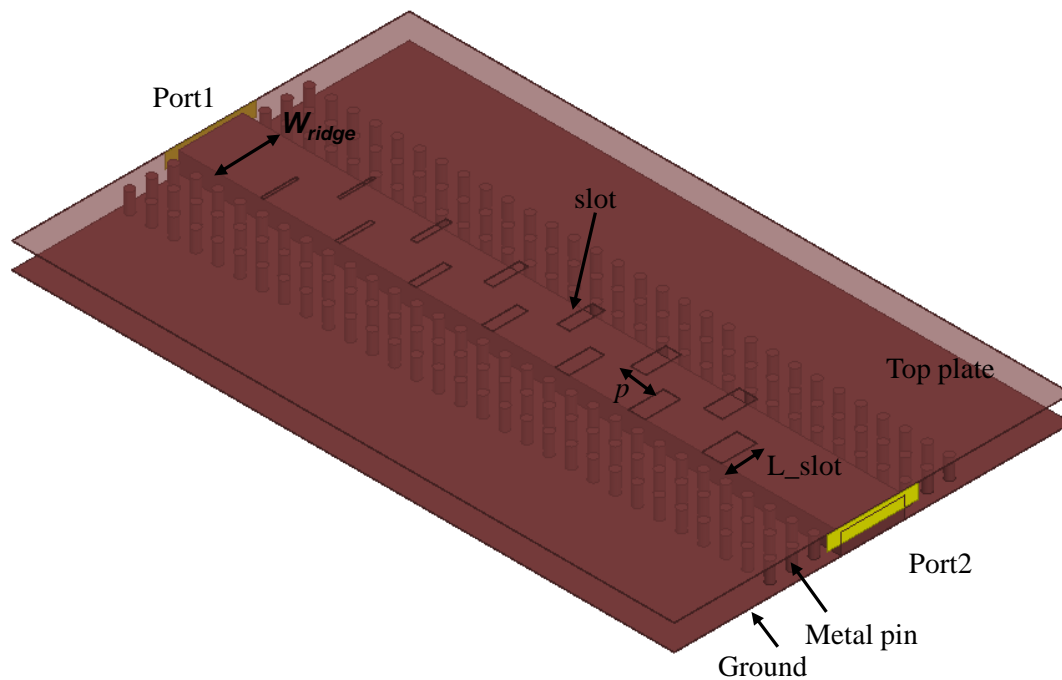


FIGURE 5.10: The configuration of an element of the FSA.

The simulated results of the S-parameters (S11 and S21) of the designed FSA are shown in Fig.5.11, where the antenna works appropriately over the 28-32 GHz range. Fig.5.12 shows the realized gain of the E-plane radiation pattern of all frequencies of the operating bandwidth. The simulated peak gain of the single element antenna is 15.5 dBi with about 1.5 dBi variation, and the beam scanning range is from -32° to -11° . A variation of antenna gain of about 4dBi can be exchanged in order to achieve a wider beam scanning range of from -40° to -11° over the operating bandwidth, while keeping an acceptable side lobe level.

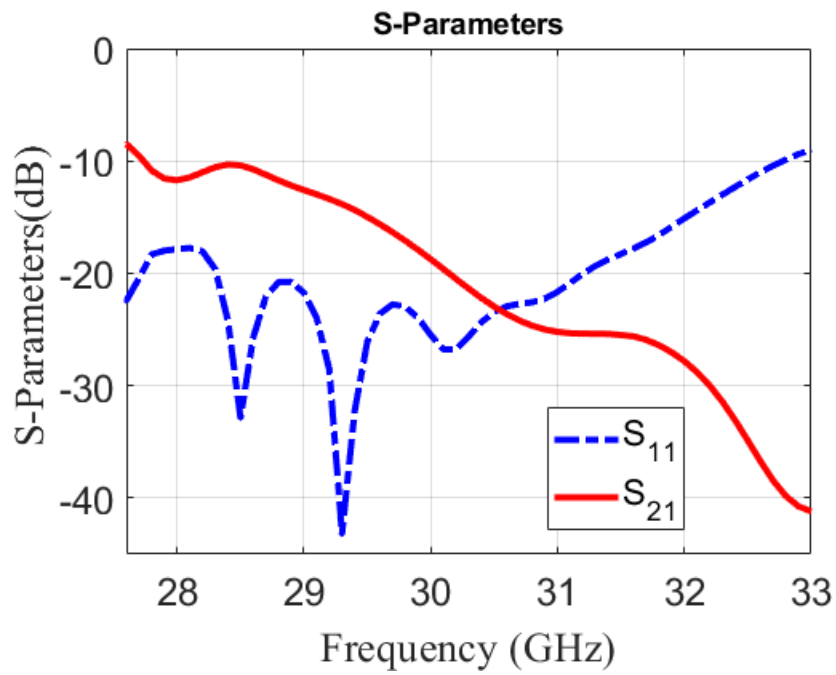


FIGURE 5.11: Simulated reflection and transmission coefficients of the single-element FSA.

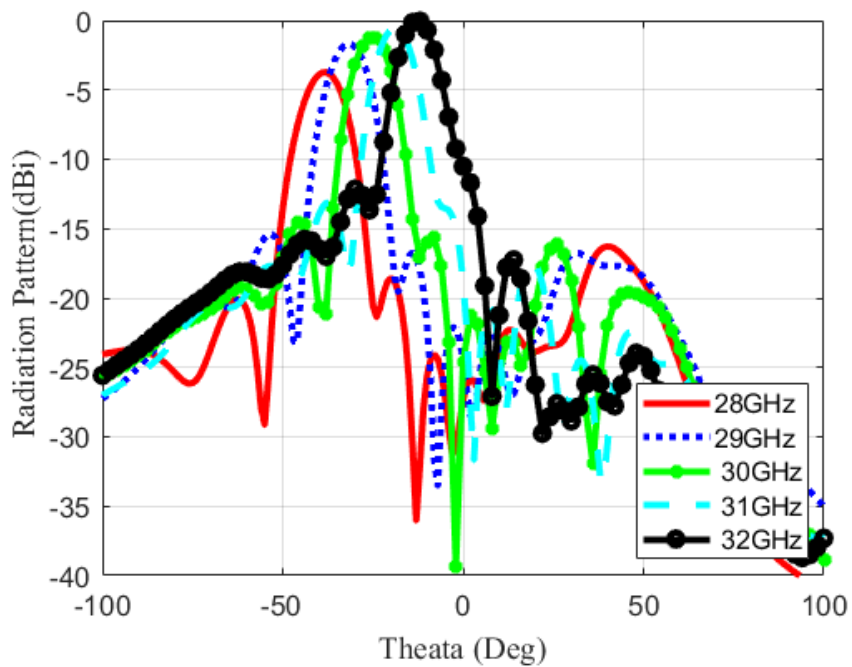


FIGURE 5.12: Simulated realized gain of the E-plane radiation pattern for 28,29,30,31 and 32 GHz.

5.2.2 Two-Element Frequency Beam Scanning Antenna.

In this section, the proposed Y-junction introduced in Chapter 4 is used to build a linear array of the FSA based on odd mode RGW technology. Both arms of the Y-junction power divider are extended to join FSA subarrays (the single element was introduced in the previous subsection), as depicted in Fig.5.13 (a). The distance between the two sub-arrays is set to be two rows of unit cells to act as the PMC . Commercial software (HFSS) is used to design and simulate the proposed structure. The whole structure of an FSA array with a Y-junction power divider is shown in Fig.5.13.

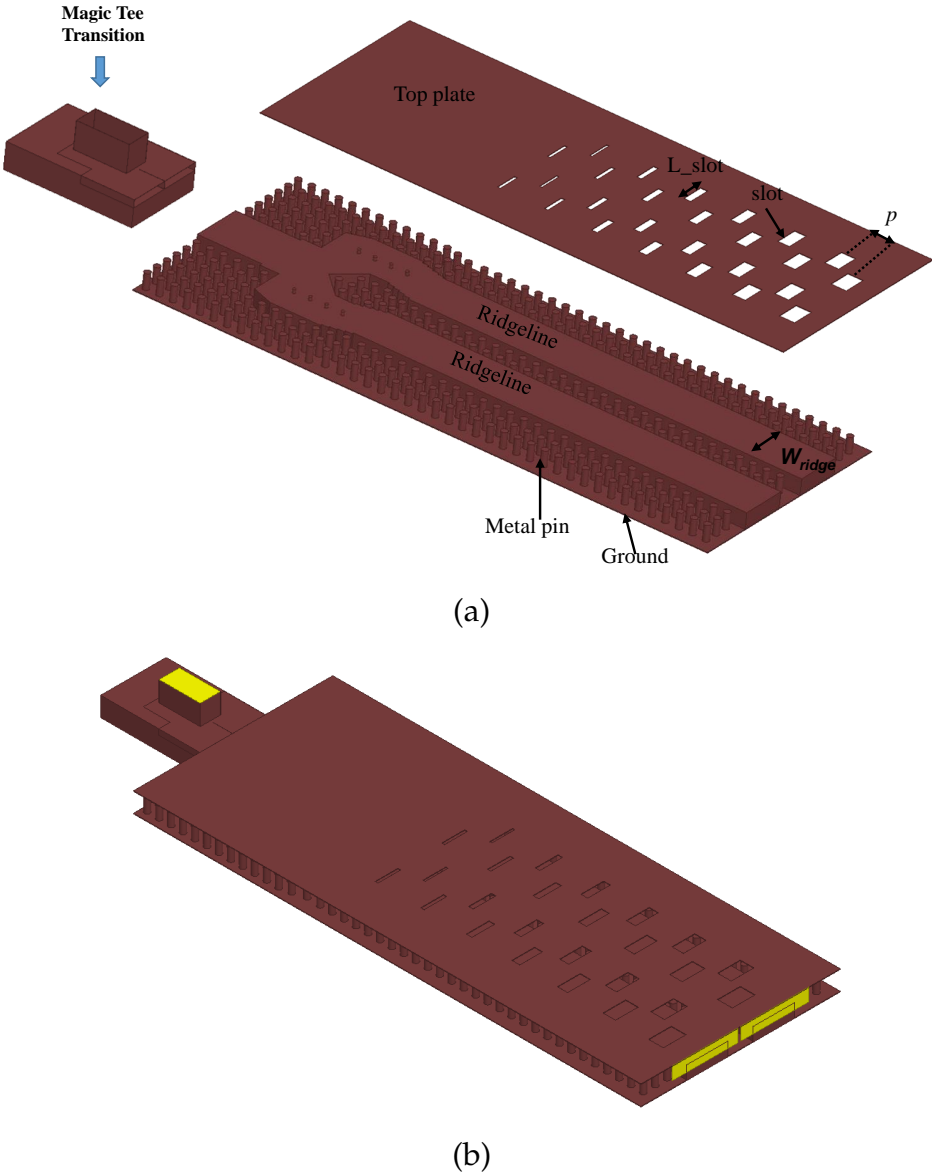


FIGURE 5.13: (a) Separated view of the top, bottom and a magic tee transition; and (b) Complete configuration of the FSA array.

The simulated matching performance of the FSA array is illustrated in Fig.5.14, and remains below -15 dB over the operating bandwidth. Fig.5.15 and Fig 5.17 show polar and 3D radiation patterns, respectively, at frequencies 28, 29,30,31, and 32 GHz. From the radiation pattern results, it is clear that beam scanning continues through the broadside. The electric field distribution inside slots at different frequencies of the proposed design are shown in Fig.5.16. The simulated peak gain of the proposed antenna is 19.15 dBi, and beam scanning range is from -11° to -40° the operating bandwidth, with an acceptable side lobe level.

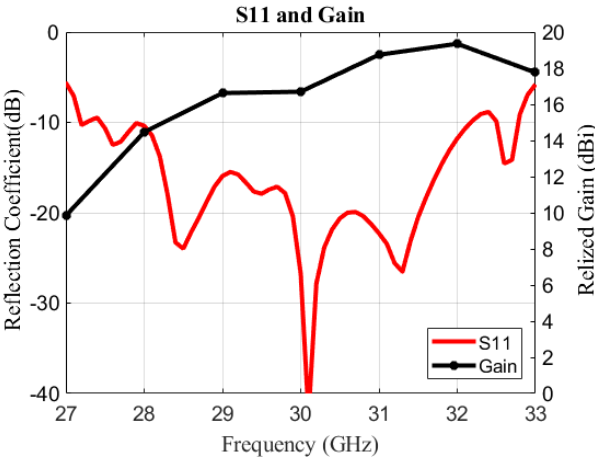


FIGURE 5.14: Simulated reflection and realized gain of the FSA array.

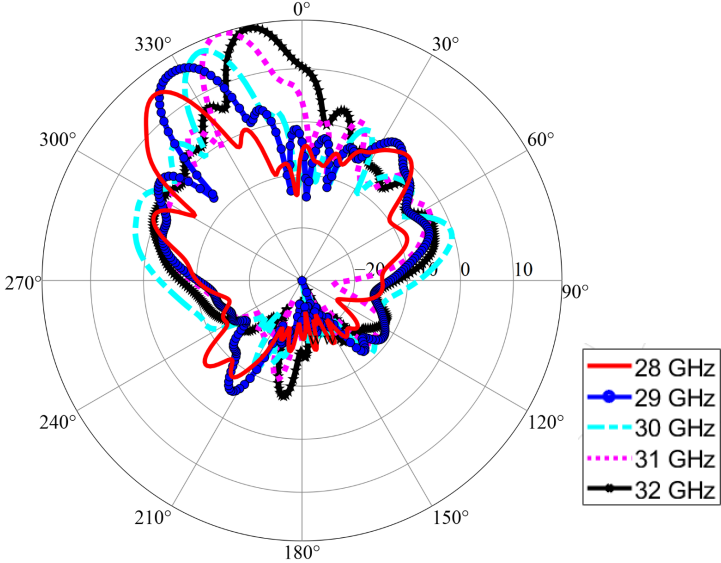


FIGURE 5.15: Simulated realized gain of the E-plane radiation pattern for 28,29,30,31 and 32 GHz.

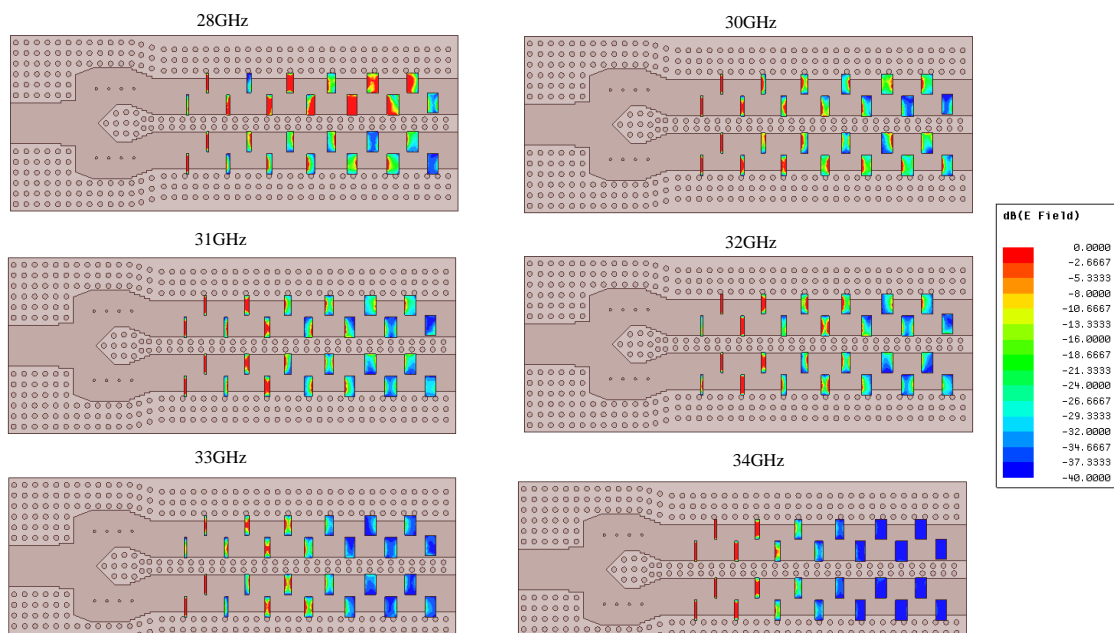


FIGURE 5.16: Simulated E-field distribution in slots for 28, 30, 31,32,33 and 34 GHz.

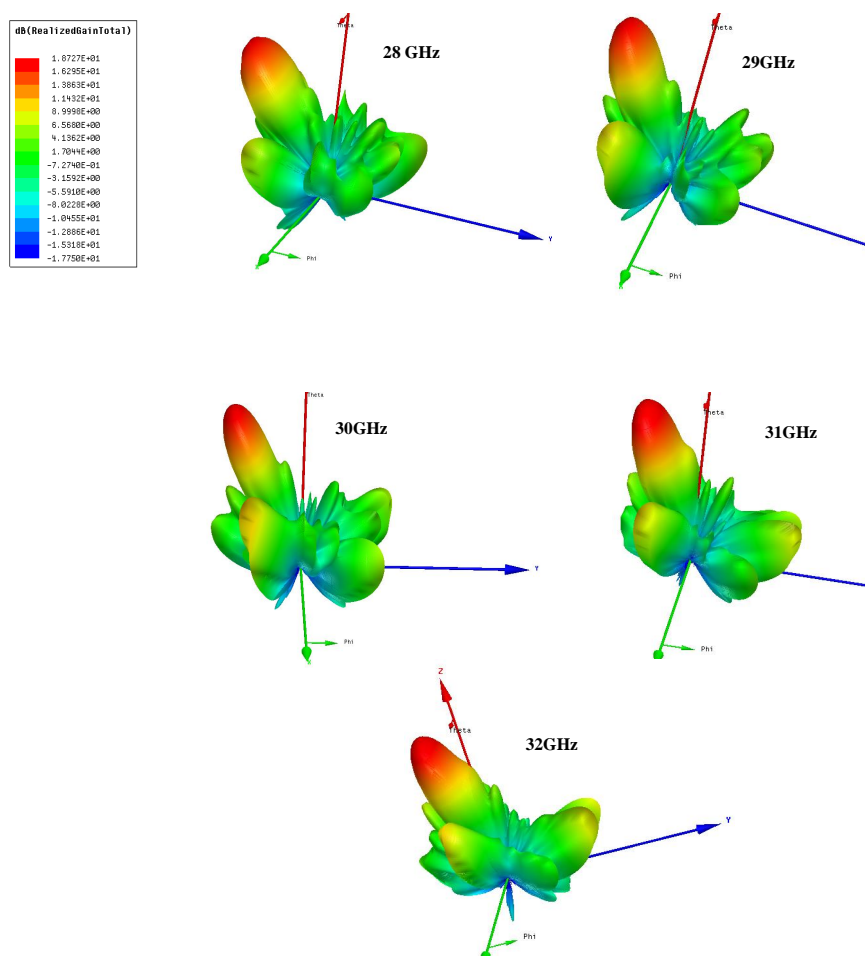


FIGURE 5.17: Simulated realized gain of 3D radiation pattern for 29, 30, 31 and 32 GHz.

5.2.3 Dual-Beam RGW Frequency Beam-Scanning Antenna.

Designing components and antennas using RGW to work at millimeter-wave frequency band has attracted much attention recently, as this band offers high data rates. However, working at the mm-wave band is challenging, as the performance of the communication system decays due to multipath, dielectric losses and link blockage because of obstructions. These losses can be compensated by using high gain directional antennas rather than omnidirectional antennas [110]. Directional antennas confine the beam in a particular direction to reduce the multipath and interference effects. The dual-beam antenna is part of the directional antenna family, and has two directional beams. Since a dual-beam antenna has two symmetrical beams, it is capable of covering two nonadjacent areas, especially for indoor wireless systems [111]. The characteristics of the dual-beam antenna also offer valuable advantages for mobile communications [112].

In this section, the proposed FSA array in the previous section is exploited to design a dual-beam antenna for mm-wave applications over 28–32 GHz. The proposed antenna is designed based on exciting the odd mode TE_{10}^{RGW} rather than the fundamental mode. The behavior of the field distribution of the first higher mode TE_{10}^{RGW} , which is 180° out of phase and is of equal magnitude, as shown in Fig.5.10 (b), can be exploited to design an FSA antenna that has a dual-beam radiation pattern. Etching the slots alternating on one arm of the Y-junction and then making a mirror to the slots means that all the slots in the first arm will radiate in phase while being out of phase with those of the other Y-junction arm. Fig.5.18 shows the configuration of the proposed dual-beam FSA array line with identical slots on both Y-junction arms. The 3D radiation pattern of this proposed LWA array is shown in Fig.5.19.

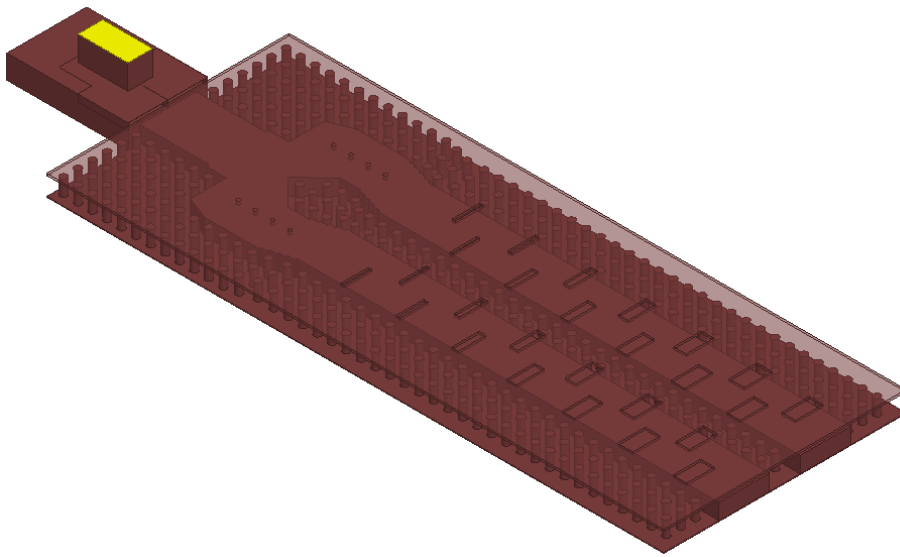


FIGURE 5.18: Configuration of the dual-beam FSA array line with identical slots on both Y-junction arms.

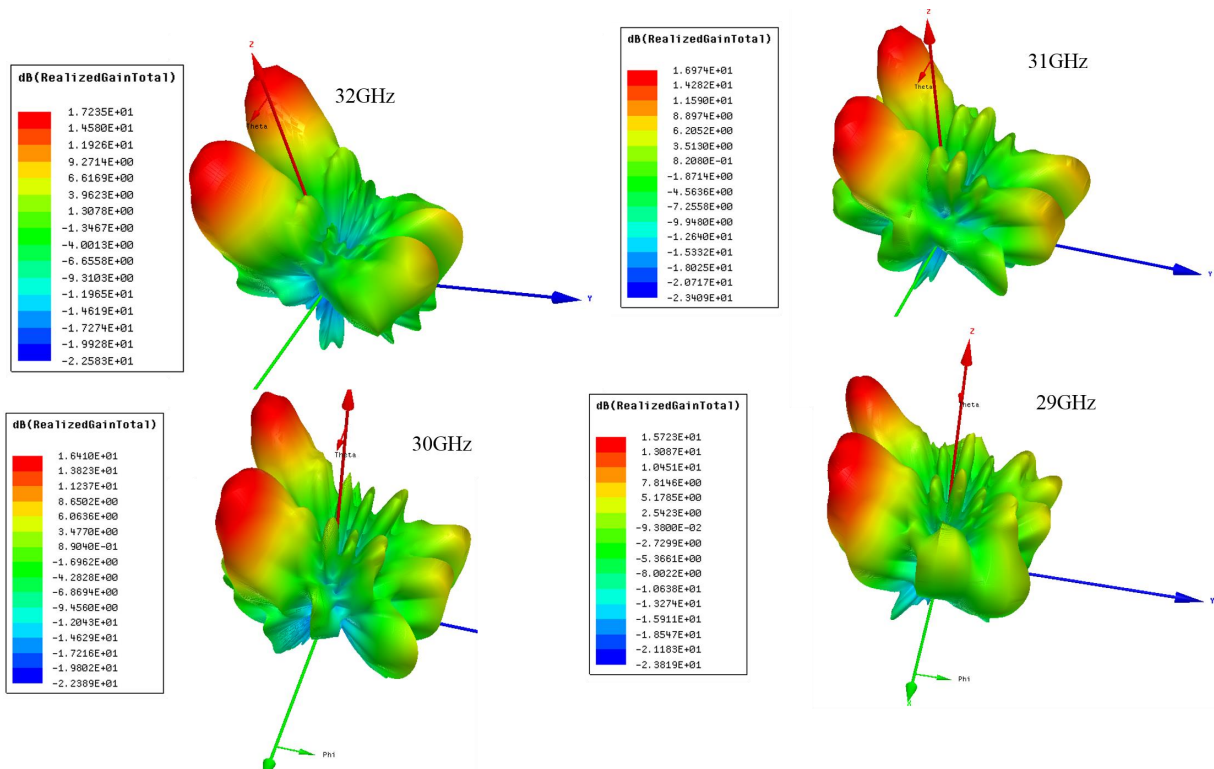


FIGURE 5.19: Simulated realized gain of 3D radiation pattern of dual-beam FSA array for 29, 30, 31 and 32 GHz.

5.2.4 Leaky Wave Antenna based on a First Higher-order Mode Ridge Gap Waveguide

Beam scanning antennas have received significant attention recently for short-range applications such as image and radar system detection. The leaky wave antenna (LWA) has the ability to produce beam scanning, and is part the traveling wave antenna family [113]. The LWA is used extensively due to its unique advantages compared to other antennas such as phased array and slot array antennas. For example, the LWA can produce a beam scanning without using phase shifters or requiring a complicated feeding network for its radiating elements.

Generally, the spacing between the radiated elements should be maintained sufficiently small to avoid having grating lobes at the highest frequency. To avoid the appearance of grating lobes in slot array and traveling-wave antennas, a phase shifter of 180° is used at the feed end of the antenna [113]. This will allow for the engraving and separating of the slots by a half wavelength. In [50], another technique is used to achieve a similar slot arrangement without needing a phase shifter.

Antenna Design and Theory

Based on the first higher-order mode of RGW discussed in Chapter 4, a leaky-wave antenna is designed and presented here for mm-wave applications. For the LWA to radiate to the broadside free space, it must operate in the fast-wave region space [113], in which the primary condition for designing an LWA is

$$-k_0 \leq \beta \leq k_0 \quad (5.2)$$

where k_0 is free space wavenumber and β is the phase constant of the wave along the guiding structure. The angle of the main lobe radiation pattern (θ_n) can be determined by

$$\sin(\theta_n) = \frac{\beta_n}{k_0} \quad (5.3)$$

where β_n is the phase constant of n th space harmonic, in which the space harmonic based on the Floquet's theory. Based on the hybrid PEC/PMC waveguide that introduced in Chapter 3 and Floquet's theorem, the dispersion diagram can be obtained by

$$\beta_n = \beta_0 + \frac{2\pi n}{p} \quad (5.4)$$

$$\beta_{10} = \sqrt{k_0^2 \epsilon_r - \left(\frac{\pi}{w}\right)^2} \quad (5.5)$$

Where p, n , and ϵ_r are the period, the number of the space harmonic and the permittivity in the RGW gap, respectively. Because the fundamental mode in this RGW is the first higher-order mode TE_{10}^{RGW} rather than the usual Q-TEM mode, the β_0 is β_{10} . In this structure, the excitation of the n th slots, including 180° phase, is different due to the displacement of all the slots on the sides of the center line, as shown in Fig.5.20. Therefore for all slots to radiate in phase in the broadside with beam scanning angle θ , it is essential that [114]

$$\beta_n = \beta_0 - \pi + \frac{2\pi n}{p} \quad (5.6)$$

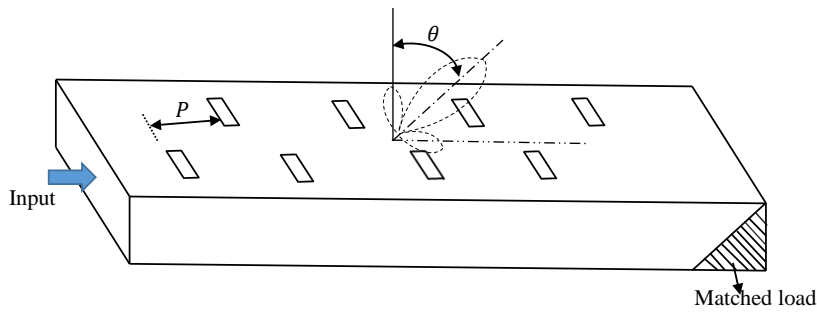


FIGURE 5.20: Sketch of center dismantlement leaky wave antenna.

Based on (5.6), we select the appropriate values for ϵ_r and p so that the radiation occurs only due to the $n = -1$ space harmonic, which leads to beam scanning of the radiation pattern in the backward quadrant. Fig.5.21 (a) shows the designed antenna based on RGW technology, in which an RT/Duroid 5880 substrate with a 1.58mm thickness is used.

The proposed leaky-wave antenna without the feed parts is designed and simulated by using the CST simulator. Wave ports are used at the ends of the RGW. The dispersion diagram of the harmonics created by the periodic slots can be determined from (5.6), in which the distance between two successive slots is 2.5 mm. The mode curves of the proposed leaky wave antenna are shown in Fig.5.21 (b). The propagation constant β_0 of the fundamental mode is larger than the propagation constant in free space k_0 , which is labeled by the red curve in Fig.5.21 (b). The leaky wave mode (β_{-1}) enters the leaky mode region at $f = 27.6$ GHz. According to the dispersion diagram, the proposed antenna can work as a leaky-wave antenna with a single beam only when $-k_0 < \beta_{-1} < k_0$ so that the radiation of the designed antenna occurs due to $n=-1$ space harmonic. Fig.5.21 (c) presents both the beam angle created with the CST simulator and the beam angle calculated by using (5.6) and (5.3).

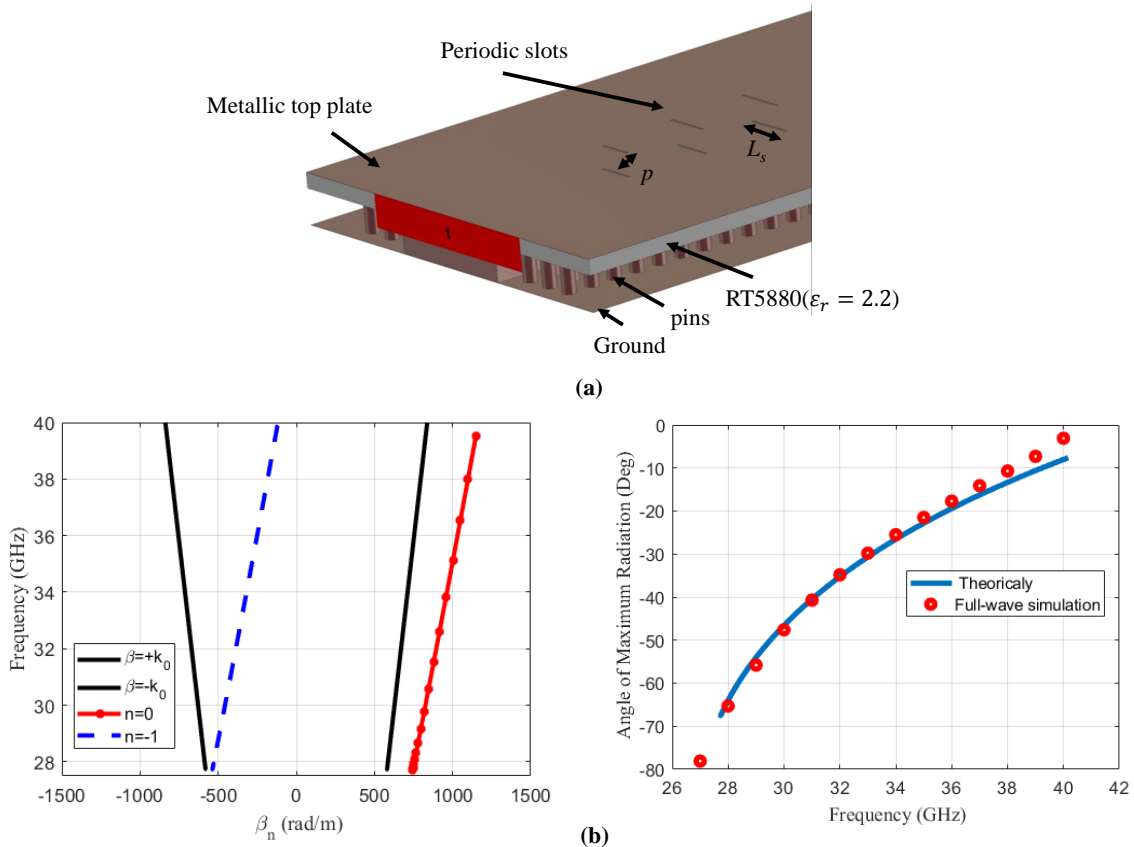


FIGURE 5.21: (a) Sketch of a leaky wave antenna; (b) Dispersion diagram; and (c) Comparison of the simulated and calculated angles of maximum radiation of the RGW leaky-wave antenna for the TE_{10}^{RGW} .

TABLE 5.3: DIMENSIONS OF THE LWA

Parameter	L_s	W_{sub}	W_{tap}	L_{tap}	w_1	w_2	w_3
Value(mm)	2.3	22	7.28	10	0.2	0.24	0.32
Parameter	w_4	w_5	w_6	w_7	w_8	w_9	w_{10}
Value(mm)	0.4	0.48	0.56	0.64	0.72	0.8	0.88
Parameter	w_{11}	w_{12}	w_{13}	w_{14}	w_{15}	w_{16}	w_{17}
Value(mm)	0.96	1.04	1.12	1.2	1.28	1.36	1.44
Parameter	w_{18}	w_{19}	L_{sub}	P			
Value(mm)	1.52	1.6	124	2.5			

The proposed geometry of the LWA is shown in Fig.5.22, in which horizontal slots are etched in the top plate, alternating on the two sides of the RGW. In order to have uniform amplitude distribution from each slot, the width of the slots is gradually increased, as shown in Fig.5.22. Two magic tees are used to feed the antenna, one at the input of the ridgeline and one at the end. Two tapered substrate sections are used at the outputs of the magic tees; these are very important for improving the matching. The associated dimensions are given in Table 5.3.

The simulated reflection coefficients of the RGW-LWA are shown in Fig.5.23, and are below -10 dB. The simulated peak realized gain of the antenna is 18.4 dBi, with less than 3dB variation throughout the whole operating bandwidth (28 to 35 GHz). The simulated radiation patterns of the designed LWA are presented in Fig 5.24, and show that the desired beam scanning has been achieved, in which the range of beam scanning is from -62° at 28 GHz to -12° at 35GHz.

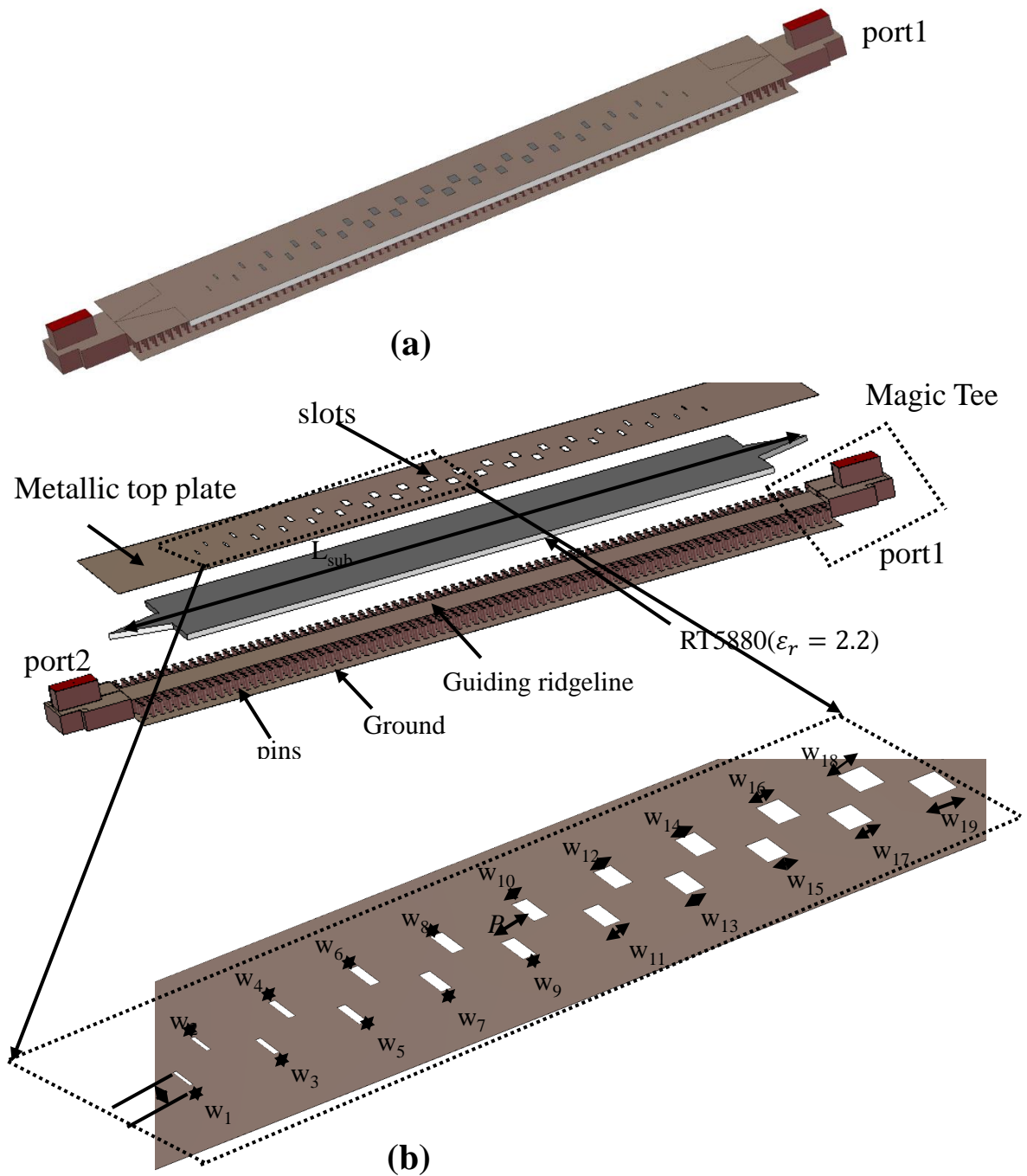


FIGURE 5.22: (a) Complete configuration of the RGW-LWA; and (b) Separated view of the stacked layers with a zoom view close to the slots and a magic tee .

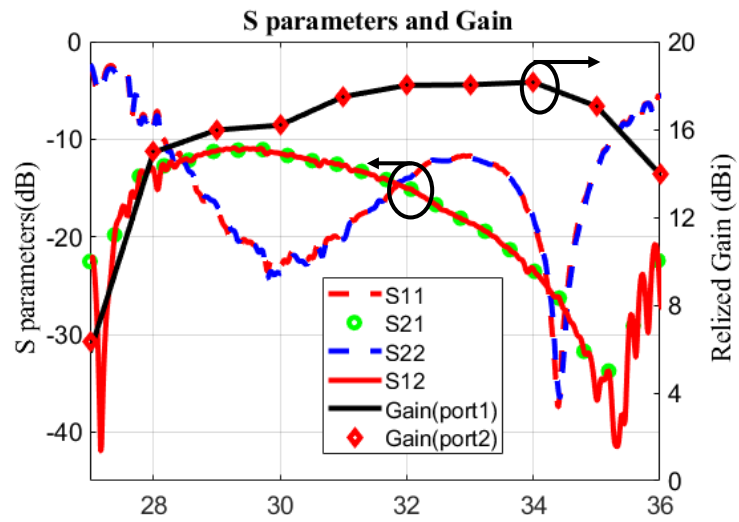


FIGURE 5.23: Simulated S parameters and gain of the proposed LWA .

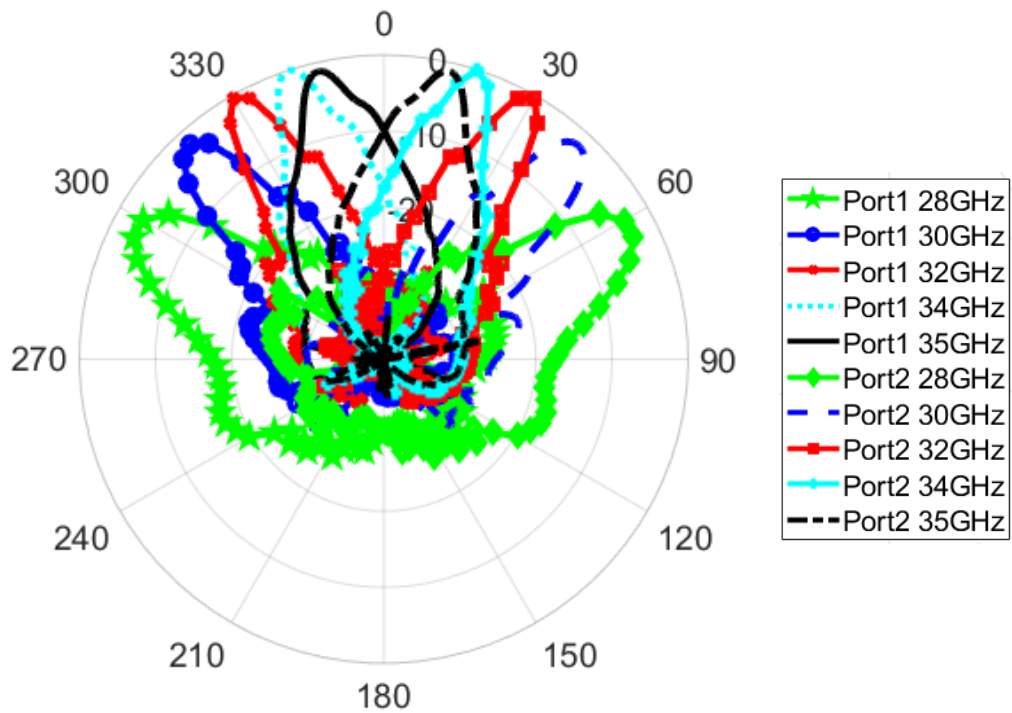


FIGURE 5.24: Simulated realized gain of the radiation pattern for 28,30,32,34 and 35 GHz for feeding from port1 and port2.

5.3 Sum and Difference Beam Switching Antenna

Switched beam antennas have attracted a huge amount of attention in wireless communication systems. This kind of antenna has several beneficial features, such as their coverage of multiple nonadjacent areas, ability to overcome interference and to enhance the channel capacity of wireless communication, as well as to point to multipoint systems. In addition, these antennas can guide power in particular directions instead of spreading it everywhere.

A Sum and difference beam switching antenna is presented here. The proposed antenna produces a single radiation pattern when fed by the Q-TEM mode, and a dual-beam pattern when fed by the TE_{10}^{RGW} mode. The typical application for type of antenna's characteristics is to cover nonadjacent areas by using difference-beam radiation and to cover the center area by using sum-beam radiation, as shown in Fig.5.25.

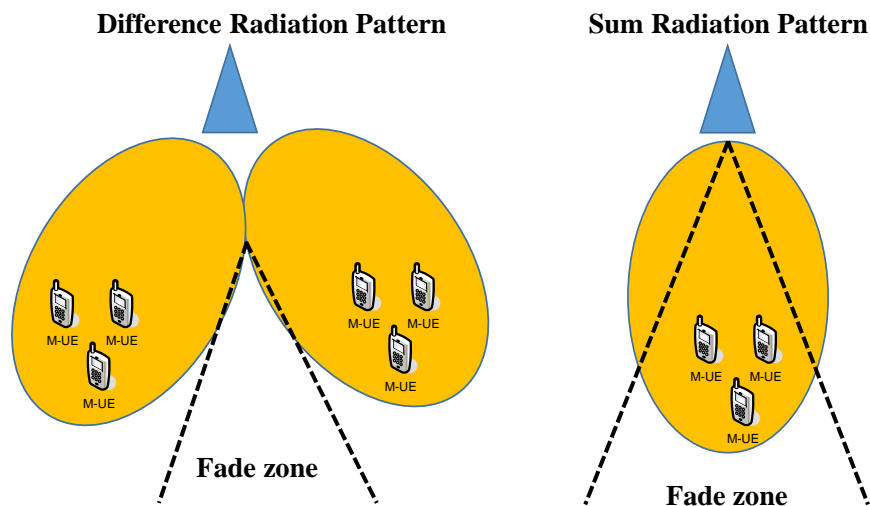


FIGURE 5.25: Switchable sum and difference radiation pattern.

5.3.1 Antenna Design

The proposed antenna is designed by using the dual-mode RGW introduced in the previous section to feed a horn antenna. The end of the ridge line section and the corresponding section of the top plate are extended to form the horn. The horn shape follows the Vivaldi antenna shape in the E-plane, and has the same width as the ridge line in the H-plane. Different views of the proposed antenna are shown in Fig.5.26.

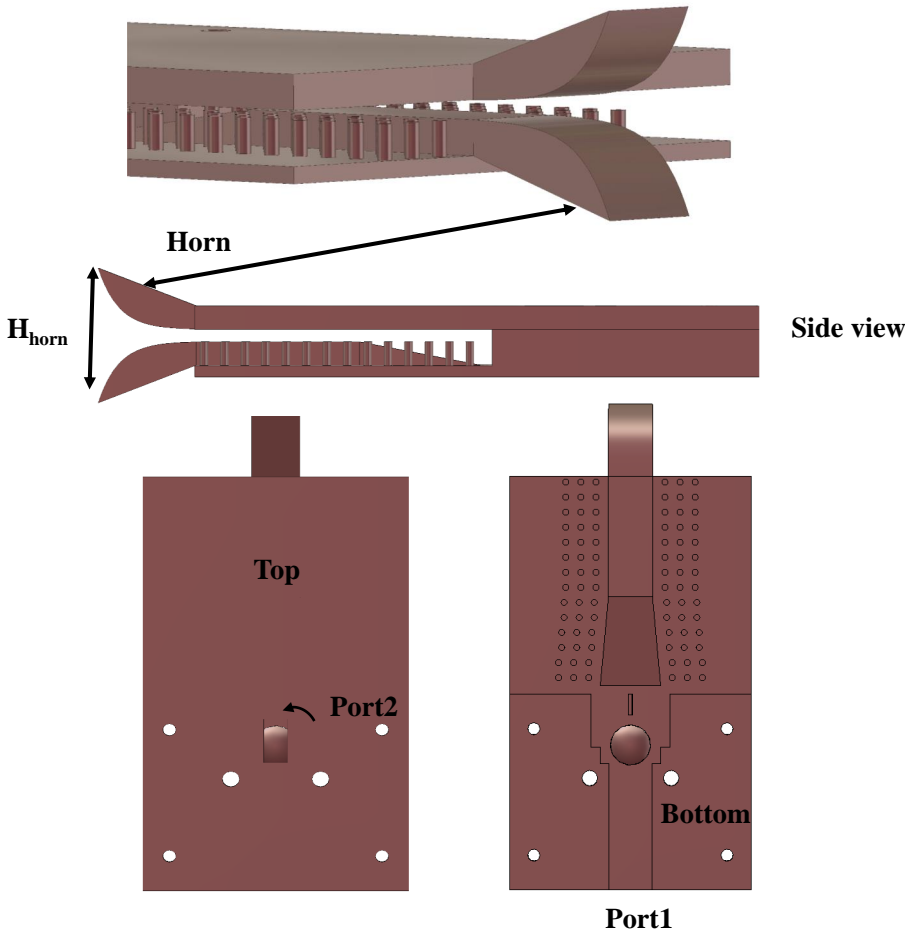


FIGURE 5.26: RGW Dual mode horn antenna views.

5.3.2 Results and Discussion

The simulated results of the sum and difference beam switching antenna fed by both Q-TEM and TE_{10}^{RGW} mode (Fig.5.27) reveal an overlap bandwidth of 25% from 28 to 36

GHz. The simulated peak realized gains for both sum and difference beams with varying frequencies are shown in Fig.5.27. The realized gain variation is very stable, with 1dB variation for the single beam and 1.5 dB variation for the dual beam throughout the whole operating bandwidth. The maximum gain for the Q-TEM radiation is 12.1 dBi, and for the first high order mode radiation it is 10.43 dBi. The gain difference between the sum and difference beam radiations is around 2 dBi. The simulated radiation patterns of the proposed antenna are presented in Fig.5.28 . These radiation patterns show that switchable, sum and difference-beam radiation patterns are achieved based on a dual-mode RWG horn antenna. The sum- and difference-beam radiation switching occurs in the H-plane, in which the sum-beam has its maxima at $\theta = 0$, while the difference-beam has its maxima at $\theta = \pm 35$, at 32 GHz.

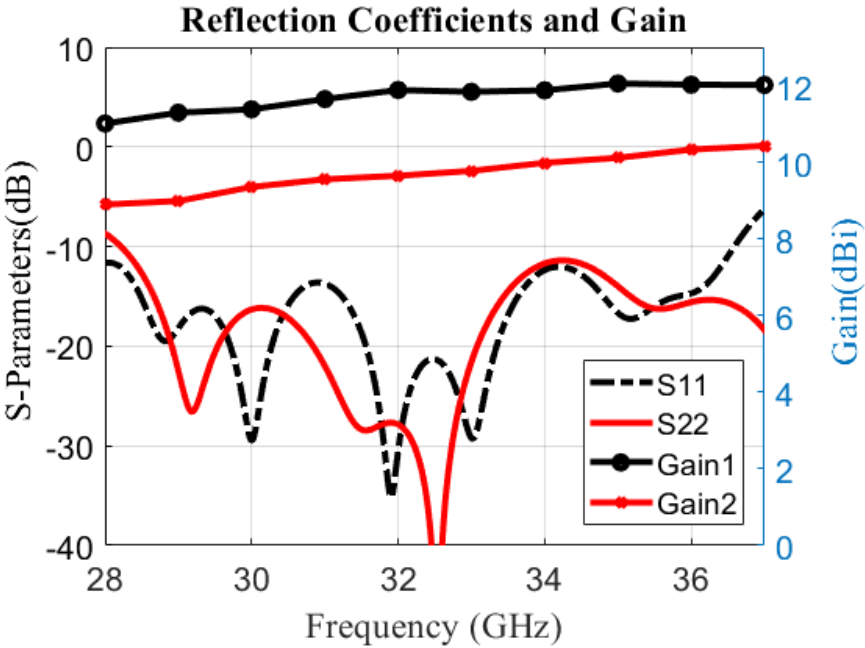


FIGURE 5.27: Simulated reflection coefficients and gain for both the sum- and difference-beam radiation modes.

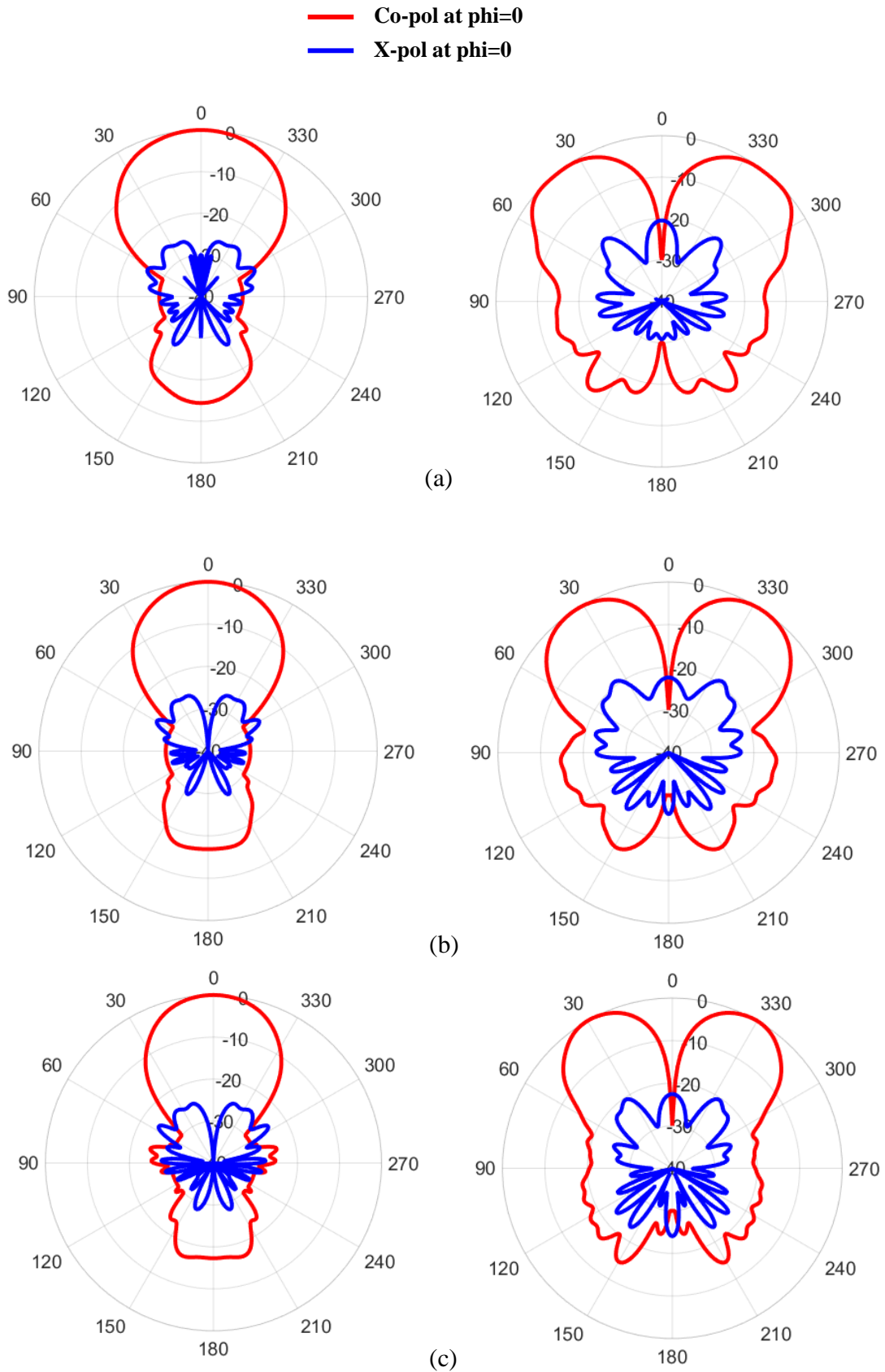


FIGURE 5.28: Simulated radiation patterns for the sum- and difference-beam radiation modes at center and at the two edge frequencies. (a) 28 GHz, (b) 32 GHz, and (c) 36 GHz.

Chapter 6

Conclusion and future work

6.1 Conclusion

To exploit the huge available bandwidth at the mm-wave band, microwave researchers and designers have started developing components, antennas and circuits that work at high-frequency bands. However, there are massive challenges to designing high frequency systems, such as propagation and system loss. A low-loss guiding structure and a high-gain antenna are required to compensate the losses in high-frequency systems. Consequently, in this work, the ridge gap waveguide (RGW) technology is used for designing components and antennas at the mm-wave band. The main scope of this work concentrates on designing the first higher-order gap waveguide passive components and antennas at the mm-wave band. This dissertation concentrates mainly on the metallic ridge gap waveguide. Chapter 2 provided a literature review and background of the ridge gap waveguide and its dispersion diagram.

A systematic design methodology for a hybrid junction based on RGW technology introduced in Chapter 3. The proposed method relies on the operation of a hybrid PEC/PMC waveguide. This waveguide offers the possibility to accurately estimate all the dimensions of the RGW coupler that are required in order to operate at a particular frequency band. The phase response analysis of a circular RGW bend is also introduced in chapter 3. The potential of tuning the center frequency of an RGW coupler by moving the upper plate of the RGW is proposed. To validate the proposed design, a prototype of the whole

0dB coupler structure was fabricated and tested. The measurement and simulation results show reasonable agreement and prove that the 0dB coupler works effectively with a coupling lengths calculated from the proposed PEC/PMC model.

Chapter 4 proposes two methods for the first higher-order mode TE_{10}^{RGW} excitation: excitation of the first high order mode by magic tee and by L-shape transition. A Y-junction power divider and 3dB forward coupler based on the first higher-order mode of an RGW are then designed. The Y-junction has a wideband frequency matching from 28 to 34 GHz, with return loss better than 15dB, and the transmission output levels are about -3.3 dB. A new 3dB odd-mode RGW coupler is also introduced, in which the simulated return loss and isolation are better than 15dB for the frequency band from 28GHz to 35GHz, and the output transmission coefficients are about -3dB with 1 dB variation. Moreover, a dual-mode ridge gap waveguide is simulated, fabricated, and measured. The measured results are in good agreement with the simulated results. The dual-mode ridge gap waveguide achieved a matching level less than -10 dB for the two modes over the operating band 28.77GHz to 34.61GHz with high isolation between the input ports.

A differential excitation mechanism for a 4x4-element cavity slot array antenna is presented in Chapter 5. This mechanism is implemented using the TE_{10}^{RGW} mode of a wide RGW. The designed antenna structure is fabricated and measured, and the results show a good agreement. The designed antenna offers good performance with a 16.5 dBi realized gain, a good symmetrical radiation pattern, and low cross-polarization level (-35 dB in the E-plane and -27 dB in the H-plane) within the 32.5-35.3 GHz frequency range.

In the same Chapter, 2x1 linear frequency scanning array antennas is designed. Initially, a single element of frequency scanning antenna was designed, followed by the design of a 2x1 element linear array. The bandwidth is from 28 GHz to 32.5 GHz and the matching is -15 dB with 19.15 dBi peak realized gain. The beam scan is from -11° to 40° at 28 GHz and 32 GHz, respectively. And then a dual-beam FSA array line antenna is presented, which provides reasonable results in terms of the gain and bandwidth, and in terms of the beam angle scanning. Also, a leaky wave antenna (LWA) based on the first higher-order mode RGW at the mm-wave band is introduced. The proposed design

provides wide bandwidth, wide scanning range, and high gain with high radiation efficiency. This designed LWA offers 22% of bandwidth at 31.5 GHz and a peak realized gain of 18.5 dBi with beam scanning range from -62° at 28 GHz to -12° at 35 GHz. The radiation efficiency of this design is more than 94% over the operating band of 28-35 GHz. Finally, A dual-functional sum- and difference-beam antenna is then presented, based on the proposed dual-mode RGW. The proposed antenna features a wide bandwidth and switchable radiation pattern from 28 to 36 GHz. Moreover, the gain and the radiation pattern are stable over the entire operating frequency.

6.2 The future work

The future proposed research has three main goals, namely the following:

- The work proposed in the dissertation presents as a proof of concept for a first higher-order mode of gap waveguide technology and its potential, however its usage at the mm-wave frequency for wireless systems need more system-level estimation. Many components such as magic tees, couplers, phase shifters, and feeding networks are needed to design a full system based on first higher-order mode RGW. Also, in order to exploit the full advantages of high order mode RGW, the active components need to be combined with RGW.
- A critical technical issue needs to be resolved in order to improve the results. This issue is the fabrication tolerances of CNC milling technique, which need much more investigations in order to implement various gap waveguide antennas and components at the mm-wave band. On the other hand, several manufacturing techniques such as metallic 3D printing and laser milling can be proper for realizing high frequency RGW structures, in which they need more investigation.

- The present work mainly focuses on metallic ridge gap waveguide technology, in which the potential of printed gap waveguide technology still remains to be investigated. Efforts to design suitable transitions for exciting the first higher-order mode would greatly help to advance this field.

Bibliography

- [1] J. Wells, "Faster than fiber: The future of multi G/S wireless," *IEEE Microwave Magazine*, vol. 10, no. 3, pp. 104–112, 2009.
- [2] E. Levine, G. Malamud, S. Shtrikman, and D. Treves, "A study of microstrip array antennas with the feed network," *IEEE Transactions on Antennas and Propagation*, vol. 37, no. 4, pp. 426–434, 1989.
- [3] F. Mesa, A. A. Oliner, D. R. Jackson, and M. J. Freire, "The influence of a top cover on the leakage from microstrip line," *IEEE Transactions on Microwave Theory and Techniques*, vol. 48, no. 12, pp. 2240–2248, Dec 2000.
- [4] D. Pozar, *Microwave Engineering*. Wiley, 1997.
- [5] S. Gupta, Z. Briqech, and A. R. Sebak, "Analysis of 60 GHz ridge gap waveguide based junctions, bends and losses," *IEEE International Conference on Antenna Innovations Modern Technologies for Ground, Aircraft and Satellite Applications (iAIM)*, pp. 1–4, Nov 2017.
- [6] A. Vosoogh, P.-S. Kildal, and V. Vassilev, "Wideband and high-gain corporate-fed gap waveguide slot array antenna with ETSI class II radiation pattern in V -band," *IEEE Transactions on Antennas and Propagation*, vol. 65, no. 4, pp. 1823–1831, 2016.
- [7] A. Vosoogh and P. S. Kildal, "Corporate-fed planar 60 GHz slot array made of three unconnected metal layers using AMC pin surface for the gap waveguide," *IEEE Antennas and Wireless Propagation Letters*, vol. 15, pp. 1935–1938, 2015.
- [8] D. Zarifi, A. Farahbakhsh, A. U. Zaman, and P. S. Kildal, "Design and fabrication of a high gain 60 GHz corrugated slot antenna array with ridge gap waveguide

- distribution layer," *IEEE Transactions on Antennas and Propagation*, vol. 64, no. 7, pp. 2905–2913, 2016.
- [9] G. Bit-Babik, C. Di Nallo, and A. Faraone, "Multimode dielectric resonator antenna of very high permittivity," *IEEE Antennas and Propagation Society Symposium*, vol. 2, pp. 1383–1386, June 2004.
- [10] B. Li and K. W. Leung, "A wideband strip-fed rectangular dielectric resonator antenna," *IEEE Antennas and Propagation Society International Symposium*, vol. 2A, pp. 172–175, July 2005.
- [11] A. Petosa, S. Thirakoune, and A. Ittipiboon, "Higher-order modes in rectangular dras for gain enhancement," *2009 13th International Symposium on Antenna Technology and Applied Electromagnetics and the Canadian Radio Science Meeting*, pp. 1–4, Feb 2009.
- [12] J. Xu, Z. N. Chen, X. Qing, and W. Hong, "A single-layer SIW slot array antenna with TE₂₀ mode," *Asia-Pacific Microwave Conference 2011*, pp. 1330–1333, Dec 2011.
- [13] A. Suntives and R. Abhari, "Design and application of multimode substrate integrated waveguides in parallel multichannel signaling systems," *IEEE Transactions on Microwave Theory and Techniques*, vol. 57, no. 6, pp. 1563–1571, 2009.
- [14] P. Wu, J. Liu, and Q. Xue, "Wideband Excitation Technology of TE₂₀ Mode Substrate Integrated Waveguide (SIW) and Its Applications," *IEEE Transactions on Microwave Theory and Techniques*, vol. 63, no. 6, pp. 1863–1874, 2015.
- [15] X. Li, J. Xiao, Z. Qi, and H. Zhu, "Broadband and High-Gain SIW-Fed Antenna Array for 5G Applications," *IEEE Access*, vol. 6, pp. 56282–56289, 2018.
- [16] Z. Pi and F. Khan, "An introduction to millimeter-wave mobile broadband systems," *IEEE Communications Magazine*, vol. 49, no. 6, pp. 101–107, June 2011.

- [17] T. S. Rappaport, S. Sun, R. Mayzus, H. Zhao, Y. Azar, K. Wang, G. N. Wong, J. K. Schulz, M. Samimi, and F. Gutierrez, "Millimeter Wave Mobile Communications for 5G Cellular," *IEEE Access*, vol. 1, pp. 335–349, 2013.
- [18] A. Polemi, S. Maci, and P. S. Kildal, "Dispersion characteristics of a metamaterial-based parallel plate ridge gap waveguide realized by bed of nails," *IEEE Transactions on Antennas and Propagation*, vol. 59, no. 3, pp. 904–913, 2010.
- [19] T. K. Sarkar, M. C. Wicks, M. Salazar Palma, R. J. Bonneau *et al.*, *Smart antennas*. Wiley Online Library, 2003.
- [20] T. K. Sarkar, R. Mailloux, A. A. Oliner, M. Salazar Palma, and D. L. Sengupta, *History of wireless*. John Wiley & Sons, 2006, vol. 177.
- [21] H. Jia-Sheng and M. Lancaster, *Microstrip filters for RF/microwave applications*. New York:Wiley, 2001.
- [22] R. Simons, *Coplanar Waveguide Circuits, Components, and Systems*, ser. Wiley Series in Microwave and Optical Engineering. Wiley, 2004.
- [23] L. G. Maloratsky, "Reviewing the basics of suspended striplines.(tutorial)," *Microwave journal*, vol. 45, no. 10, pp. 82–91, 2002.
- [24] M.-H. Ho and P.-F. Chen, "Suspended substrate stripline bandpass filters with source load coupling structure using lumped and full-wave mixed approach," *Progress In Electromagnetics Research*, vol. 122, pp. 519–535, 2012.
- [25] C. A. Balanis, *Antenna theory: analysis and design*. John wiley & sons, 2016.
- [26] C. A. Palmer and E. G. Loewen, *Diffraction grating handbook*. Thermo RGL New York, 2002, vol. 5.
- [27] D. Deslandes and K. Wu, "Single substrate integration technique of planar circuits and waveguide filters," *IEEE Transactions on microwave theory and Techniques*, vol. 51, no. 2, pp. 593–596, 2003.

- [28] F. Xu and K. Wu, "Guided wave and leakage characteristics of substrate integrated waveguide," *IEEE Transactions on microwave theory and techniques*, vol. 53, no. 1, pp. 66–73, 2005.
- [29] M. Bozzi, M. Pasian, L. Perregrini, and K. Wu, "On the losses in substrate integrated waveguides," *2007 European Microwave Conference*, pp. 384–387, 2007.
- [30] P. S. Kildal, E. Alfonso, A. Valero Nogueira, and E. Rajo Iglesias, "Local metamaterial based waveguides in gaps between parallel metal plates," *IEEE Antennas and Wireless Propagation Letters*, vol. 8, no. 2009, pp. 84–87, 2009.
- [31] P.-S. Kildal, "Three metamaterial-based gap waveguides between parallel metal plates for mm/submm waves," *2009 3rd European Conference on Antennas and Propagation*, pp. 28–32, 2009.
- [32] P.-S. Kildal and A. Kishk, "EM Modeling of surfaces with STOP or GO characteristics-artificial magnetic conductors and soft and hard surfaces," *Applied Computational Electromagnetics Society Journal*, vol. 18, no. 1, pp. 32–40, 2003.
- [33] D. Sievenpiper, L. Zhang, R. F. Broas, N. G. Alexopolous, E. Yablonovitch *et al.*, "High impedance electromagnetic surfaces with a forbidden frequency band," *IEEE Transactions on Microwave Theory and techniques*, vol. 47, no. 11, pp. 2059–2074, 1999.
- [34] Y. J. Lee, J. Yeo, R. Mittra, and W. S. Park, "Application of electromagnetic bandgap (EBG) superstrates with controllable defects for a class of patch antennas as spatial angular filters," *IEEE Transactions on Antennas and Propagation*, vol. 53, no. 1, pp. 224–235, 2005.
- [35] S.-G. Mao and M.-Y. Chen, "Propagation characteristics of finite width conductor-backed coplanar waveguides with periodic electromagnetic bandgap cells," *IEEE transactions on Microwave Theory and Techniques*, vol. 50, no. 11, pp. 2624–2628, 2002.

- [36] F. Yang and Y. Rahmat-Samii, "Reflection phase characterizations of the EBG ground plane for low profile wire antenna applications," *IEEE Transactions on antennas and propagation*, vol. 51, no. 10, pp. 2691–2703, 2003.
- [37] P. A. Belov, R. Marqués, S. I. Maslovski, I. S. Nefedov, M. Silveirinha, C. R. Simovski, and S. A. Tretyakov, "Strong spatial dispersion in wire media in the very large wavelength limit," *Phys. Rev. B*, vol. 67, p. 113103, Mar 2003.
- [38] M. G. Silveirinha, C. A. Fernandes, and J. R. Costa, "Electromagnetic characterization of textured surfaces formed by metallic pins," *IEEE Transactions on Antennas and Propagation*, vol. 56, no. 2, pp. 405–415, 2008.
- [39] E. Rajo-Iglesias, M. Ferrando-Rocher, and A. U. Zaman, "Gap waveguide technology for millimeter wave antenna systems," *IEEE Communications Magazine*, vol. 56, no. 7, pp. 14–20, 2018.
- [40] N. Ashraf, A. A. Kishk, and A. Sebak, "Ridge Gap Waveguide Quasi-TEM Horn Antenna for Ka-band Applications," *2018 IEEE International Symposium on Antennas and Propagation USNC/URSI National Radio Science Meeting*, pp. 421–422, July 2018.
- [41] J. Liu, A. Vosoogh, A. U. Zaman, and J. Yang, "A slot array antenna with single-layered corporate-feed based on ridge gap waveguide in the 60 GHz band," *IEEE Transactions on Antennas and Propagation*, vol. 67, no. 3, pp. 1650–1658, 2018.
- [42] Q. Gao, "Ridged waveguide slot antenna using high impedance ground plane," *IEEE Antennas and Wireless Propagation Letters*, vol. 6, pp. 454–456, 2007.
- [43] D. Zarifi, A. Farahbakhsh, A. U. Zaman, and P.-S. Kildal, "Design and fabrication of a high gain 60 GHz corrugated slot antenna array with ridge gap waveguide distribution layer," *IEEE Transactions on Antennas and Propagation*, vol. 64, no. 7, pp. 2905–2913, 2016.

- [44] S. I. Shams and A. A. Kishk, "Design of 3-dB hybrid coupler based on RGW technology," *IEEE Transactions on Microwave Theory and Techniques*, vol. 65, no. 10, pp. 3849–3855, 2017.
- [45] M. M. M. Ali, S. I. Shams, and A. R. Sebak, "Printed ridge gap waveguide 3 dB coupler Analysis and design procedure," *IEEE Access*, vol. 6, pp. 8501–8509, 2017.
- [46] A. Polemi and S. Maci, "Closed form expressions for the modal dispersion equations and for the characteristic impedance of a metamaterial based gap waveguide," *IET microwaves, antennas propagation*, vol. 4, no. 8, pp. 1073–1080, 2010.
- [47] Y. J. Cheng, W. Hong, and K. Wu, "Design of a monopulse antenna using a dual V-type linearly tapered slot antenna (DVL TSA)," *IEEE Transactions on Antennas and Propagation*, vol. 56, no. 9, pp. 2903–2909, 2008.
- [48] X. Cheng and Y.-K. Yoon, "Hybrid mode radiation in patch antenna loaded with corrugated electric via arrays," *2011 IEEE International Symposium on Antennas and Propagation (APSURSI)*, pp. 2080–2082, 2011.
- [49] W. Peng, W. Cao, and Z. Qian, "High-gain electrically large air-cavity-backed patch antenna element and array," *IEEE Access*, vol. 6, pp. 74 072–74 080, 2018.
- [50] S. I. Shams, M. A. Abdelaal, and A. A. Kishk, "Broadside uniform leaky-wave slot array fed by ridge gap splitted line," in *2015 IEEE International Symposium on Antennas and Propagation USNC/URSI National Radio Science Meeting*. IEEE, 2015, pp. 2467–2468.
- [51] S. I. Shams and A. A. Kishk, "Wide band power divider based on ridge gap waveguide," in *2016 17th International Symposium on Antenna Technology and Applied Electromagnetics (ANTEM)*, 2016, pp. 1–2.
- [52] E. Alfonso, M. Baquero, A. Valero-Nogueira, J. Herranz, and P.-S. Kildal, "Power divider in ridge gap waveguide technology," in *Proceedings of the Fourth European Conference on Antennas and Propagation*, 2010, pp. 1–4.

- [53] M. R. Rahimi, N. Bayat-Makou, and A. A. Kishk, "Millimeter-Wave Substrate Integrated Gap Waveguide Leaky-Wave Antenna for WiGig Applications," *IEEE Transactions on Antennas and Propagation*, 2019.
- [54] J. Xi, B. Cao, H. Wang, and Y. Huang, "A novel 77 GHz circular polarization slot antenna using ridge gap waveguide technology," in *2015 Asia-Pacific Microwave Conference (APMC)*, vol. 3, 2015, pp. 1–3.
- [55] A. U. Zaman and P.-S. Kildal, "Ku band linear slot-array in ridge gapwaveguide technology," in *2013 7th European Conference on Antennas and Propagation (EuCAP)*, 2013, pp. 3078–3081.
- [56] M. Ferrando-Rocher, A. Valero-Nogueira, J. I. Herranz-Herruzo, and A. Berenguer, "V-band single-layer slot array fed by ridge gap waveguide," in *2016 IEEE International Symposium on Antennas and Propagation (APSURSI)*, 2016, pp. 389–390.
- [57] M. A. Abdelaal, S. I. Shams, M. A. Moharram, M. Elsaadany, and A. A. Kishk, "Compact full band omt based on dual-mode double-ridge waveguide," *IEEE Transactions on Microwave Theory and Techniques*, vol. 66, no. 6, pp. 2767–2774, 2018.
- [58] J. Rebollar, J. Esteban, and J. De Frutos, "A dual frequency OMT in the Ku band for TT&C applications," in *IEEE Antennas and Propagation Society International Symposium*, vol. 4, 1998, pp. 2258–2261.
- [59] R. W. Jackson, "A planar orthomode transducer," *IEEE microwave and wireless components letters*, vol. 11, no. 12, pp. 483–485, 2001.
- [60] L. Petit, L. Dussopt, and J.-M. Laheurte, "MEMS-switched parasitic-antenna array for radiation pattern diversity," *IEEE Transactions on Antennas and Propagation*, vol. 54, no. 9, pp. 2624–2631, 2006.
- [61] A. I. Sotiriou, P. K. Varlamos, P. Trakadas, and C. N. Capsalis, "Performance of a six-beam switched parasitic planar array under one path rayleigh fading environment," *Progress In Electromagnetics Research*, vol. 62, pp. 89–106, 2006.

- [62] M. Kamran Saleem, M. A. Alkanhal, and A. F. Sheta, "Switched beam dielectric resonator antenna array with six reconfigurable radiation patterns," *International Journal of RF and Microwave Computer-Aided Engineering*, vol. 26, no. 6, pp. 519–530, 2016.
- [63] S. Yonezawa, R. Bakar, H. Arai, A. Miura, and H. Tsuji, "Beam switched antenna using inverted F antenna for mobile terminal," in *2016 International Symposium on Antennas and Propagation (ISAP)*, 2016, pp. 1064–1065.
- [64] V. Semkin, F. Ferrero, A. Bisognin, J. Ala-Laurinaho, C. Luxey, F. Devillers, and A. Räsänen, "Beam switching conformal antenna array for mm-wave communications," *IEEE Antennas and Wireless Propagation Letters*, vol. 15, pp. 28–31, 2015.
- [65] K. Hosoya, N. Prasad, K. Ramachandran, N. Orihashi, S. Kishimoto, S. Rangarajan, and K. Maruhashi, "Multiple sector ID capture (MIDC): A novel beamforming technique for 60-GHz band multi-Gbps WLAN/PAN systems," *IEEE Transactions on Antennas and Propagation*, vol. 63, no. 1, pp. 81–96, 2014.
- [66] Z. L. Ma, C. H. Chan, K. B. Ng, and L. J. Jiang, "A supercell based dual beam dielectric grating antenna for 60 GHz application," in *2015 IEEE International Symposium on Antennas and Propagation and USNC/URSI National Radio Science Meeting*, 2015, pp. 643–644.
- [67] M. Danielsen and R. Jorgensen, "Frequency scanning microstrip antennas," *IEEE Transactions on Antennas and Propagation*, vol. 27, no. 2, pp. 146–150, 1979.
- [68] W. Cao, Z. N. Chen, W. Hong, B. Zhang, and A. Liu, "A beam scanning leaky-wave slot antenna with enhanced scanning angle range and flat gain characteristic using composite phase-shifting transmission line," *IEEE Transactions on Antennas and Propagation*, vol. 62, no. 11, pp. 5871–5875, Nov 2014.
- [69] R. S. Elliot, *antenna theory and design*. Prentice-Hall, 1981.

- [70] L. Cui, W. Wu, and D.-G. Fang, "Printed frequency beam-scanning antenna with flat gain and low sidelobe levels," *IEEE Antennas and Wireless Propagation Letters*, vol. 12, pp. 292–295, 2013.
- [71] F. Molaee-Ghaleh and K. Mohammadpour-Aghdam, "Design of a Millimeter-Wave Frequency-Scanning Slot Array Antenna in SIW Technology," in *2018 Fifth International Conference on Millimeter-Wave and Terahertz Technologies (MMWaTT)*, 2018, pp. 74–77.
- [72] M. Singh and B. Ghosh, "Substrate Integrated Waveguide (SIW) Leaky-Wave Antenna With Sinusoidally Modulated Transverse Slots," in *2018 IEEE Indian Conference on Antennas and Propagation (InCAP)*, Dec 2018, pp. 1–4.
- [73] J. L. Gomez-Tornero, D. Canete-Rebenaque, and A. Alvarez-Melcon, "Microstrip leaky-wave antenna with control of leakage rate and only one main beam in the azimuthal plane," *IEEE Transactions on Antennas and Propagation*, vol. 56, no. 2, pp. 335–344, Feb 2008.
- [74] H. J. Riblet, "The short-slot hybrid junction," *Proceedings of the IRE*, vol. 40, no. 2, pp. 180–184, 1952.
- [75] I. Bahl and P. B. R. Mongia, "RF and microwave coupled line circuits," *Microwave Journal*, vol. 44, no. 5, pp. 390–390, 2001.
- [76] R. F. Harrington, "Time-harmonic," *Electromagnetic Fields*, pp. 168–171, 2001.
- [77] T. Oyedokun, R. Geschke, and T. Stander, "A tunable ka-band planar groove gap waveguide resonant cavity," in *2017 IEEE Radio and Antenna Days of the Indian Ocean (RADIO)*, 2017, pp. 1–2.
- [78] S. Sirci, J. Martinez, M. Taroncher, and V. Boria, "Varactor-loaded continuously tunable SIW resonator for reconfigurable filter design," in *2011 41st European Microwave Conference*, 2011, pp. 436–439.

- [79] A. A. Brazález, A. U. Zaman, and P.-S. Kildal, "Investigation of a microstrip-to-ridge gap waveguide transition by electromagnetic coupling," in *Proceedings of the 2012 IEEE International Symposium on Antennas and Propagation*, 2012, pp. 1–2.
- [80] A. U. Zaman, T. Vukusic, M. Alexanderson, and P.-S. Kildal, "Design of a simple transition from microstrip to ridge gap waveguide suited for MMIC and antenna integration," *IEEE Antennas and wireless propagation letters*, vol. 12, pp. 1558–1561, 2013.
- [81] A. A. Brazález, J. Flygare, J. Yang, V. Vassilev, M. Baquero-Escudero, and P.-S. Kildal, "Design of F-Band Transition From Microstrip to Ridge Gap Waveguide Including Monte Carlo Assembly Tolerance Analysis," *IEEE Transactions on Microwave Theory and Techniques*, vol. 64, no. 4, pp. 1245–1254, 2016.
- [82] A. Chauloux, F. Colombel, M. Himdi, J. Lasserre, P. Bruguiere, P. Pouliguen, and P. Potier, "High gain and low losses antenna array for high power microwave applications," in *The 8th European Conference on Antennas and Propagation (EuCAP 2014)*, 2014, pp. 1705–1709.
- [83] S. B. Yeap, Z. N. Chen, and X. Qing, "Gain enhanced 60 GHz LTCC antenna array with open air cavities," *IEEE Transactions on Antennas and Propagation*, vol. 59, no. 9, pp. 3470–3473, 2011.
- [84] W. Yang, H. Wang, W. Che, Y. Huang, and J. Wang, "High gain and low loss millimeter wave ltcc antenna array using artificial magnetic conductor structure," *IEEE Transactions on Antennas and Propagation*, vol. 63, no. 1, pp. 390–395, 2014.
- [85] A. Suntives and R. Abhari, "Ultra high speed multichannel data transmission using hybrid substrate integrated waveguides," *IEEE Transactions on Microwave Theory and Techniques*, vol. 56, no. 8, pp. 1973–1984, 2008.

- [86] H. Jin, W. Che, W. Yang, and K.-S. Chin, "A millimeter-wave TE 20-mode SIW-fed patch antenna array with differential feeding network," in *2017 47th European Microwave Conference (EuMC)*, 2017, pp. 400–403.
- [87] J. Xu, Z. N. Chen, X. Qing, and W. Hong, "A single-layer SIW slot array antenna with TE 20 mode," in *Asia-Pacific Microwave Conference*, 2011, pp. 1330–1333.
- [88] W. Han, F. Yang, J. Ouyang, and P. Yang, "Low cost wideband and high gain slotted cavity antenna using high order modes for millimeter wave application," *IEEE Transactions on Antennas and Propagation*, vol. 63, no. 11, pp. 4624–4631, 2015.
- [89] F. Ren, W. Hong, K. Wu, D. Yu, and Y. Wan, "Polarization adjustable planar array antenna with SIW fed high order mode microstrip patch," *IEEE Transactions on Antennas and Propagation*, vol. 65, no. 11, pp. 6167–6172, 2017.
- [90] K.-D. Xu, W. Li, and Y. Liu, "Dual-Frequency SIW cavity-backed slot antenna using two high-order modes," in *2017 Sixth Asia-Pacific Conference on Antennas and Propagation (APCAP)*, 2017, pp. 1–3.
- [91] C. Wu, H. Wang, X. Jiang, S. Quan, and X. Liu, "High-gain dual-polarization higher order mode substrate integrated cavity antenna array," in *2016 11th International Symposium on Antennas, Propagation and EM Theory (ISAPE)*, 2016, pp. 129–131.
- [92] A. Kaur, R. Khanna, and M. Kartikeyan, "A novel miniature antenna for Ka band applications at 33 GHz," in *2011 International Conference on Multimedia Technology*, 2011, pp. 2880–2883.
- [93] J. Huang, "A ka band circularly polarized high-gain microstrip array antenna," *IEEE Transactions on antennas and propagation*, vol. 43, no. 1, pp. 113–116, 1995.
- [94] P.-S. Kildal, A. U. Zaman, E. Rajo-Iglesias, E. Alfonso, and A. Valero-Nogueira, "Design and experimental verification of ridge gap waveguide in bed of nails for parallel-plate mode suppression," *IET Microwaves, Antennas and Propagation*, vol. 5, no. 3, pp. 262–270, 2011.

- [95] A. U. Zaman and P.-S. Kildal, "Slot antenna in ridge gap waveguide technology," in *2012 6th European Conference on Antennas and Propagation (EUCAP)*, 2012, pp. 3243–3244.
- [96] P. S. Kildal, A. U. Zaman, E. Rajo Iglesias, E. Alfonso, and A. Valero Nogueira, "Design and experimental verification of ridge gap waveguide in bed of nails for parallel-plate mode suppression," *IET Microwaves, Antennas & Propagation*, vol. 5, no. 3, pp. 262–270, 2011.
- [97] M. Bosiljevac, Z. Sipus, and P.-S. Kildal, "Construction of green's functions of parallel plates with periodic texture with application to gap waveguides—a plane-wave spectral-domain approach," *IET microwaves, antennas and propagation*, vol. 4, no. 11, pp. 1799–1810, 2010.
- [98] T. Granberg, *Handbook of digital techniques for high-speed design: design examples, signaling and memory technologies, fiber optics, modeling and simulation to ensure signal integrity*. Prentice-Hall, 2004.
- [99] F. Zarkeshvari, P. Noel, S. Uhanov, and T. Kwasniewski, "An overview of high-speed serial I/O trends, techniques and standards," in *Canadian Conference on Electrical and Computer Engineering 2004 (IEEE Cat. No. 04CH37513)*, vol. 2, 2004, pp. 1215–1220.
- [100] R. Farjad-Rad, C.-K. Yang, and M. A. Horowitz, "A 0.3- μm CMOS 8-Gb/s 4-PAM serial link transceiver," *IEEE Journal of Solid-State Circuits*, vol. 35, no. 5, pp. 757–764, 2000.
- [101] J. T. Stonick, G.-Y. Wei, J. L. Sonntag, and D. K. Weindler, "An adaptive PAM-4 5-Gb/s backplane transceiver in 0.25- μm CMOS," *IEEE Journal of Solid-State Circuits*, vol. 38, no. 3, pp. 436–443, 2003.

- [102] X. Ma, L. Li, M. Zhu, W. Chen, and Z. Han, "Multilevel polar-coded modulation based on cooperative relaying," in *2017 9th International Conference on Wireless Communications and Signal Processing (WCSP)*, 2017, pp. 1–4.
- [103] K. Wu, D. Deslandes, and Y. Cassivi, "The substrate integrated circuits-a new concept for high-frequency electronics and optoelectronics," in *6th International Conference on Telecommunications in Modern Satellite, Cable and Broadcasting Service*, vol. 1, 2003, pp. P–III.
- [104] C.-H. Tseng and T.-H. Chu, "Measurement of frequency-dependent equivalent width of substrate integrated waveguide," *IEEE transactions on microwave theory and techniques*, vol. 54, no. 4, pp. 1431–1437, 2006.
- [105] X.-W. Yuan, X.-C. Li, N. Wang, X.-J. Ma, Y. Shao, and J.-F. Mao, "High-speed data transmission system using half mode substrate integrated waveguide," in *2014 IEEE Electrical Design of Advanced Packaging Systems Symposium (EDAPS)*, 2014, pp. 105–108.
- [106] W. Ma, K. Wu, W. Hong, and Y.-J. Cheng, "Investigations on half-mode substrate integrated waveguide for high-speed interconnect application," in *2008 IEEE MTT-S International Microwave Workshop Series on Art of Miniaturizing RF and Microwave Passive Components*, 2008, pp. 120–123.
- [107] A. Suntives and R. Abhari, "Dual-mode high-speed data transmission using substrate integrated waveguide interconnects," in *2007 IEEE Electrical Performance of Electronic Packaging*, 2007, pp. 215–218.
- [108] H. Li, W. Hong, T. J. Cui, K. Wu, Y. L. Zhang, and L. Yan, "Propagation characteristics of substrate integrated waveguide based on LTCC," in *IEEE MTT-S International Microwave Symposium Digest*, 2003, vol. 3, 2003, pp. 2045–2048.

- [109] D. Stephens, P. R. Young, and I. D. Robertson, "Millimeter-wave substrate integrated waveguides and filters in photoimageable thick-film technology," *IEEE Transactions on Microwave Theory and Techniques*, vol. 53, no. 12, pp. 3832–3838, 2005.
- [110] P. F. Driessen, "Gigabit/s indoor wireless systems with directional antennas," *IEEE Transactions on Communications*, vol. 44, no. 8, pp. 1034–1043, 1996.
- [111] Y. Tao and G. Delisle, "Lens-fed multiple beam array for millimeter wave indoor communications," in *IEEE Antennas and Propagation Society International Symposium 1997. Digest*, vol. 4, 1997, pp. 2206–2209.
- [112] C.-C. Hu, C. Jsu, and J.-J. Wu, "An aperture-coupled linear microstrip leaky-wave antenna array with two-dimensional dual-beam scanning capability," *IEEE Transactions on Antennas and Propagation*, vol. 48, no. 6, pp. 909–913, 2000.
- [113] A. A. Oliner, D. R. Jackson, and J. Volakis, "Leaky-wave antennas," *Antenna engineering handbook*, vol. 4, p. 12, 2007.
- [114] R. E. Collin and F. Zucker, *Antenna theory*. McGraw-Hill, 1969.

List of Publications

Journals

- [J1] A. Beltayib and A. Sebak, "Analytical Design Procedure for Forward Wave Couplers in RGW Technology Based on Hybrid PEC/PMC Waveguide Model," in *IEEE Access*, vol. 7, pp. 119319-119331, 2019.
- [J2] A. Beltayib, I. Afifi and A. Sebak, " 4×4 -Element Cavity Slot Antenna Differentially-Fed by Odd Mode Ridge Gap Waveguide," in *IEEE Access*, vol. 7, pp. 48185-48195, 2019.
- [J3] A. Beltayib, I. Afifi and A. Sebak,, " Design of Dual Mode Ridge Gap Waveguide for Switchable Dual and Single Beam Antenna," submitted to *IEEE Transactions on Microwave Theory and Techniques*, November 2019.
- [J4] Z. Briqech, S. Gupta, A. Beltayib, A. Elboushi, , A. Sebak, and T. Denidni, "57- 64 GHz Imaging/Detection Sensor—Part I: System Setup and Experimental Evaluations," *IEEE Sensors Journal*, has been accepted for publication on Feb. 05, 2020

Conferences

- [C1] A.Beltayib , I. Afifi and A. Sebak, "Excitation of the first High order mode in Ridge Gap Waveguide," RAEMP2019 conference on Engineering Math and Physics , Cairo university, "accepted".
- [C2] I. Afifi , A.Beltayib and A. Sebak, "Ultra-wideband compact T-junction with optimized V cut for millimeter wave applications," RAEMP2019 conference on Engineering Math and Physics, Cairo university, "accepted" .
- [C3] A. Beltayib, M. Asaadi, Z. Briqech and A. Sebak, "A beam deflector based on gradient refractive index metamaterial," 2017 International Conference on Electromagnetics in Advanced Applications (ICEAA), Verona, 2017, pp. 1134-1136.
- [C4] M. Asaadi, A. Beltayib and A. Sebak, "High Gain High Dense Dielectric Patch Antenna Using FSS Superstrate for Millimeter-Wave Applications," 2018 18th International Symposium on Antenna Technology and Applied Electromagnetics (ANTEM), Waterloo, ON, 2018, pp. 1-2.